UNIVERSITÉ DU QUÉBEC

THÈSE PRÉSENTÉ À
L'UNIVERSITÉ DU QUÉBEC À CHICOUTIMI
COMME EXIGENCE PARTIELLE
DU DOCTORAT EN INGÉNIERIE

Par:
ALIREZA SAFAEE

NANOSTRUCTURED METAL SURFACES AND THEIR PASSIVATION FOR SUPERHYDROPHOBIC AND ANTI-ICING APPLICATIONS

LES SURFACES NANOSTRUCTURÉES ET LEUR PASSIVATION POUR DES APPLICATIONS DES REVÊTEMENTS SUPERHYDROPHOBES ET GLACIOPHOBES

Décembre 2008

Bibliothèque
Paul-Émile-Boulet

UQAC
Université du Québec
à Chicoutimi

Mise en garde/Advice

Afin de rendre accessible au plus grand nombre le résultat des travaux de recherche menés par ses étudiants gradués et dans l'esprit des règles qui régissent le dépôt et la diffusion des mémoires et thèses produits dans cette Institution, **l'Université du Québec à Chicoutimi (UQAC)** est fière de rendre accessible une version complète et gratuite de cette œuvre.

Motivated by a desire to make the results of its graduate students' research accessible to all, and in accordance with the rules governing the acceptation and diffusion of dissertations and theses in this Institution, the **Université du Québec à Chicoutimi (UQAC)** is proud to make a complete version of this work available at no cost to the reader.

L'auteur conserve néanmoins la propriété du droit d'auteur qui protège ce mémoire ou cette thèse. Ni le mémoire ou la thèse ni des extraits substantiels de ceux-ci ne peuvent être imprimés ou autrement reproduits sans son autorisation.

The author retains ownership of the copyright of this dissertation or thesis. Neither the dissertation or thesis, nor substantial extracts from it, may be printed or otherwise reproduced without the author's permission.

ABSTRACT

Many systems and infrastructures developed by human beings frequently encounter deficiencies, stop functioning or even fail during severe weather conditions due to ice accumulation. One of the common methods to prevent snow and ice accumulation on exposed surfaces is the use of chemicals such as freezing point depressants. They should be applied during storms or just before ice accumulation which is practically difficult. Also these chemicals adversely affect the environment. New environment-friendly methods are necessary to be developed. An ideal solution can be covering the structures with a coating capable of inhibiting or reducing the bonding between snow or ice and solid surfaces.

A solid surface with a water contact angle greater than 150° is called superhydrophobic. Desiring superhydrophobicity, a surface should satisfy two criteria, nano/micrometer scale roughness as well as low surface energy. Many applications in industry and in everyday-life can be benefited from this extreme water-repellence if one can develop a durable, environment-friendly superhydrophobic coating.

In the present study, the hydrophobicity of the surfaces with submicron roughness prepared by spin-coating of metallic nanoparticle colloids on aluminum and copper substrates was studied. Three colloids of silver nanoparticles and two colloids of copper nanoparticles with different size distributions were synthesized by chemical reduction methods. Silver particles were found to be stable enough to make the model surfaces but copper particles were unstable and not suitable for this application.

Regardless of nanoparticle type, hydrophobic surfaces could not be achieved by making rough surfaces by only one layer of coating. By adding a second layer of coating, all three types of silver nanoparticles resulted in coatings with high degree of superhydrophobicity on metallic substrates. Due to the similar shapes of nanoparticles, the difference in observed contact angles could be related to the particles sizes. The particles with the average size of ~263 nm had the highest contact angles whereas the particles with average size of ~195 nm or ~360 nm showed lower values.

The anti-icing behaviour of these superhydrophobic films was studied under atmospheric icing conditions. On aluminum, two layer coating of 263 nm particles could reduce the ice adhesion up to 8.1 times. This value was equal to 4 on copper substrates with similar coating. The copper based samples could keep their ice adhesion reduction even after five ice removal test.

RESUMÉ

Plusieurs systèmes et infrastructures stratégiques sont affectés ou cessent de fonctionner pendant les périodes hivernales accompagnées de givrage atmosphérique. Une des méthodes couramment utilisées pour diminuer les charges de glace ou de neige est l'utilisation des produits chimiques pour abaisser le point de congélation. Cependant, ces produits doivent être appliqués pendant le givrage ou juste avant l'accumulation de la glace, ce qui est difficile en pratique. De plus, ces produits sont nocifs pour l'environnement. C'est ainsi que de nouvelles méthodes, plus efficaces et moins nocives, sont nécessaires. Une solution idéale serait de recouvrir les structures exposées de revêtements capables de réduire ou de neutraliser l'adhésion de neige ou glace aux surfaces exposées.

Une surface caractérisée par un angle de contact de 150° ou plus avec les gouttelettes d'eau déposées est dite superhydrophobe. Pour obtenir une telle surface, une des solutions suggérées est la création de surfaces nanostructurées avec faible énergie de surface. De telles surfaces hydrophobes ont de nombreuses applications si elles sont durables et n'ont pas d'effets nocifs sur l'environnement.

Dans cette étude, des surfaces superhydrophobes nanostructurées ont été obtenues par le recouvrement de surfaces d'aluminium ou de cuivre avec des nanoparticules métalliques. Trois colloïdes différents de nanoparticules d'argent et deux colloïdes de nanoparticules de cuivre ont été synthétisés par des méthodes de réduction chimique (chemical reduction). Il s'est avéré que les particules d'argent sont assez stables pour cette application par rapport particules de cuivre qui ne le sont pas suffisamment.

Indépendamment du type de nanoparticules, des surfaces hydrophobes n'ont pas pu être réalisées avec une seule couche. En ajoutant une deuxième couche, tous les types de nanoparticules ont formé un revêtement avec d'excellentes propriétés hydrophobes, mais avec des angles de contact différents. En raison des formes similaires des nanoparticules, cette différence entre les angles de contact pourrait dépendre de la dimension de ces particules. En effet, les particules avec une taille moyenne de ~263 nanomètres présentent les angles de contact les plus élevés, tandis que celles avec une taille moyenne de ~195 ou de ~360 nanomètres présentent des valeurs plus basses.

Le comportement des revêtements superhydrophobes élaborés a été étudié dans des conditions de givrage atmosphérique. Sur une surface d'aluminium protégée par un revêtement de deux couches de particules de 263 nanomètres, l'adhérence de glace a été réduite jusqu'à 8.1 fois. Cette réduction de l'adhérence était de 4 fois dans le cas de substrats à base de cuivre dans les mêmes conditions. Les échantillons à base de cuivre nanostructurés ont pu garder leurs propriétés glaciophobes même après cinq essais de déglaçage.

ACKNOWLEDGMENTS

This work has been carried out within the framework of the NSERC/Hydro-Quebec/UQAC Industrial Chair on Atmospheric Icing of Power Network Equipment (CIGELE) and the Canada Research Chair on Engineering of Power Network Atmospheric Icing (INGIVRE) at the University of Quebec in Chicoutimi.

I would like to thank all who gave me the possibility to complete this research. I wish to express my best appreciation to my director, Prof. Masoud Farzaneh, for his patience, guidance, encouragement and support of my research work. It was great to have the privilege to work with him and learn from his expertise in the past three years.

My special thanks to my co-director Dr. Dilip K. Sarkar for his gentle instructions, many technical discussions and suggestions throughout this project and of course reading and editing my thesis.

Special thanks to Mrs. Hélène Grégoire, CNRC Chicoutimi for providing access to FESEM. I am also grateful to INRS, Varennes, for XRD measurements. Thanks to Mr. Jian Hung Lin, Center for Condensed Matter Sciences, National Taiwan University, Taiwan, for preparing smooth silver-coated silicon samples. I would also like to thank Dr. Dmitry V. Shtansky, Moscow Institute of Steel and Alloys, for optical profilometry.

I debt to Dr. Jean Perron, Mrs. Caroline Blackburn and the technicians of Anti-icing Materials International Laboratory, UQAC, for providing access to The Centrifuge Adhesion Test System.

I would also like to thank the research colleagues, professionals and technicians in CIGELE, for their support and help. These people include Dr. Sergei Kulinich, Dr. Richard Menini, Dr. Hossein Hemmatjou, Dr. Majid Kermani, Pierre Camirand, Xavier Bouchard, and Denis Masson among many others. I am thankful for the time they have taken with me.

I am pleased to have participated in the Ph.D. program offered by the University of Quebec in Chicoutimi, where I had the chance to develop my skills and find forward-looking friends.

Finally, I want to express my deepest thanks and appreciation to my dear wife, Azadeh, for her never-ending support, understanding and patience in all the situations.

TABLE OF CONTENTS

LIST OF FIGURES

LIST OF TABLES

LIST OF SYMBOLS AND ABBREVIATIONS

θ_0	Contact angle value for smooth, planar, homogenous and rigid surfaces
γ_{SV}	Surface tension of solid-vapour interface
γ_{SL}	Surface tension of solid-liquid interface
γ_{LV}	Surface tension of liquid-vapour interface
θ_A	Advancing contact angle
θ_R	Receding contact angle
θ^W	Contact angle value for rough surfaces predicted by the Wenzel model
θ^{CB}	Contact angle value for rough surfaces predicted by the Cassie-Baxter model
EG	Ethylene glycol
PVP	Polyvinylpyrrolidone
MeOH	Methanol
PTFE	Polytetrafluoroethylene
LLL	Liquid-like layer
LBL	Layer by layer
CBD	Chemical bath deposition
CVD	Chemical vapour deposition
PVD	Physical vapour deposition
AFM	Atomic force microscopy
SEM	Scanning electron microscopy
FTIR	Fourier transform infrared spectroscopy
XRD	X-ray diffraction

CHAPTER 1

INTRODUCTION

1.1 The Problem of Icing

Atmospheric icing phenomena happen when the surfaces of exposed structures are in contact with supercooled water drops or snow particles. In cold climate regions accretion of ice creates several problems, including damages for the civilian, industrial or military equipment such as automobiles, ships, aircraft, dams, telecommunication and overhead power networks. Each year, numerous failures due to ice accumulation are reported from Canada, the United States, Russia, Iceland, Japan, China, etc. [1].

In the specific case of power transmission lines, high adherence of ice or wet snow to both the metallic and insulator surfaces results in heavy ice build-up. Static ice weight overloads the towers and leads to sagging in power conductors. This ice build-up, with a typical thickness of a few centimetres, is aerodynamically unstable [2]. It increases the amplitude of wind-induced dynamic oscillations, galloping, and decreases the damping rate, which leads to high mechanical stress on conductors, insulating supports and towers. When the accumulated ice suddenly drops off a conductor, excessive mechanical tensions are generated [3] which cause high-amplitude traveling waves in conductors. It also increases the possibility of low clearance between the adjacent high-voltage conductors or between conductors and ground cables towers [4,5]. Ice-covered insulators are more susceptible to have arcs and flashovers, which may incur voltage sags, spikes or even complete power loss [6-10]. As an example of catastrophic destructions from icing, one can refer to the storm that hit the southern parts of Quebec and Ontario and some states of USA in January 1998, downing several kilometres of power lines, causing the collapse of

hundreds of steel towers and breaking thousands of wooden sub-transmission structures [2,5,11].

Preventing ice build-up has long been a technological challenge. Ice, with its broad range from snow to glaze, can stick to almost anything. There have been many attempts to reduce ice adhesion, but fundamental physics of ice adhesion is not yet well understood. Many de-icing methods have been developed [12] but none of them is satisfactory. In fact none fulfils two major requirements for a true solution: (a) high reduction in ice adhesion, and (b) long service-time. Traditional approaches rely on mechanical breaking of ice or using chemicals to melt the accreted ice, which are temporary solutions [13]. There are some effective methods involving the melting of ice by heating (Joule effect or high frequency current), but they require very high energy [14,15]. Although de-icing fluids can be applied to ice-covered structures to eliminate such ice build-ups, these substances can have significant negative environmental impacts [16]. Electrolysis is another approach found to be effective for removing ice from certain surfaces [17], however it is not yet a practical method. All of these de-icing techniques are employed where there is already some ice formed. Several types of anti-icing fluids are used to prevent ice build-up on aircraft surfaces, but the durability of protection depends on precipitation conditions and the properties of fluids. Moreover, anti-icing fluids such as ethylene glycol are toxic and environmentally unfriendly.

An alternative way of preventing ice accretion would be making a durable solid anti-icing coating which can inhibit ice accumulation rather than eliminating it after accretion [12]. Such coatings are called anti-icing or icephobic materials. Coating any surface with

anti-icing materials can be an effective way of reducing/preventing ice accretion. Recently, several coatings for icephobic application have been tested and reported but the best results belonged to greases and lubricants and not to solid coatings [18]. There are reports on methods toward developing a hydrophobic coating to reduce the adhesion of ice on pavements and highways [19,20]. Polymers with low critical surface tension such as organopolysiloxane and tetrafluoroethylene were examined. Those coatings exhibited satisfactory traction on wet roads; they produced very low runoff water contamination and demonstrated a significant reduction in ice adhesion. Another investigation revealed that fluorinated and polysiloxane coated surfaces had the poorest wetting by water and are the best candidates for icephobic coatings [21]. For real applications the coating should be hard, durable and be able to sustain extreme weather conditions. It is expected that the path to icephobicity passes through the materials with low degree of wettability [22,23].

1.2 Wetting Phenomena

Study of wetting properties of solids by liquids and interfacial phenomena are not only important in fundamental research [24], but are also significant technological issues [25]. These are of main concern in the context of microfluidic dynamics, textiles, lubrication, adhesives and non-sticking surfaces among others. In macroscopic scales, wetting property of a particular solid can be examined with contact angle measurement. A water contact angle less than 90° indicates a hydrophilic surface while an angle greater than 90° presents a hydrophobic one. If the water contact angle is higher than 150°, the surface is called superhydrophobic [26].

In nature, several plants and insects show very high water contact angles, for instance lotus leaves or butterfly wings [27,28]. Searching for the origin of superhydrophobicity, scanning electron microscopy reveals that lotus leaves have a high degree of microscopic roughness, as shown in figure 1.1 [29]. In addition, the outermost layer of lotus leaf is composed of a waxy material which is inherently hydrophobic.

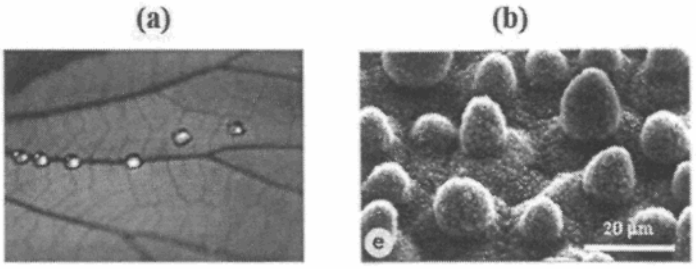

Figure 1.1: (a) Water drops on lotus leaves (nelumbo nucifera) with very high contact angles of 150°, rolling off the surface, (b) a SEM image of surface structure of lotus leaf [29].

Trying to mimic these extremely water-repellent surfaces, several approaches have been developed and documented [30] which can be beneficial. For example, it will be convenient to have windows that can be cleaned by a slight rain. However, there is always a question about the durability of such coatings when it comes to their wide range uses. The same principle would result in less adhesion strength between solids and ice or snow. It is expected that ice wouldn't adhere to a surface that has a thin superhydrophobic coating.

A superhydrophobic surface requires micro/nanometer scale surface structures. Nanoscience involves materials with specific properties that are attributable to nano-sizes, with at least one dimension limited to 1-1000 nm [31]. Different definitions for

nanoparticles can be found in the literature. In some references nanoparticles are defined as solid colloidal particles ranging in size from 10 nm to 1 μm [31,32]; other authors considered nanoparticles to be a collection of atoms or molecules with an average diameter up to 100 nm [33]. More detailed definition can be found in [34] where the author provides finer size scales from quantum (0.1 nm), molecular (1 nm), nanoscale macromolecular (10 nm), mesoscale molecular assemblies (100 nm), microscale (1000 nm), and macroscale. Nanoparticles usually exhibit unique physical and chemical properties (due to their shape, small size, high surface-to-volume ratio, and quantum confinement effects) that are very different from atomic state or bulk material [35]. It is possible to use nano-particles to engineer nanostructured thin coating layers which exhibit superhydrophobic properties [36]. This is the basis of this research.

1.3 Main Objectives

The proposed research investigates the feasibility of developing an innovative superhydrophobic coating based on metallic nanostructures and is intended to effectively reduce ice accretion. For this purpose, the research is concentrated on thin films of silver and copper nanoparticles. The objectives of this research project are:

1. Controlled synthesis of metallic nanoparticles and then nanostructured thin films using those metallic nanoparticles,
2. Passivation of those nanostructured metallic thin films by chemical and physical surface modification methods, to achieve low energy surfaces,

3. Characterization of the nanostructured metallic thin films by morphological and chemical analyses of the surface,
4. Studying the effect of surface parameters on wettability under different conditions, and evaluating ice accretion and ice adhesion strength on those samples under simulated atmospheric icing conditions (supercooled water droplets impacting the sample surface at subzero temperature).

1.4 Methodology

Considering the above objectives, the methodology employed includes the following tasks:

- *Synthesis of metallic nanoparticles and nanostructured metallic thin film coatings:* Silver and copper nanoparticles prepared in respective solutions (in acid, base and alcohol media) were individually spin coated on to copper and aluminum substrates to obtain nanostructured silver and copper thin films.
- *Passivating the nanostructured silver and copper thin films:* The nanostructured metallic thin films were passivated using chemical and plasma modifications. In the chemical method, the nanostructured thin films are immersed in solutions of different fatty acids, namely, lauric acid, palmitic acid, and stearic acid to obtain low surface energy resulting from the orientation of the hydrophobic functional groups outward the surface. In the plasma modification, a rf-sputtered PTFE thin films are coated onto the nanostructured thin films using an inductively coupled plasma.

- *Characterization of the nanostructured silver and copper thin films:* The surface morphology of nanostructured metallic thin films were characterized by atomic force microscopy (AFM), field emission scanning electron microscopy (FESEM), and optical profilometry. The chemical and structural characterization was performed using Fourier-transform infrared spectrometry (FTIR), X-ray diffraction (XRD) and UV-vis spectrophotometer. Wettability tests were carried out via contact angle measurements using a contact angle goniometer. Ice accretion and it adhesion tests were performed by centrifugal ice adhesion reduction test apparatus designed, developed and inter-phased in-house at CIGELE Laboratories.

1.5 Statement of Originality

As expressed extensively in chapter 2, there are previous studies on coatings and thin films toward ice adhesion reduction so as to make removal of ice easier. Also some reports can be found discussing the potential use of nanoparticles to obtain superhydrophobic surfaces. However, making nanostructured superhydrophobic coatings to prevent ice from adhering to solid surfaces has not been so far reported according to our knowledge.

Therefore, coupling these two ideas, i.e. using superhydrophobic surfaces based on metallic nanoparticles in view of prevention of ice adhesion, is a novel approach. The research work presented in this dissertation is a part of investigation series currently in progress in the Industrial Chair on Atmospheric Icing of Power Network Equipment (CIGELE) and the Canada Research Chair on Atmospheric Icing Engineering of Power Network (INGIVRE) at the University of Québec at Chicoutimi.

1.6 The Outline of Thesis

This dissertation introduces and discusses the different aspects of model superhydrophobic surfaces based on metallic nanoparticles in atmospheric icing conditions, in the following order:

- Chapter 1 introduces the problem of atmospheric icing, and wetting phenomena;
- Chapter 2 provides a brief literature review of atmospheric icing, superhydrophobicity and metallic nanoparticles;
- Chapter 3 describes the details of experimental processes related to nanoparticle preparation, coating and passivating and characterization methods;
- Chapter 4 discusses the properties of achieved nanoparticles in detail.
- Chapter 5 presents the results and discussion of water behaviour on developed hydrophobic surfaces;
- Chapter 6 provides the results and discussion of atmospheric-like icing on various achieved hydrophobic surfaces; and
- Chapter 7 includes general conclusion and recommendations for future studies.

CHAPTER 2

BACKGROUND

2.1 Atmospheric Ice Accretion on Outdoor Equipment

Atmospheric ice deposition on outdoor equipment can adversely affect their operation or even result in serious and costly damages [1,37]. An example is the mechanical failure of power transmission lines and towers due to the static load of accreted ice, or dynamic stresses of ice shedding or wind-induced galloping [2]. It can also lead to loss of insulation [6-10] and electric arcs or flashovers between power lines and metallic supports, the latter being at ground potential. Wind loads can deteriorate the situation by intensifying the stresses on the mechanical parts. Engineers need to design the above structures with considerable margins to ensure their ability to withstand icing and windy conditions [38]. All these considerations increase the weight and cost of the infrastructures. Icing problem can impact many other systems such as ships, aircraft, vehicles, etc. Our interest here lies in the icing process in order to develop a method to reduce its adhesion to surfaces and eliminate related harmful effects.

2.1.1 Supercooled Water Drops

Water drops can be cooled down much below bulk water freezing point (0°C). Figure 2.1 illustrates Levine's results [39] showing that tiny water drops may remain in liquid state below 0°C and their freezing point is size-dependent. For a water drop below the freezing point, commonly referred to as supercooled droplet, the liquid state is thermodynamically unstable. The most stable state for such droplets is the solid state which means an arrangement of water molecules in a lattice. This requires the movement of some molecules

and the gain of a higher degree of order, which is not favourable, according to the second law of thermodynamics. The net result is the lower freezing temperatures, seen in figure 2.1.

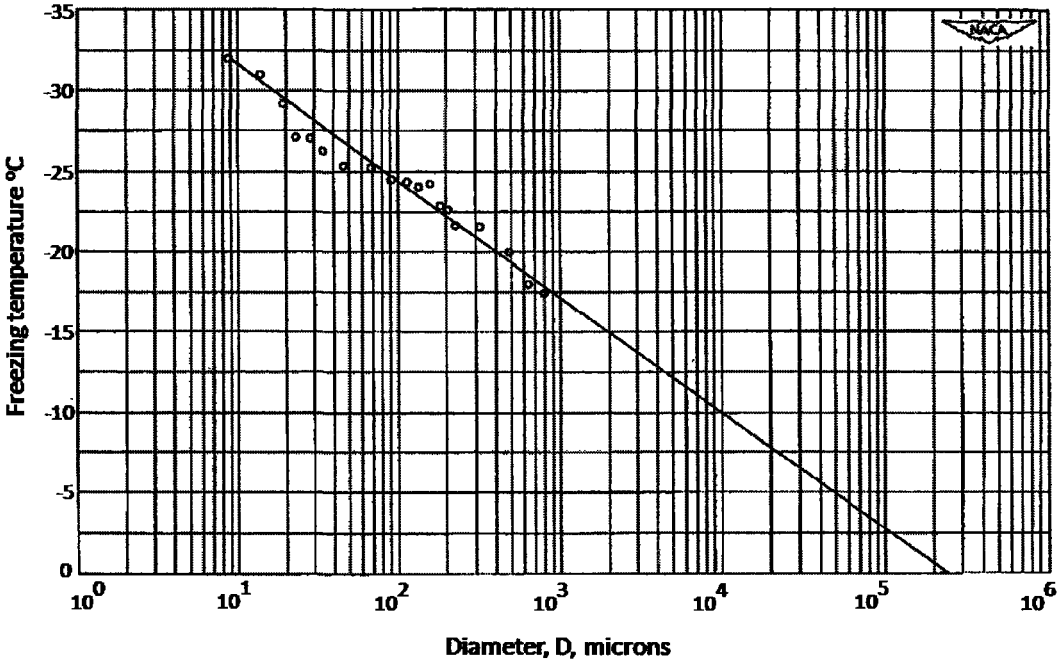

Figure 2.1: Freezing temperature of small water drops versus size [39].

The freezing process may be facilitated in presence of any substance acting as a freezing nucleus, which induces growth of an ice crystal about itself [40].It is suggested that a material whose basal plane structure is similar to that of ice can be an effective nucleating agent [41]. Heterogeneous nucleation can take place by a variety of mechanisms. Theoretical studies and experimental measurements have shown that the ice nucleating ability of a particle is size-dependent and influenced by other physical and chemical factors [42]. This phenomenon could be seen in clouds or fogs above -30°C where supercooled

droplets convert to ice particles through the presence of heterogeneous ice nuclei [43]. Levine in his studies also concluded that smaller droplets have less probability to contain nuclei, and therefore lower freezing temperature [39]. However, in clouds below -30°C ice particles densities are more than ice nuclei densities [44] and it is believed that some supercooled water drops freeze homogenously [45].

Both the heterogeneous and homogenous nucleation phenomena inside the clouds are slow processes. For the objects in high altitudes, supercooled water droplets may impinge on exposed surfaces. An effective nucleus has a crystal structure similar to ice which allows water crystallize by repeating its structure. Thus, the best nucleus for ice is a tiny piece of ice. That is why supercooled water droplets tend to rapidly join the ice layers covering the outdoor structures and objects.

2.1.2 Types of Atmospheric Icing

Atmospheric icing appears when supercooled water drops approach the exposed surfaces of outdoor equipment. According to meteorological conditions, two types of ice formation could take place, namely in-cloud icing and precipitation icing. In-cloud icing occurs when the supercooled water droplets in a cloud come in contact with an exposed object. This kind of icing is relevant to the aircraft flying through clouds or the equipment installed high up in mountains.

Precipitation icing can happen in any place regardless of altitude during freezing rain. When a warm layer of air (above 0°C) is trapped between two layers of cold air (below 0°C), freezing rain may occur. Precipitation starts falling down as snow and reaching the

warm air, the snow particles melt to water. This water encounters the low-level cold air and becomes supercooled. Freezing drizzle has relatively smaller and lighter drops and originates from low level clouds whereas freezing rain is from higher clouds.

Atmospheric icing may arise as one of three types: glaze, hard rime and soft rime [46]. An alternative to them, wet snow, is of relatively less importance. Ice type is determined by supercooled droplet size, air temperature, wind speed, and properties of objects being hit by drops. The relationships of ice types with droplet size, air temperature, and wind speed are shown in figure 2.2, adopted from [47].

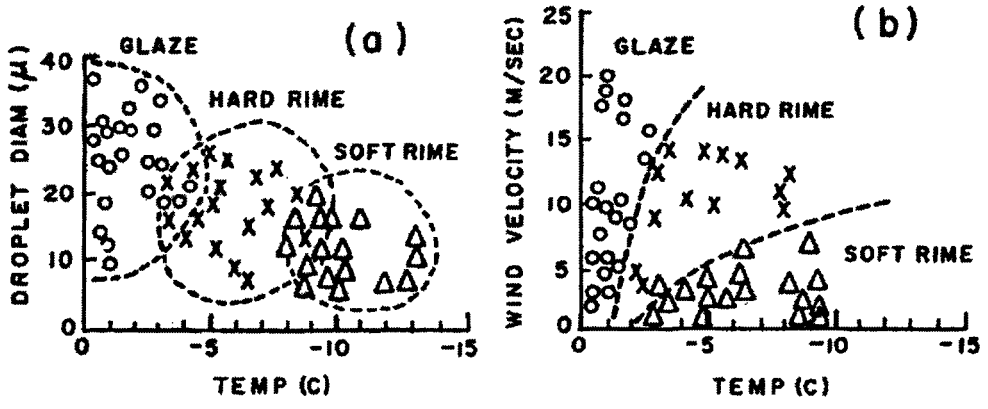

Figure 2.2: Atmospheric icing types as a function of (a) droplet diameter and air temperature, and (b) wind velocity and air temperature [47].

Glaze is a homogenous and transparent wet ice, depositing when relatively large supercooled droplets of freezing rain hit a subzero. Glaze accumulation happens at temperatures close to the melting point and under wet growth regime [48]. Lower temperatures create hard rime and soft rime. Rime ice accumulates when smaller supercooled droplets are in contact with dry objects below the freezing point [49]. This kind of ice mostly appears in mountains and at low wind speeds. Table 2.1 summarizes the

appearance, density, and formation conditions for each of the icing types. Among three types of atmospheric ice, glaze is denser and exerts larger static/dynamic forces to the equipment. Also it conducts electricity easier and is more dangerous for the performance of the components of electric networks.

Table 2.1: Types and characteristics of atmospheric icing [50,51].

Type of ice	Appearance	Density (g.cm-3)	Conditions of formation
Glaze	Hard, well-bonded, generally clear homogeneous ice	0.8-0.9	Supercooled water droplets at a temperature close to freezing (0 to -3° C) and wind speeds of 1-20 m/s
Hard rime	Hard, granular white or translucent ice growing along the direction of the wind	0.6-0.8	Supercooled water droplets at a temperature of -3 to -8° C, wind speeds generally 5-10 m/s
Soft rime	White, opaque, granular ice with delicate structure only loosely bonded, growing along the direction of the wind	< 0.6	Supercooled water droplets at a temperature of -5 to -25° C, and low wind speed (1-5 m/s)

2.1.3 Ice Adhesion

Ice forms strong bonds with the surface on which it freezes. The required stress to de-bond the ice from the surface is usually referred to as ice adhesion stress. Many parameters can influence the adhesion of ice to other materials. In addition to substrate properties, the conditions of ice formation can intensify the adhesion. Briefly, the adhesion is stronger when there is a lower freezing rate, more water on the material, higher droplet momentum, wider contact area, and lower air temperature down to a point.

The fundamental physics of ice adhesion is not well known yet. The bonds responsible for adhesion at the ice-solid interface are not unique. In [52] the authors divided the mechanisms of ice adhesion into the following categories:

- Electrostatic: There is evidence that some kinds of electron transfer [53] or proton ordering [54] happen at the interface of ice and solids, depending on the nature of material. These phenomena result in electrostatic attractions.
- Diffusion and mechanical: Penetration and diffusion of one material into the matrix of the other can help the materials adhere well. In presence of microscopic pores in a solid, a water drop can enter and freeze inside the pores. The expansion of water after freezing leads to a strong mechanical interlocking between the ice and substrate.
- Chemical: Materials adhere when chemical bonds are formed between them. Different types of bonding are likely to happen: hydrogen bonds, dipole-dipole bonds, dipole induced bonds, etc.

Chemical bonds are also of different types: electrical dipole-dipole interactions are intermolecular forces between polar molecules, such as water molecules. These forces are highly dependent on distance between the molecules and can be very strong when the molecules are close to each other. The attraction strength increases when polarity increases. Dipole- induced interactions (or Van der Waals forces) are mainly important for non-polar molecules and arise from temporary mismatch of electron clouds and nuclei. These weak forces act between all kinds of atoms or molecules. A hydrogen bond is an attraction interaction in which a hydrogen atom is attracted to two atoms (especially electronegative atoms) and acts like a bridge between them [55]. Usually, there is a considerable amount of oxides or adsorbed water molecules on the majority of practical solid surfaces, which can give rise to strong interaction with water molecules during freezing.

2.1.4 Ice Adhesion Measurement

Many investigators have studied the adhesion of artificial and atmospheric ice on various materials with a variety of surface properties [56,57]. Many methods have been used [58], for example, the techniques applying torsion shear, lap shear, cylinder torsion shear test, axial cylinder shear; methods such as cone test tensile, test, peel test or blister test [59], impact tests [21], laser technique [60], electromagnetic tensile tests [61], scratch tests [62] and so on. Each method was found to have its advantages and limitations.

The difficulty of reliable and meaningful ice adhesion measurements was reported long ago [63]. Some of the earliest studies on ice adhesion were carried out by Loughborough and Haas [64,65]. The shear strength of refrigerated ice was found to be about 1.72 MPa. Adhesion of artificial ice to metals was also measured to be from 0.85 MPa on copper to 1.52 MPa on aluminum. The authors noted a poor correlation between low ice adhesion and water repellency [64]. The adhesive strength of natural rime and glaze impact ice on aluminum power cables was studied by Phan et al. [66], Druez et al. [67], and Laforte et al. [68], and the adhesive shear strength for hard rime was shown to vary 0.075 to 0.12 MPa. Both wind velocity and surface roughness appeared to increase the adhesive shear strength.

The first rotating centrifugal force method to measure adhesive strength of thin films of ice on metal was reported by Beams et al. [69]. Raraty and Tabor [70] also used the same technique to measure the adhesive shear strength of ice on polished-cleaned stainless steel. Stallabrass and Price [71] and Itagaki [72,73] used the rotating rod centrifugal method and found the adhesive shear strength of ice to be 0.03 to 0.07 MPa at -6°C; 0.03 to 0.16 MPa at -1to -15°C. Kozitsokii [74] studied the effect of surface roughness on 304 SS plates. The

author considered three types of surfaces: a machined surface, a mat surface finish, and a mirror polish. Mean adhesive shear strengths were 0.6 MPa, 0.26 MPa, and 0.07 MPa respectively, for a snow-ice layer 0.1-0.2 cm thick. Thus surface roughness increased the shear strength by a factor of 10.

It is generally hard to compare the results of different ice adhesion values reported in the literature. Many parameters have to be considered when one tends to compare various investigations, for example ice formation conditions (e.g. airspeed, air temperature, droplet size, liquid water content, etc.), sample area and thickness, applied strain rate, and so on. Such substantial details are usually not mentioned clearly, or not reproducible. Strain rate has strong effect i.e. ice is ductile with viscoelastic behaviour at low strain rates, while brittle at high strain rates. The important issues in ice-adhesion measurement are reliability and reproducibility. An improved reproducibility of shear measurements requires uniformity in the force applied to the sample, enough ice-sample attachment area, and constant strain rate. One practical approach is to perform comparative or differential study; by applying ice both on known reference samples and on sample surfaces in completely similar way and then express the results in percent of change in shear strength.

2.1.5 Liquid-like Layer

When the outermost layers of most solids approach the bulk melting temperatures, the molecular structure tends to a kind of disordered state with some attributes of both the solid

and liquid phases. It was found that on most of the ice interfaces a thin liquid or liquid-like layer (LLL) exists at temperature below the ice melting point [75,76].

One of earliest qualitative justifications of existence of such a layer and its extension to hundreds of molecular layers into the bulk was given by Weyl [77]. Following this report, various experimental methods were used to study the LLL, such as some dynamic measurements sensitive to the hydrodynamic properties of the layer (e.g., viscosity) [78], ellipsometry [79], photoelectron spectroscopy [80], nuclear magnetic resonance [81] and so on. Each of these experiments is based on a specific property of the LLL, so its thickness measurement can differ from the thickness measured by another approach. In addition to experimental investigations, many researchers tried to prove the existence of the LLL theoretically. For a brief list one can refer to [82].

A common observation in different experiments is temperature dependence of LLL. The thickness of the LLL increases rapidly as temperature rises. As shown in figure 2.3 having the temperature near bulk melting point, the thickness of the LLL increases rapidly up to micrometer scale. This is the temperature range in which glaze, the most bothering atmospheric ice, is most likely when precipitation drops are large and wind is strong. If one can find a surface coating capable of repelling water (and thus probably the LLL), such a coating is expected to effectively reduce ice adhesions and/or accumulation. Superhydrophobic materials show very low affinity to water, and are good ice-repellent candidates, as discussed in the following section.

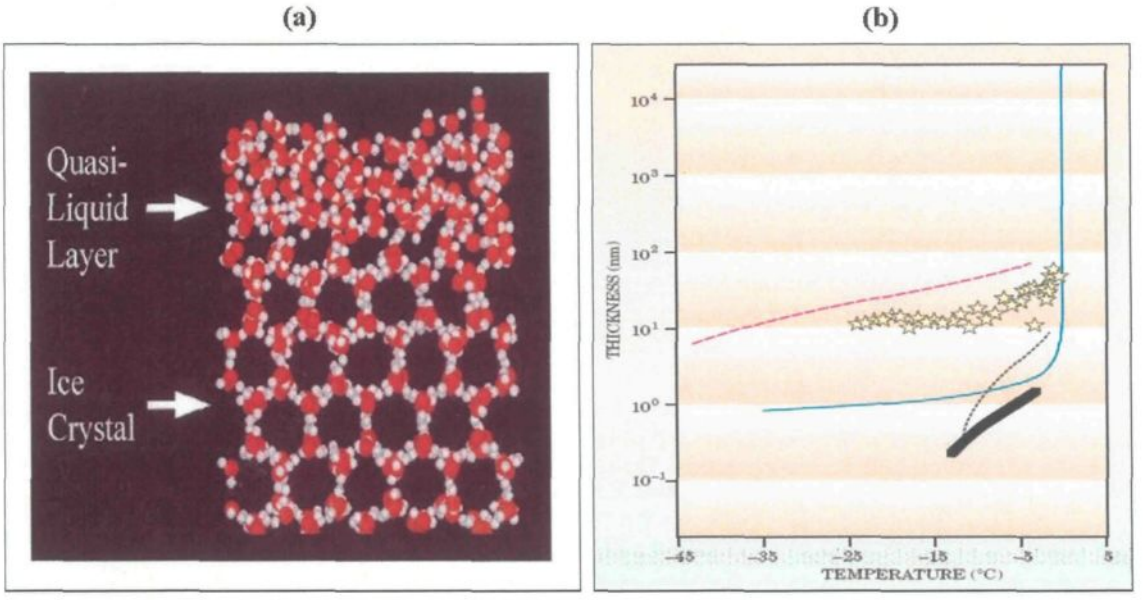

Figure 2.3: (a) Molecular dynamics simulation of the LLL structure at 265K, (b) the thicknesses of the LLL by proton backscattering (red dashed line) [83], x-ray scattering using a glass interface (black dashed line) and a silicon interface (black bold line) [84,85], AFM (stars) [86] and relegation (blue solid line) [87]

2.2 Wettability and Superhydrophobicity

2.2.1 Surface Energy and Surface Tension

Although plasma is the most abundant phase of matter in the world, in our daily life we face the other three familiar states; solid, liquid and vapour. Wetting phenomena happen in the points where all the three states are in contact. In other words, wetting includes the behaviour of intersection of three interfaces, solid-liquid, solid-vapour, and liquid-vapour.

An interface is the boundary between two phases, and when one side is a vapour or gas, the other is called a surface. The properties of surfaces are different compared to the

interior or bulk. One important aspect is the extra energy associated with the surfaces, also known as surface energy. When a solid material is cleaved to two pieces, the applied energy is used to break the chemical bonds between the atoms of the material and the conservation of energy results in the increment in energy of these atoms. The energetic atoms tend to reduce their energy, so they undergo relaxation (a slight rearrangement in surface layers) and reconstruction (displacements of the surface atoms) as well as adsorption and oxidation in presence of air. But the surface energy remains still high. For liquids, it is common to use the term of surface tension, a vector quantity, instead of surface energy, both having a dimension of force per unit length (Nm^{-1}) or energy per unit area (Jm^{-2}). In the case of liquids, the unfavourable surface energy is lowered by minimizing the amount of exposed area and also by surface relaxation [88]. The direction of surface tension is inward the liquid, determining the curvature of free surfaces of liquids, rising the liquids in tiny vertical pipes and wetting the solid surfaces. The measured surface tensions of some common liquids are listed in appendix A.

For crystalline materials, many of physical and chemical properties are directional and dependent on the microstructural attributes. Surface energy of metals has been subject of numerous theoretical [89,90] and experimental investigations [91]. Appendix B includes the values of surface tension for some common metals. For more complete list one can refer to [92].

2.2.2 Contact Angle as Wettability Indicator

Wetting occurs when a liquid drop contacts a solid surface. As a result, fractions of both the liquid surface and solid surface are reduced while a solid-liquid interface appears. For a given solid, a low-surface-tension liquid will spread easily while a high-surface-tension one tries to keep its drop shape. Similarly for a given liquid, a high-surface-energy solid tends to be covered (or wetted) in contrast to low-energy surface one which does not absorb the liquid. If the liquid does not spread to make a thin layer, it will sit as a spherical-cap-like droplet.

The most common quantitative indicator of wettability is contact angle. It is believed that contact angle measurement is a reliable method to study the surface energy. The contact angle value for ideal surfaces (smooth, planar, homogenous and rigid), θ_0, is given by Young's equation [93]

$$\cos\theta_0 = \frac{\gamma_{SV} - \gamma_{SL}}{\gamma_{LV}} \qquad \textbf{(Eq. 2.1)}$$

where γ_{SV}, γ_{SL} and γ_{LV} are surface tensions for the solid-vapour, solid-liquid and liquid-vapour interfaces, depicted in figure 2.4.

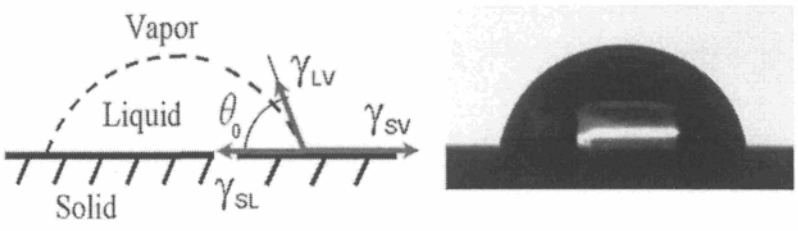

Figure 2.4: Interfacial tensions and contact angle.

Young equation gives the contact angle which corresponds to minimum energy of a drop on a smooth solid surface [94]. In this equation, the solid surface is considered as a hard homogenous material which doesn't reshape or dissolve and there is no liquid penetration.

When the selected liquid is water and $\theta_0 < 90^\circ$, the solid is named hydrophilic (having a substantial affinity for water) and for $\theta_0 > 90^\circ$ the solid is hydrophobic (lacking affinity for water). Actually, hydrophobic materials attract water but the tendency between water and material molecules is weaker than between water molecules. In the extreme case of hydrophilicity, $\theta_0 = 0^\circ$, water wets the entire surface and spreads completely to form a thin layer. On the other hand, the surfaces with contact angles more than 150° are called superhydrophobic or ultrahydrophobic.

2.2.3 Contact Angle Measurement

The different methods applied to measure the contact angles can be categorized into two main groups based on the state of droplet during procedure:

- Static: the drop is placed on the surface before measurement and its volume is momentarily constant while the contact angle is measured.
- Dynamic: the contact angle is studied when the drop is being enlarged, reduced or moved. The boundary of liquid-solid interface is evolved during the measurement process.

Static methods can give the values of equilibrium contact angles. A liquid droplet of 3 to 8μL is placed on the surface and the needle is removed so that the drop can take its shape freely without any alteration due to presence of needle. The condition of constant volume of drop is required temporarily for measuring the contact angle and does not mean that the volume is kept constant continuously. Many events may alter the drop volume, such as liquid evaporation, dissolving the solid in to liquid or vice versa, chemical reaction between the solid and liquid and so on. Sometimes, the time-dependent evolution of droplet on the surface can provide useful information and usually there is a facility in measuring systems to record the variations of contact angle versus time.

Dynamic contact angles describe the evolution at the liquid-solid boundary during the wetting and de-wetting processes. The main purpose of dynamic method is to achieve the advancing and receding contact angles. During the process the needle remains in the drop throughout the whole measurement so the selection of proper size is important to have the results not affected by the presence of needle. When there is a relative displacement between solid surface and needle the velocity should be selected properly. A reliable and stable boundary is not formed instantaneously but needs some time before equilibrium is reached. The similar argument is correct when there is a liquid injection or suction to alter the drop size. The needle diameter, droplet size and injection rate should be selected precisely.

Another dynamic method for contact angle measurement is by tilting the solid surface. The solid surface is slowly tilted from horizontal state and the contact angles are constantly measured. The acceptable contact angle is the one just before the drop starts to roll. The

inclination angle of surface with horizontal plane is called sliding angle. It is worth mentioning that this procedure is highly dependant to the size of liquid droplet. Each method has it advantages and limitations and the proper method should be selected according to the actual experiment.

2.2.4 Contact Angle Hysteresis

Young's equation predicts a unique value for contact angle, but in reality a liquid drop on a solid does not show just a single contact angle. If a drop is placed on a static horizontal solid surface, the contact angle is named as sessile. When there is a relative movement between the droplet and the surface, for instance because of tilting, as in figure 2.5, there will be a change in the contact angles. Another example is when the volume of droplet increases or reduces because of injecting/sucking the liquid to/from droplet with a needle. The contact angles at the wetting and de-wetting edges of droplet are called as advancing and receding, respectively. Usually the sessile contact angle is greater then receding angle, θ_R, and less than advancing angle, θ_A.

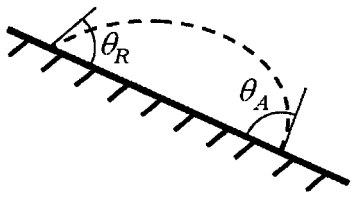

Figure 2.5: Advancing and receding contact angles of a liquid drop on a tilting solid surface.

Experiments have shown that the hysteresis is related to the chemical and structural heterogeneity of the surface [95-98]. However, there is almost no unique relation between the values of contact angle and contact angle hysteresis. In other words, it is normal to have surfaces with a similar contact angle value but with quite different hysteresis numbers. On the other hand, low hysteresis usually happens when the sessile contact angles are large, i.e. in superhydrophobic materials. Hysteresis is a very important property and should be considered precisely when the ease of liquid movement on the surface is concerned.

2.2.5 Passivation

The surface energy of solids is a surface property, which means it is determined by few outermost atomic layers. Therefore, the energy of a particular surface can be increased or decreased by covering the surface with an appropriate thin film, usually as thin as a few layers of molecules. When the final energy is lower than original value, the process is called a passivation.

Some organic molecules have a polar group at one end (namely head) and a non-polar long saturated hydrocarbon chain on the other end (tail). Since the hydrocarbon chain has all its valence requirements satisfied by carbon–carbon or carbon–hydrogen bonds, it is fairly inert to the polar interactions with polar liquids like water. The polar head can be absorbed to other polar molecules or to high energy solid surfaces and make bonds. In ideal case, the entire solid surface can absorb enough number of these organic molecules and be covered perfectly with only one molecular layer. This ordered arrangement of molecules is called self-assembled monolayer, or SAM. Presence of such a molecular layer can result in

considerably lower surface energy. SAMs have been subject of intensive studies and many organic acids with saturated long chains or alkylsilanes are found to form SAMs [99-101] .

Fluorine, the first element of seventh group in periodic table, is known to be effective for lowering the surface energy. A variety of fluorinated materials have been prepared with excellent resistances against water, oil and organic solvents, for example polytetrafluoro-ethylene (PTFE) with more familiar name, Teflon. According to the functional groups, the surface energy reduces in this order: $-CH_2 > -CH_3 > -CF_2 > -CF_2H > -CF_3$ [102]. The least surface energy relates to the hexagonal arrangements of closely packed $-CF_3$ groups [103]. Some types of fluorocarbon SAMs showed promising to reduce ice adhesion compared to bare aluminum surfaces [104,105]. This is also compatible with theoretical predictions [28]

.

2.2.6 Effect of Roughness, Superhydrophobicity

The passivation is not the only parameter which can affect the wettability of materials, the surface morphology is equally important. Usually, passivated smooth solids show the maximum achievable contact angles ~ 120°, quite far from the maximum value of 180° [106]. On the other hand, there are some plants in nature, such as *Nelumbo nucifera druce,* which exhibit very high water contact angles (CA) and very low contact angle hysteresis and this property is usually known as the Lotus Effect [29], as shown in figure 2.6a. This phenomenon is not restricted to plants. Similar properties are identified in some animals and insects. It is worth mentioning that lotus leaves are covered by a paraffinic wax containing predominantly $-CH_2-$ groups [29]. In lotus leaf surfaces, lower energy of $-CH_3$

groups or fluorocarbons are not present and the surface energy is not extremely low [107]. The key feature of these natural surfaces, which makes them so water-repellent, is the presence of a specific surface morphology. In figure 2.7 some scanning electron microscopy (SEM) images of these tissues are shown [108].

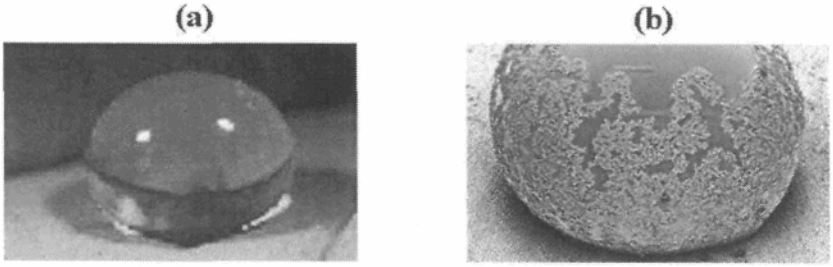

Figure 2.6: (a) water drop on lotus leaf with contact angle more than 150°, (b) self-cleaning property of lotus leaves

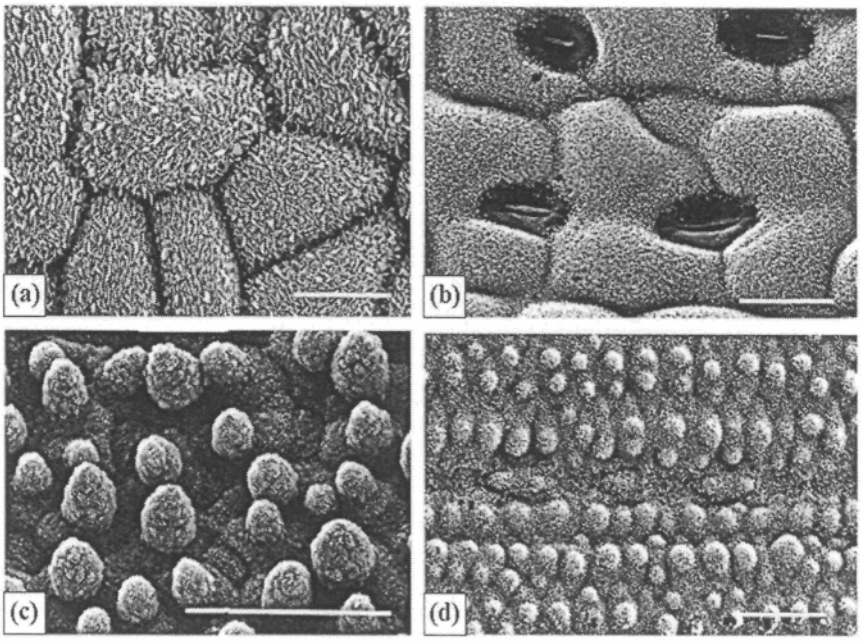

Figure 2.7: SEM images of superhydrophobic leaf surfaces. Water-repellent leaf surfaces of (a) hypericum aegypticum, scale bar=20μm; (b) mMarsilea mutica, bar=20μm (c) nelumbo nucifera, bar=50μm. (d) sinarundinaria nitida, bar=20μm.

When the sessile contact angles are over 150°, the surface is usually termed as superhydrophobic [26]. Natural superhydrophobic materials usually have a very low hysteresis which appears in simplicity of rolling the water drops off the surface. The rolling droplets absorb the dust and debris and carry them out of the surface, as depicted in figure 2.6b. This is called self-cleaning.

On a rough solid surface, the predicted contact angle by Young's equation, θ_0, may be not close to the measured contact angle. When the surface is rough, two distinct events may happen: liquid can completely fill up the grooves (figure 2.8a) or some air bubbles entrap underneath the liquid (figure 2.8b). The former situation is the "homogeneous wetting regime", while the latter is the "heterogeneous wetting regime" [109].

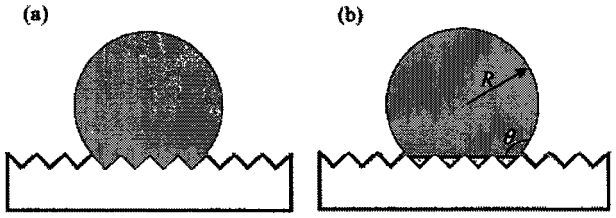

Figure 2.8: Liquid drop on rough hydrophobic surface: (a) homogenous (Wenzel) and (b) heterogeneous (Cassie-Baxter) regimes

Wenzel [110] introduced an equation defining a relation between the actual contact angle on rough surface in homogenous wetting regime and the Young's contact angle as follows:

$$\cos\theta^W = r\cos\theta_0 \qquad \textbf{(Eq. 2.2)}$$

where r is the roughness factor defined as the ratio of the actual area of a rough surface to the projected area. If θ_0 is less than 90°, θ^W is smaller than θ_0 and reduces as r increases.

On the other hand, when θ_0 is greater than 90°, θ^W is greater than θ_0 and increases by increment of r. Figure 2.9 shows the effect of roughness in Wenzel model for a range of r and θ_0. Therefore, based on Wenzel model it is impossible to have the contact angles in the shaded areas in figure 2.9a. Another limitation of Wenzel model is no prediction for θ^W in the cases of $r\cos\theta_0 > 1$.

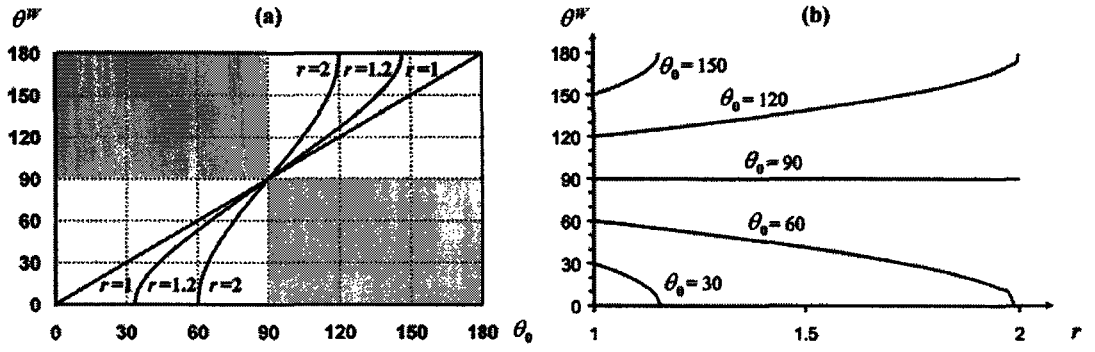

Figure 2.9: (a) Contact angles predicted by Wenzel's model for roughness factors of 1, 1.2, and 2 [98]; (b) contact angle for rough surface as a function of roughness factor in Wenzel's model [111]

All surfaces have some degree of chemical heterogeneity. A heterogeneous solid surface has domains with different surface free energies. Cassie and Baxter [112] developed another model by considering the interface composed of two types of domains: fraction f_1 with contact angle of θ_1 and fraction f_2 with contact angle of θ_2 where $f_1 + f_2 = 1$. The predicted contact angle, θ^{CB}, can be calculated as:

$$\cos\theta^{CB} = f_1\cos\theta_1 + f_2\cos\theta_2 \qquad \textbf{(Eq. 2.3)}$$

It states that the cosine of the contact angle on a heterogeneous surface is the weighted average of the cosines of the contact angles on the various fractions. In the case of rough heterogeneous surfaces, it is possible to have some amount of air entrapped beneath the liquid drop. If fraction f_2 represents the solid-air interface and considering that liquid drops in air have spherical shape, or equally $\theta_2 = 180^\circ$, we have:

$$\cos\theta^{CB} = f_1 \cos\theta_1 + f_2 \cos\theta_2 = f_1 \cos\theta_1 + (1 - f_1)\cos 180^\circ = f_1 \cos\theta_1 + f_1 - 1$$

where f_1 is solid-liquid fraction. Replacing f_1 with f and θ_1 with Young's contact angle θ_0 lead to:

$$\cos\theta^{CB} = f\cos\theta_0 + f - 1 = f(\cos\theta_0 + 1) - 1 \qquad \textbf{(Eq. 2.4)}$$

known as modified Cassie-Baxter model [113,114]. Having this model, it is possible to obtain $\theta^{CB} > 90^\circ$ even if $\theta_0 < 90^\circ$, provided that f is very small. Figure 2.10 depicts the effect of roughness in modified Cassie-Baxter model for a range of θ_0 and some f values.

Another form of Cassie-Baxter model is also suggested as:

$$\cos\theta^{CB} = r_f f \cos\theta_0 + f - 1 \qquad \textbf{(Eq. 2.5)}$$

where r_f is roughness ratio of wet area of solid [109]. This equation gives more precise contact angle because of considering the effect of the curvatures in wet area. It is known that both the Wenzel and Cassie-Baxter models can be correct only if the drop size is sufficiently large compared with typical surface roughness [115,116].

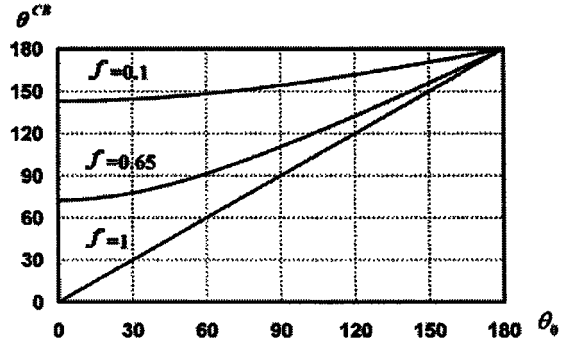

Figure 2.10: Contact angles predicted by the modified Cassie-Baxter model for solid-liquid fractions of 0.1, 0.65, and 1 [98].

Homogeneous and heterogeneous wetting regimes are commonly referred to as Wenzel and Cassie-Baxter wetting regimes. Many researchers tried to find out which of the wetting regimes is preferred for drops in equilibrium state on certain surfaces [117,118]. It is found that transitions are probable between wetting regimes in superhydrophobicity and there is a relationship between the solid surface topography and the transition between the homogeneous and heterogeneous wetting regimes [118].

2.2.7 Artificial Superhydrophobic Surfaces

In many areas of technology it is required to control the wettability of surfaces. Self-cleaning property is desirable for car windshields, aircraft, solar energy cells, etc. A general classification of methods to prepare superhydrophobic surfaces into two broad groups is given in [107]. The former group includes the ways of roughening the low-surface-energy materials and latter one has the two-step methods; making a rough surface and then passivating it. A brief of each category is as follows:

Roughening a low surface energy material:

- Fluorocarbons: Fluorinated polymers have extremely low surface energies. Roughening these polymers can lead to superhydrophobicity. For example, one can name achievement of 165° water contact angle on PTFE by Zhang et al. [119], 161° on polymer-embeded PTFE by Menini et al [120], 159° on poly[bis(2,2,2-trifluoroethoxy)phosphazene] by Singh et al. [121], etc. Silicones: Polydimethylsiloxane (PDMS) is a well-known material with low surface energy that can readily be converted into superhydrophobic surfaces. Some works on PDMS are reported with water contact angles up to 175° by Khorasani et al. [122], 160° by Jin et al. [123], 150° by Sun et al. [124], etc.
- Organic materials: Some researchers followed the approach of nature to make superhydrophobic surfaces made from organic materials. One can refer to the works reporting 173° on polyethylene by Lu et al. [125], 162° on polystyrene/dimethyl-formamide composite byJiang et al. [126], 150° on polyalkylpyrrole byYan et al. [127], etc.
- Inorganic materials: Some inorganic materials also can lead into superhydrophobic surfaces. Some examples are obtained on ZnO (173°) by Saleema et al [128], (151°) by Yang et al. [129] and on TiO_2 (160°) by Feng et al. [130].

Making a rough substrate and modifying it with low surface energy materials

- Etching and lithography: Etching is a straightforward and effective way to make rough surfaces. Different etching methods are tried to make roughness, such as plasma etching [131], laser etching [132] and chemical etching [133]. Lithography

(e.g. photolithography, electron beam lithography, X-ray lithography, soft lithography, nanosphere lithography and so on) is a well-established technique for creating large area periodic micro-/nanopatterns. Some examples of using these methods for a systematic study of superhydrophobicity are as follows: Abdelsalam et al. studied the effect of pore size and shape in controlling wetting of gold and showed that the apparent contact angle was independent of the pore diameter over the range 400-800 nm [134], Martines et al. fabricated ordered arrays of nanopillars by using electron beam lithography and found that a forest of hydrophilic/hydrophobic slender pillars was an very effective water-repellent configuration [135], etc.

- Sol–gel processing: Sol–gel processes can be used to fabricate superhydrophobic surfaces from different materials. For instance, Shirtcliffe et al. [136] prepared porous sol–gel foams from organotriethoxysilanes which exhibited superhydrophobicity at certain temperatures, or Hikita et al. [137] used colloidal silica particles and fluoroalkylsilane and obtained a contact angle of 150°.
- Layer-by-layer (LBL) and colloidal assembly: LBL self-assembly is a rich process to make thin film coatings with molecular level control over film thickness. For recent use of LBL process to make rough surfaces, one can refer to works of Shi et al. [138] on gold aggregates or Zhao et al. [139] on silver films among many others.
- Electrochemical and chemical bath deposition (CBD): Electrochemical deposition is extensively reported to prepare superhydrophobic surfaces. For instance, Zhang et al. [140] fabricated dendritic gold clusters, which was formed by electrochemical

deposition onto indium tin oxide or Shirtcliffe et al. [26] prepared a double-roughened copper surface. As an example of CBD, Hosono et al. [141] used this technique to fabricate a nanopin film of brucite-type cobalt hydroxide.

- Other methods: There are also some other methods for making superhydrophobic surfaces, such as electrospinning [121] and chemical or physical vapour deposition (CVD or PVD) [142].

Several superhydrophobic materials have been produced using a range of chemical and physical methods [143-145]. Some of these coatings show promises of hindering snow accumulation too [146,147]. Figure 2.11 shows two type of the ordered surface morphologies prepared by photolithography method on silicon [95] and polystyrene [148] which are used for superhydrophobicity investigations.

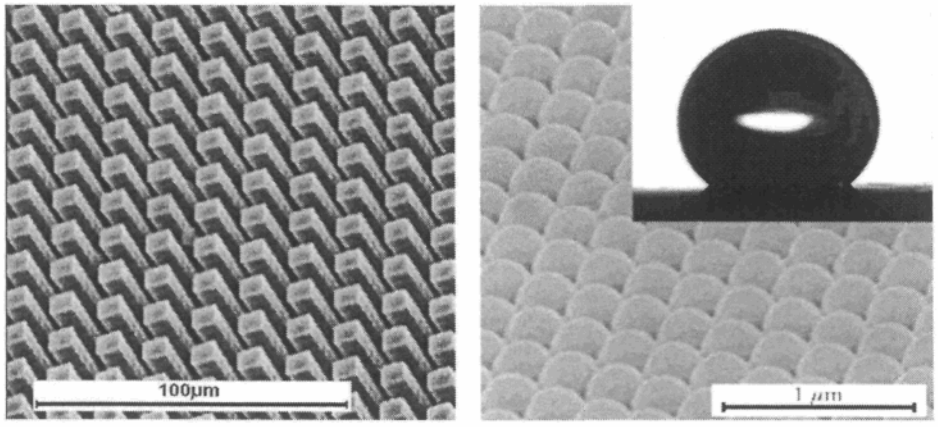

Figure 2.11 : Ordered nanostructures of silicon (left) and polystyrene (right) for superhydrophobicity studies [95,148].

Although the ordered micro/nano structures are extremely valuable to study the details of water droplet behaviour on superhydrophobic surfaces, the regularity of tiny arrangements is not necessary to have high degrees of water repellency; not-ordered rough surfaces can exhibit very similar properties. Figure 2.12 depicts two examples of not-ordered alkylketene dimer [143] and copper [26] superhydrophobic surfaces.

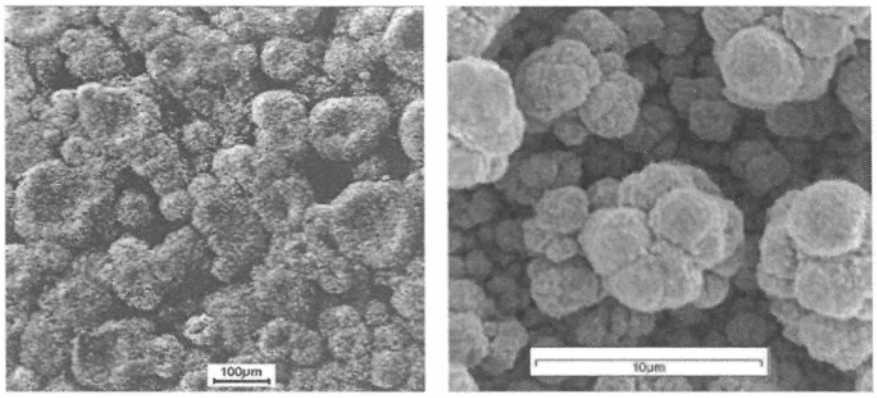

Figure 2.12 : SEM images of alkylketene dimmer (left) and copper (right) surfaces.

Ideally, a coating layer must be able to: cover the entire surface to give a uniform defect-free layer; bond strongly to the surface; be durable and demonstrate stable performance, and be easy to apply on different substrate shapes, among other criteria. Among the methods mentioned earlier, making the required roughness by spreading the previously prepared nanoparticles is a flexible technique which can be used to make wide range of surfaces in a controlled way. The related aspects of nanoparticles are discussed with more details in the next section.

2.3 Nanoparticles and Their Morphology

2.3.1 Nanoparticles

Nanomaterials, with at least one of three dimensions in the range of 1 to 1000 nm, have attracted ever-growing interest due to their fascinating properties. Nanoparticles are solid materials with all the dimensions varying in nanometre scale [31,32]. The properties of nanomaterials lie between those of molecules and bulk structures, strongly dependent on the size, shape and structure [149]. In nanometre range, which is typical motion scale of the electron that determines the properties of material, the situation is unique. Nanosize-effects are evident in specific optical, electrical, magnetic and catalytic behaviours quite different from those of the bulk material. In metals, high surface/volume ratio leads to dominant surface effects and nano-particles gain new properties. In noble metals, which have low electrical resistance, the collective oscillations of electrons can be quite strong in the frequency range of ultraviolet and visible light. This appears in special absorption/radiation spectra of noble nanoparticles, for example nanoparticles of gold or silver.

Over the last two decades there have been dramatic advancements in the study of nanomaterials, which have wide applications in electronics [150,151], catalysis [152], biosensors [153], antimicrobial [154], nonlinear optics [155], magnetic storage [156], etc., and many other applications are expected to benefit of nanomaterials in coming years.

2.3.2 Preparation of Nanoparticles

The research on the properties of the nanomaterials largely rests on the development of new preparation methods. In general, the various methods of producing nanoparticles can be classified in two broad categories. Figure 2.13 depicts these two categories.

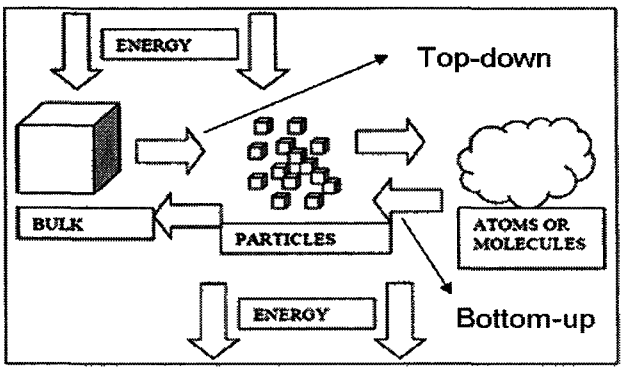

Figure 2.13: Top-down and bottom-up approaches to achieve nanoparticles.

- The "top-down" or "phase-breakdown" procedures are based on breaking down the bulk materials into smaller particles with dimensions in the range of micrometers or nanometres.
- In the "bottom-up" or "phase build-up" approaches, the nanoparticles are synthesized from atoms or molecules as building blocks by chemical reactions [157].

For the case of metals, the phase-breakdown method is based on applying energy to the bulk material in order to separate the pieces of metal, for example by mechanical milling or by fast cooling of molten droplets of metal. These procedures can not provide uniform or monodispersed particles. The focused ion beam (FIB) is another tool which can cut away (mill) pieces with dimensions of microns from a target material and it is possible to operate

directly on the nanoparticles [158]. Milling is achieved by accelerating focused ions, such as gallium iones, to a specific target, which etches off exposed surface of material, ejecting tiny particles. Although this method is very precise, it is expensive and hard to use.

In the bottom-up or "phase build-up" methods, the metallic particles are prepared directly from the metal atoms. This process can be performed either in gas or liquid phase, by controlling the process in liquid medium is easier [157]. The liquid medium synthesis is easier to monitor and control, needs less expensive facilities and materials, and is more appropriate for laboratory scale investigations. Herein, the bottom-up approach is used throughout this text.

Nanomaterials also have different shapes and morphologies. Figure 2.14 depicts some images of silver nanostructures reported in the literature: nanocubes [159], triangular nanoplates, a cross section of nanowires with pentagonal shape and nearly spherical nanoparticles [160].

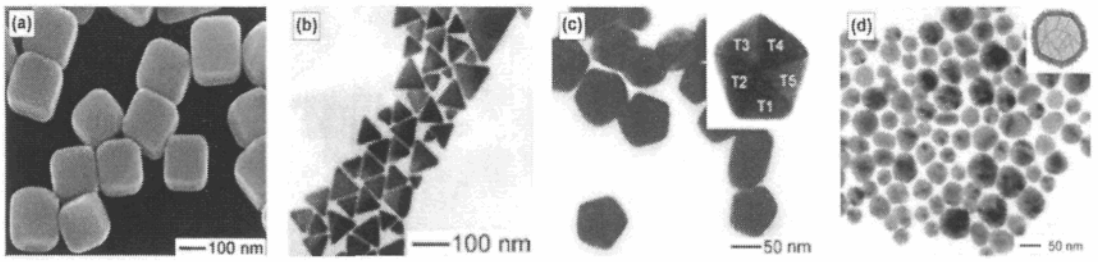

Figure 2.14: Nanosize silver in different shapes: (a) SEM image of nanocubes, TEM image of triangular nanoplates (b), pentagonal cross section of nanowires (c) and nearly spherical nanoparticles.

The size, shape and structure of nanomaterials are dependent to great extent on the selected preparation method and its parameters such as reagent concentrations, temperature, time, etc. Figure 2.15 shows the drastic change in the morphology by doubling the concentration of one of the reagent in the reaction [161].

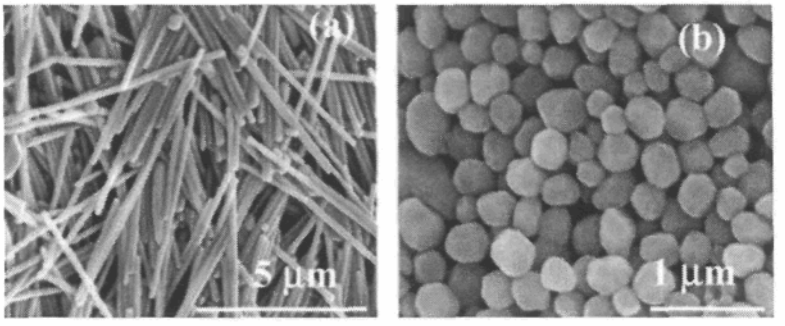

Figure 2.15 : SEM images of silver nanorods (a) and nanoparticles (b) [161]

2.3.2 Nanoparticle-based Coatings

As described previously, some degree of surface roughness is needed to achieve superhydrophobicity. It is common to use the nanoparticles not only in colloidal solutions but also in solid phase. Spreading the nanoparticles onto a solid surface can provide new surface morphologies with nanosize roughness. Different approaches have been reported to bring and bind the nanoparticles onto the surfaces to make them rough. For instance, silica particles have been coated on latex by sol-gel processing [162] or on glass by dip-coating [163]. Another example is TiO_2 nanoparticles by spray coating on cement [164] or glass [165]. There are very few articles about this application of metallic nanoparticles, such as [166,167], but apparently there is rarely any report of making the metallic nanoparticles and

bringing them onto the surface toward achieving superhydrophobicity. Figure 2.16 shows the rough surfaces with high degree of superhydrophobicity prepared by silica [162] and titanium dioxide [164] nanoparticles. This is the intended approach in this research.

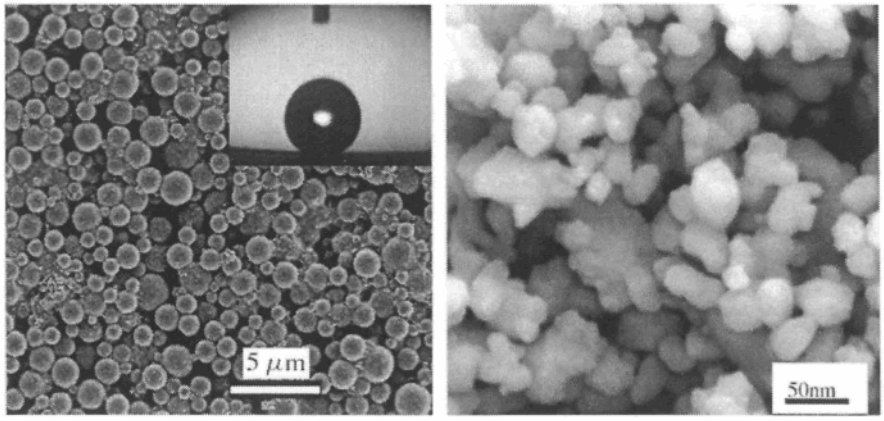

Figure 2.16 : The surface morphology after coating with silica particles (left) or TiO_2 (right) to achieve superhydrophobic surfaces.

CHAPTER 3

BACKGROUND

In this chapter, the detailed synthesis of metallic nanoparticles and preparation of thin nanostructured films are described. Also, the used characterization techniques are explained.

3.1 Preparation of Nanoparticles

Three methods were used to obtain different sizes of nearly-spherical silver particles, labelled as type 1 to type 3, respectively. Also, two methods were applied to achieve copper nanoparticles, types 1 and 2. These labels are used throughout this text. The following sections include the details of nanoparticles preparation procedures.

3.1.1 Materials

In all of the subsequent experiments, anhydrate silver nitrate ($AgNO_3$, 99.9%, Alfa Aesar) was used as a precursor of silver and pentahydrate copper sulphate ($CuSO_4$, $5HO_2$, 99.9%, Fluka) was applied as a copper precursor. Ethylene glycol (EG, 98.5%, EMD), polyvinylpyrrolidone (PVP, Mw = 40 000, Alfa Aesar), and L-ascorbic acid (99.8%, J.T.Baker) were used as received. De-ionized water with a resistively of 18 MΩ-cm was prepared using a four-step filtration system (Millipore). Acetone (99.5%, EMD) and methanol (99.8%, MAT) were used without further purification.

3.1.2 Silver Particles Type 1, Synthesis in Hot Alcohol Medium

Type 1 of Ag nanoparticles was prepared in an alcohol medium following the approach described in [159]. Briefly, solutions of $AgNO_3$ (0.25 M) and PVP (0.375 M in repeating

unit) were prepared both in EG. As shown in figure 3.1, a 50mL EG was heated to 160°C for 1 h in a round-bottom three-neck flask under vigorous stirring (500rpm). Here, EG was used as a solvent as well as a reducing agent. The $AgNO_3$ and PVP solutions were injected into the flask simultaneously, with an average rate of 3 mL/min. A transparent red color appeared immediately but turned to turbid yellow. The liquid was sampled periodically for UV-vis investigation. The reaction mixture was stirred at 160°C for 60 min, and then removed from heat source to cool down naturally, under stirring for ~3 h, prior to centrifugation. More information is given in appendix D.

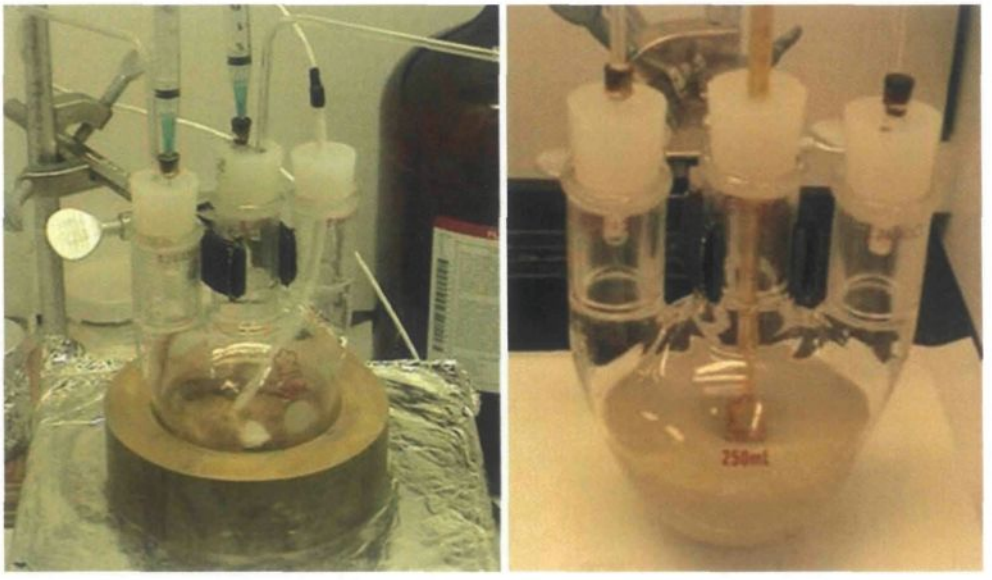

Figure 3.1: Experimental setup for preparation of nanoparticles.

3.1.3 Silver Particles Type 2, Synthesis in Basic Medium

Type 2 of Ag nanoparticles was obtained by the following procedure: A solution of $AgNO_3$ in deionized water (0.25M) was prepared and kept in a dark bottle to protect from

light-induced reduction. 1.5 mL of this solution and 3 mL of PVP in EG (0.375M) were dissolved in 50 mL of EG while stirring at 500 rpm at room temperature. 5 mL of KOH (75mM) were added drop by drop to the above solution while stirring continuously. A dark green color appeared immediately. After 10 min, the reaction was terminated by adding four-fold volume of deionized water.

3.1.4 Silver Particles Type 3, Synthesis with Ascorbic Acid

Type 3 of Ag nanoparticles was prepared in aqueous/alcohol medium. A mixture of 75 mL deionized water and 25 mL EG was prepared in a flat-bottom beaker under vigorous stirring at room temperature. 3 mL of $AgNO_3$ (0.25M) and 10 mL of PVP (0.375M) both in deionized water were added to the mixture. 6 mL of L-ascorbic acid in water (0.25 M) were added drop-wise while stirring continuously. The solution turned to pale yellow color slowly. After 10min, the reaction was terminated by adding four-fold volume of water. The particles were collected immediately afterwards by centrifugation.

3.1.5 Copper Particles Type 1, Synthesis with Ascorbic Acid

Type 1 of Cu nanoparticles was achieved as follows: A mixture of 100 mL of EG and 3 mL of PVP (dissolved in EG, 0.375 M) were poured in a round-bottom three-neck flask (similar to the setup of figure 3.1) and then heated to 140°C, under vigorous stirring for 30 min. Then, 3 mL of $CuSO_4$ (dissolved in EG, 0.25 M) and 3 mL of L-ascorbic acid (dissolved in water, 0.25 M) were injected into the flask with average rate of 0.5 mL/min. Immediately after the injection, the mixture turned red, indicating the presence of copper

clusters. On adding more solution, the mixture became dark-red in color. Presence of water in the ascorbic acid solution led to high amount of water vapour bubbles. After one hour of heating at 140°C, the flask was removed from heat source. Adding a small amount of ascorbic acid solution into the mixture prevented the Cu particles from oxidation. After cooling to room temperature, the colloid was diluted and centrifuged.

3.1.6 Copper Particles Type 2, Synthesis with Two-step Process

And type 2 of Cu nanoparticles was prepared as below: A solution of 50 mL of EG and 50 mL of deionized water was taken in a three-neck flask, with stirring and purging with N_2 for 15 min to remove the dissolved oxygen. Then, 10 mL of $CuSO_4$ (25mM) and 6 mL of PVP (0.375M) were added to the solution while stirring continuously. Afterwards, 4 mL of ice-cold $NaBH_4$ (25mM) solution were injected into the flask drop by drop. Appearance of a dark-yellow color indicated the formation of metal particles. The liquid was sampled for tracking the nanoparticle growth by UV-vis investigation. Then 3 mL of ascorbic acid (0.25M) were added within one minute. The color became dark-red. Purging was continued until 10 min after injection of acid. The particles were separated from the solution by centrifugation.

3.1.7 Centrifugation

A laboratory centrifuge (Drucker, 614V) was used to concentrate the colloids of nanoparticles. In all cases, the applied centrifuge speed and duration were kept equal to 3500 rpm and 45 min respectively. The solvents for different reactions are summarized in

table 3.1. Adding acetone decreased the viscosity and facilitated the separation of particles. It also helped dissolve the PVP covering the particles which could result in unwanted effects afterwards. Presence of methanol helped have more uniform solution, especially when the amount of EG was high, and inhibited very fast precipitation of particles on the glass tube walls. The number of centrifugation cycles was selected based on the initial molar ratio of PVP:Metal in each reaction. With higher PVP, it was necessary to repeat the process to ensure the removal of PVP from the particles. After centrifugation, the particles were dispersed ultrasonically in a mixture of methanol and EG with ratio of 3:1.

Table 3.1: The centrifugation parameters for different reactions.

Particle	Reaction Solvent	Centrifugation solvent	Centrifugation
Silver, type 1	EG	Colloid:Acetone:Methanol = 2:11:2	2 times
Silver, type 2	EG	Colloid:Acetone:Methanol = 2:11:2	3 times
Silver, type 3	EG:H_2O = 94:25	Colloid:Acetone:Methanol = 3:10:2	3 times
Copper, type 1	EG	Colloid:Acetone:Methanol = 2:11:2	3 times
Copper, type 1	EG:H_2O = 1:1	Colloid:Acetone:Methanol = 5:8:2	3 times

3.3 Coating Process

3.3.1 Materials

Methanol (99.8%, MAT), hexane (98.5%), acetone (99.5%), iso-propanol (99.8%), ethylene glycol (98%) (all from EMD) and sulphuric acid (98%, SIGMA-ALDRICH) were used without further purification. De-ionized water with a resistively of 18 MΩ-cm was used. Different materials were used as substrates. Aluminum and copper were principal

substrates with dimensions of 1" × 1" for wettability characterizations and 2" × 1(¼)" for icing tests. To connect a sample to an icing test beam, two 3mm-diameter holes were drilled in one side of the sample. The aluminum substrates used here were cut or punched from industrial rolled sheets of aluminum alloy (AA6061-T6) with 1/16" thickness. The alloy composition is: Al 97.9 wt.%, Mg 1.0 wt.%, Si 0.60 wt.%, Cu 0.28 wt.%, Cr 0.20 wt.%. The copper samples were, cut from 1/8" thick industrial copper strips provided by Metal Solutions Company. Silicon substrates with approximate size of (½)" × (½)" were used for FTIR measurements and study of nanoparticle morphology with AFM and SEM, if applicable. Glass slides (VWR) were cut into 1" × 1" pieces and used for UV-visible study of nanoparticle-based coatings.

3.3.2 Coating

Copper substrates were washed in a soap solution and then with acetone to remove dirt, oil and organic materials. After that they were placed in a sulfuric acid solution (10% v/v) for 10s, to get rid of oxide layer, followed by washing several times in deionized water and drying in nitrogen flow. Aluminum substrates were also washed with a soap solution and then with water. The glass substrates were cleaned ultrasonically for 15 minutes in a KOH solution (10mM), then three times with water. Silicon samples were washed ultrasonically with acetone, iso-propanol and water consequently, each for 15min. All the substrates were dried at 70°C in an oven in air atmosphere.

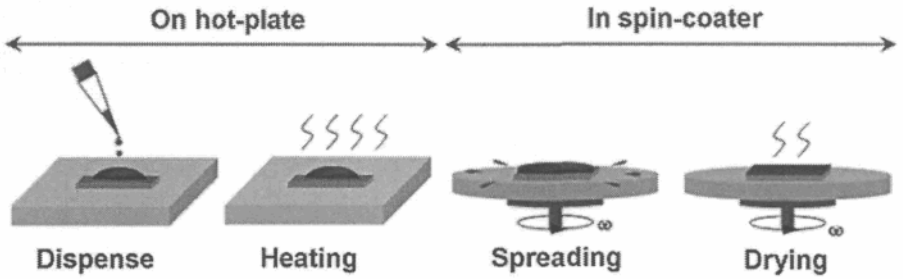

Figure 3.2: Coating procedure.

Figure 3.2 shows the procedure of bringing the nanoparticles from colloidal solution to the surface of substrates. A desirable amount of nanoparticles was added to a tube containing a mixture of MeOH/EG with ratio of 20:1 and the tube was sonicated for 5 min to have a uniform colloid. Each substrate was taken out of the oven and placed on a hot-plate at room temperature. The sample was covered with a thin layer of MeOH which could wet all the substrate types used. After 1 min, 0.5 mL of colloid were placed onto the surface. The presence of MeOH layer helped provide a uniform liquid layer which covered the entire sample surface. After 5 min, the hot-plate was set at 80°C with rising rate of 400°C/h. The sample was heated for a desirable period of time at 80°C, then removed from the hot-plate and transferred to a spin-coater. After spinning with specific parameters, the sample was dried in the oven at 70°C or annealed in a tube-furnace, and kept in the oven until characterization step.

3.4 Passivation Process

3.4.1 Materials

One set of smooth silver films were grown on silicon wafer by a thermal evaporation technique with 0.2 nm/sec deposition rate, up to a thickness of 40 nm. Lauric acid (95%, J.T.Baker), palmitic acid (99%, CALBOCHEM) and stearic acid (99%, Alfa Aesar) were used as-received. Commercial 1/8" thick PTFE sheets were utilized as targets in rf-sputtering process. Zonyl 8740, (a perfluroalkyl methacrylic copolymer from Dupont) was used without further purification.

3.4.2 Passivation

Three different methods were followed for passivation purpose. In the first approach, the samples were placed in a solution of 50 mL acetone or hexane containing 2 mM carboxylic acids. After 30 min, the sample was removed from the solution, dried in N_2 flow and then cured in an oven at 80°C overnight, i.e. more than 12h.

In second passivation method, thin layers of polytetrafluoroethylene (PTFE) were deposited by radio frequency magnetron sputtering of a PTFE target using argon plasma in an inductively-coupled plasma reactor (Plasmionique HICP-600SB). The sputtering process started after 2 h evacuation at a base pressure in the chamber equal to 3×10^{-6} Torr. The Ar pressure of 20 mTorr and injected power of 50W were maintained in the chamber during coating process. The distance between the target and samples was 30 cm and the sputtering period was approximately 17 min.

In the third approach, the samples were immersed in a 30 mL aqueous solution containing 5 wt.% of Zonyl 8740. After 1 h, the samples were removed from the solution, dried in N_2 flow and then kept at 80°C in the oven.

3.5 Characterization Methods

3.5.1 Atomic Force Microscopy

When the surface of coated samples was not very rough, an atomic force microscope (Digital Nanoscope IIIa) was used to characterize the morphologies. After removing the loose particles and dust, the samples were kept in the AFM for one hour prior to performing a measurement. The imaging was carried out in tapping mode, with a silicon-nitride probe (Nanosensors™, PPP-NCH), and at room temperature under normal air pressure. This type of AFM probe has a typical tip radius of less than 7 nm, with high mechanical Q-factor for high sensitivity and fast scanning ability. AFM images, and related software (v613R1sr1) were used to obtain some useful information such as surface morphology, particle coverage and particle size distribution.

To study a highly planar silver surface, a smooth thin film of silver was prepared on silicon substrate (100). Smooth silver films were grown on silicon wafer by a thermal evaporation technique with 0.2 nm/sec deposition rate up to a thickness of 40 nm.

3.5.2 Scanning Electron Microscopy

The morphologies of metallic nanoparticles and coated surfaces were observed using a LEO Gemini field emission scanning electron microscope. Gemini field emission electron

gun has many advantages, such as high beam brightness and low energy spread which gives better images in high magnifications. Before each measurement, a very thin film of platinum was coated on the sample by thermal evaporation. This was done to minimize charge build-up during the scanning. In most cases, a 20kV beam was used during the scanning, with magnifications up to x100k.

3.5.3 Optical Profilometry

Some topographical surface profiles were achieved using an optical profilometer, Wyko NT 1100 (Veeco), suitable for large-region and irregular samples. The vertical resolution is ~3 nm in a range of up to 1mm. The inspected surface areas were 0.9 mm wide and 1.2 mm long.

3.5.4 X-ray Diffraction

X-ray diffraction (XRD) is a non-destructive method capable of revealing the details of chemical composition and crystallographic structure of solid materials. XRD pattern was obtained using a X-ray diffractometer (Bruker D8 Advance) with Cu K_α radiation ($\lambda \cong 0.154$ nm) in order to study the elements on a copper sample coated with silver nanoparticles.

3.5.5 Absorption Measurements

UV-visible spectrometry:

Nanometer scale conductive entities can effectively absorb the energy of passing electromagnetic wave and this property can be used to identify the metallic nanoparticles in

a non-absorbent medium (see appendix C). Metallic nanoparticles in this research have characteristic plasmon resonance bands in the ultra-violet and visible (UV-Vis) region of electromagnetic spectrum. The applied system to track these particles was a spectrometer (8453, Agilent) capable of detecting the absorbance of light passing through the transparent samples.

Having the particles in colloids, a plastic or quartz cuvette filled with methanol was used as background. Then a colloid was added drop by drop until a clear, noise-free spectrum was achieved without having saturation. The UV-vis spectra were recorded two times and their average was considered in next studies. A similar method was followed for thin films coated on glass substrate, with a clean glass slide used as a background.

Fourier transform infrared spectrometry:

After passivation, the presence of organic materials on the silicon substrates was studied using Fourier transform infrared spectroscopy (FTIR, Spectrum One, PerkinElmer). Ultrasonically cleaned silicon substrate was used for background subtraction during FTIR measurements and the number of scans used for each sample was kept constant at 20. No N_2 purging was done, but it was always considered to have similar test conditions.

3.5.6 Contact Angle Measurement at Room Temperature

The system used for contact angle measurements is a DSA100 drop shape analyzer system (KRÜSS Co.), shown in figure 3.3. It has an automatic injection mechanism with several fully-controllable syringes. There is a light source to illuminate the sample surface

and a CCD camera connected to a computer where the drop shape can be recorded and analyzed. There are two knobs for zoom and focus functions. Also the goniometer stage, the place on which sample sits, can be moved manually by another knob. Using the related software (DSA1 v1.9), one can select any of the syringes and control its position and injection rate. It can also control the light intensity and functions of the camera. Another important task of the software is to calculate the contact angles by curve fitting methods [168].

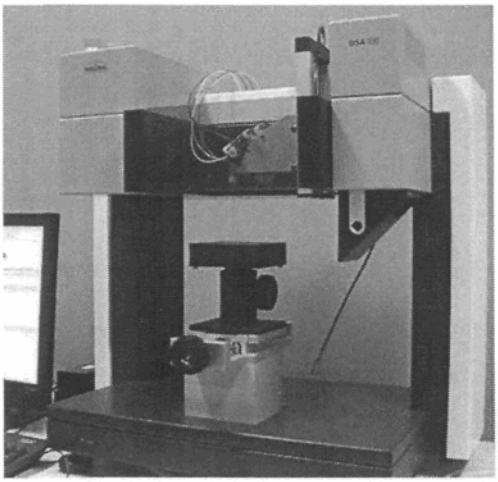

Figure 3.3: DSA100 drop shape analyzer system for contact angle measurements.

To measure a static contact angle, the desired amount of liquid was selected by the software (usually 6μL) and a droplet is made suspending from the syringe needle. The sample was placed on the completely levelled goniometer stage of drop shape analyzer. Then the needle was brought near the sample so that the drop was in contact with sample surface. A very slight impact to the needle released the drop. For the very slippery samples, these steps should be done carefully otherwise the drop could roll off easily and go off the

sample. It was essential to wait for 10s prior to measurement to be sure that the droplet is stabilized. Also the image should be focused. More precise results were achieved in a dark room.

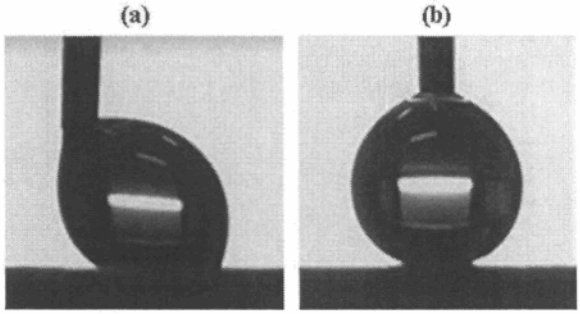

Figure 3.4: Measuring the advancing and receding contact angles on a sample with (a) a high hysteresis and (b) a low hysteresis.

A commonly used experimental approach [169] was followed to measure the contact angle hystereses. A water drop of volume ~6 μL was injected and brought into contact with a sample surface while suspending from the needle. The water drop was kept in contact with the sample surface with stationary needle in it. Then the advancing and receding contact angles were measured while moving the stage and the sample in one direction by turning the positioning knob very slowly. This method lets us to measure these two angles and to deduce directly the contact angle hysteresis simultaneously (figure 3.4).

3.5.7 Contact Angle Measurement at Lower Temperatures

The above mentioned system has a set of additional parts for measuring the contact angles in desired temperature. A specially designed chamber can replace the simple goniometer stage, shown in figure 3.5a and 3.5b. It has sealed walls and windows, and a

thermoelectric heating/cooling element (Peltier) at the bottom. Using a fast and high-precision controller, (TC40, figure 3.5c and 3.5d), it is possible to adjust the temperature of Peltier element over a wide temperature range of –30°C to +160°C within ±0.2°C.

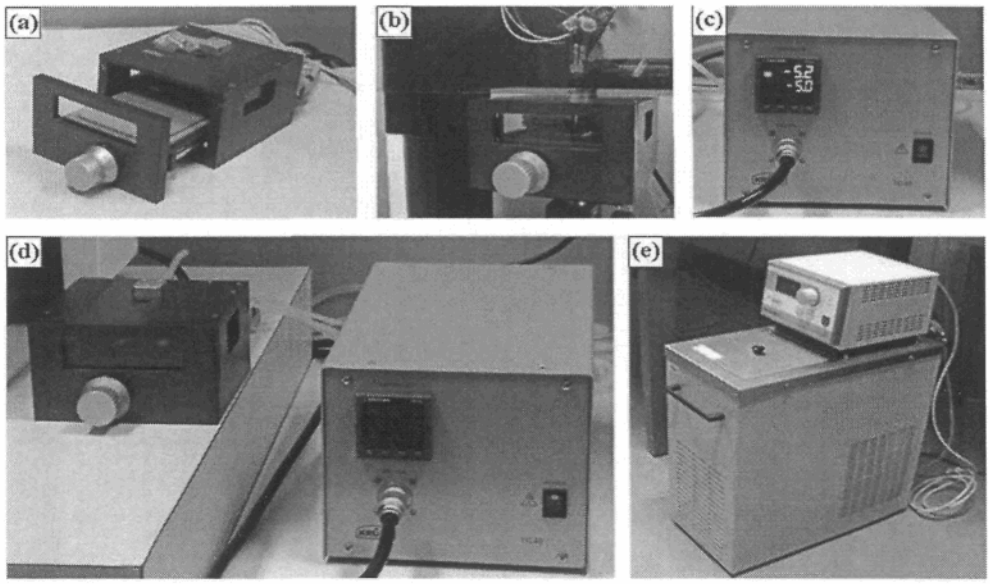

Figure 3.5: Temperature-controlled chamber, TC40 controller and liquid-circulating thermostat.

A powerful liquid-circulating thermostat unit (figure 3.5e) brings the temperature near the desired value and is responsible to remove excess heat from Peltier element. The Peltier chamber has a built-in high-precision positioning knob which helps have a reproducible positioning of the sample and a minimum opening for the needle

The experiment was performed as follows: a sample was placed inside the Peltier chamber at room temperature. Then a water drop of ~6 μL was placed on the sample and the needle was removed and the process of contact angle measurement started. The set-point of TC40 was changed to -5°C and the measurement was continued. After ~3 min the

droplet was frozen completely. Then the set point was retuned to +5°C and the same steps were exactly repeated for the melted droplet.

3.5.8 Ice Adhesion Test

According to section 2.1.4 applying a differential adhesion measurement method is essential for investigation of atmospheric ice. Here, the ice adhesion test approach is adopted from [18] with some modifications.

3.5.8.1 Beams

Each test included three sample beams and three reference beams. Each beam was made of aluminum with approximate dimensions of 340mm×32mm×6.4mm, depicted in figure 3.6. The reference beams had clean smooth surfaces while the coated substrates were attached to the sample beams using two tiny bolts and nuts. After each icing process, the entire set was balanced by adding proper amount of counterweight.

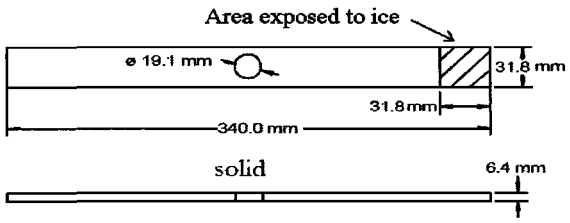

Figure 3.6: Test beam dimensions.

As mention in chapter 2, supercooled water droplets in presence of nucleation sites (such as solid surfaces) can accumulate in the form of atmospheric ice, which is quite different from the ice prepared with other methods. Due to our focus on the behaviour of

atmospheric ice on the coated materials, one of the following icing procedures was followed for each experiment.

3.5.8.2 Icing procedure 1

A series of tests were performed in Anti-icing Materials International Laboratory (AMIL), University of Québec in Chicoutimi. In each experiment, three sample beams and three references beams were placed on a support in at -8°C in the cold room shown in figure 3.7 [18].

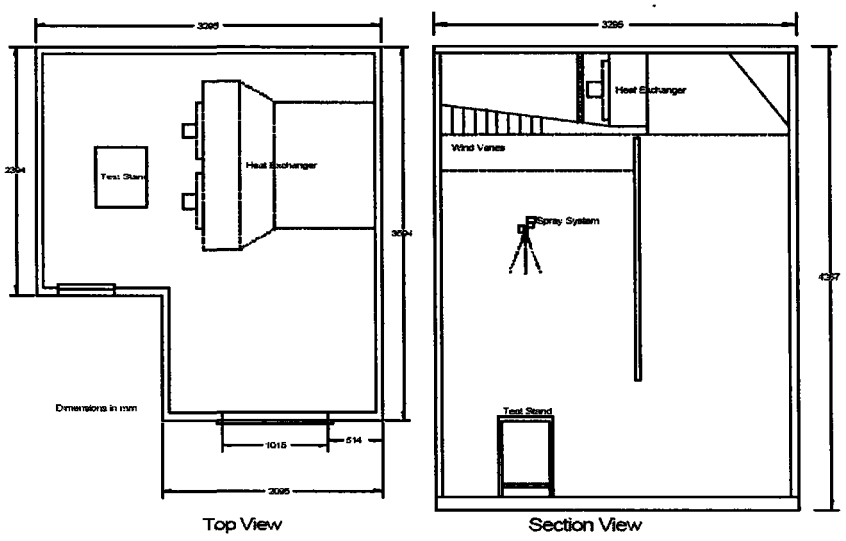

Figure 3.7: Freezing room in Anti-icing Materials International Laboratory (UQAC).

After 30min, pre-cooled water (4°C) was conducted through sealed pipes and prayed vertically toward a test stand. The spray rate, size of nozzle and vertical distance were selected properly so the falling droplets could reach to thermal equilibrium state before getting to the test stand. The beams were covered in the way that only the testing area of

each sample was open to the droplets. The exposure of beams to freezing water spray was continued until an accumulation of ~1cm detected on the samples. The average density of ice was ~0.87 g/cm^3. The samples were kept at -10°C for 30min prior to centrifuge adhesion test.

3.5.8.3 Icing procedure 2

In the second series of experiments, the ice accumulation conditions were created in the CIGELE atmospheric icing research wind tunnel, illustrated in figure 3.8. This wind tunnel is a closed-loop low-speed icing wind tunnel which can emulate icing conditions identical to those encountered during various icing processes in nature. The system is highly controllable and many parameters can be adjusted such as air speed, temperature and liquid water content [170].

The technique used in this experiment was to inject room temperature water via warm nozzles into a cold air stream. Water and air are supplied to the three nozzles on the spray–bar through independent lines of water and air for each nozzle. The distance between the nozzles and the sample holder was long enough to obtain thermodynamic equilibrium for even the largest droplets at the highest air velocity. The air and water pressure were 15 psi (~103kPa) and 55 psi (~379kPa), respectively. Air temperature during experiment was equal to -10°C with ±0.5°C accuracy, and the air velocity value was adjusted to 10m/s [171].

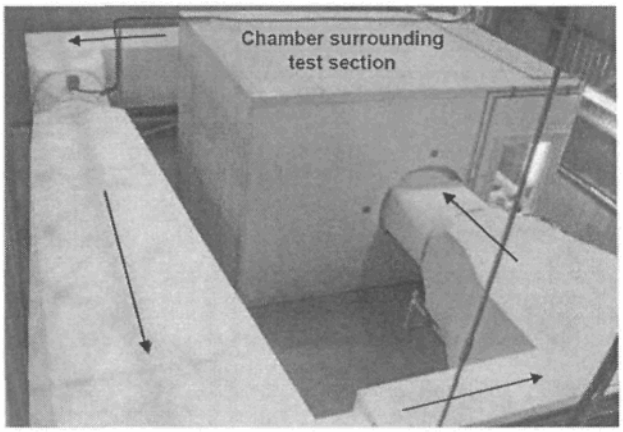

Figure 3.8: A view of the CIGELE atmospheric icing research wind tunnel

Before ice accumulation, the coated substrates were cleaned with nitrogen flow to get rid of dust and loose particles, attached to the sample beams, weighed precisely and finally placed in the tunnel for 15min to be cooled down. A sample holder was designed to place three sample beams in the middle of the test section of the wind tunnel in a vertical state. There was a U-shaped aluminum airfoil for each beam which could conduct the air flow without causing any turbulence. Therefore, for each beam only the coated substrate was exposed to the air enriched with water droplets. Figure 3.9 shows the sample holder and the reference samples. After ice accumulation was finished, the samples were removed from the test section and kept in a climatic chamber at -10°C. The beams are weighed following icing and the surface area covered with ice was recorded for each sample. The time period needed to have approximately 5g of ice on each sample was recorded too.

Figure 3.9: A view of reference sample beams and airfoils in wind tunnel.

3.5.8.4 The centrifuge Adhesion Test

The ice adhesion tests were performed using the method introduced by AMIL [18]. This method is simple, fast, reproducible with variations of less than 15%, and able to work with atmospheric ice. The centrifuge test machine can accelerate an iced sample beam from 0 to 10000 rpm with an acceleration of approximately 300 rpm/s. Rotation generates a centrifugal force and when this force is more than adhesion force of ice, the ice detaches from the sample.

The iced beams were individually tested in the centrifuge test machine (figure 3.10) placed in a cold room at $-10.0°C \pm 0.1$. There, the beams were rotated at increasing speeds from 0 up to the point the detachment took place. The rotor speed and time at which detachment happened and ice hit the walls of system was determined from the data stored in computer and was applied to calculate the adhesion reduction factor.

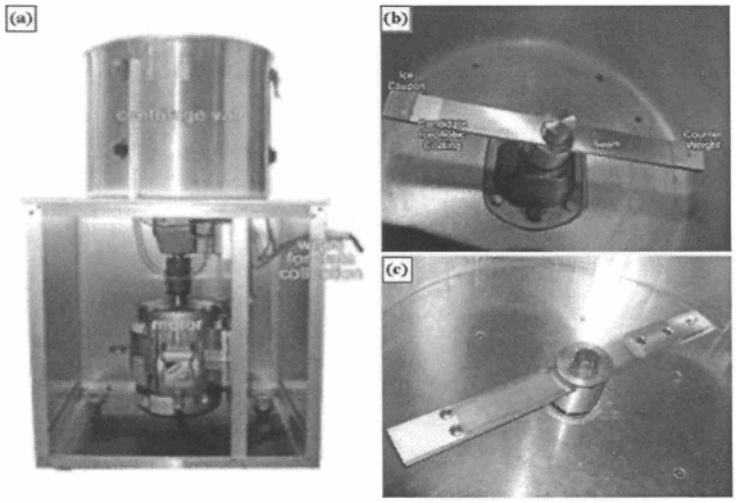

Figure 3.10: (a) Centrifuge test system of AMIL group from (a) outside and (b) inside, and (c) the test system of CIGELE from inside.

CHAPTER 4

RESLULTS AND DISCUSSION:

PROPERTIES OF SILVER AND COPPER

NANOPARTICLES

In this phase of the present work, model nanostructured surfaces were prepared in order to examine the correlation between the wetting behaviour and their parameters, i.e. particles size, density, topography etc. As mentioned in Chapter 2, two conditions are necessary to produce a superhydrophobic surface: (1) a specially-designed roughness or texture on the surface; (2) an intrinsically hydrophobic material for the outermost layer. The steps of the approach to have a superhydrophobic surface are depicted in figure 4.1.

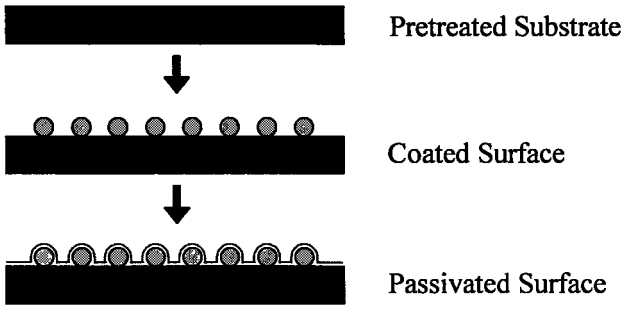

Figure 4.1: Schematic illustration of two-step process to prepare superhydrophobic surfaces.

It involves a substrate, which is usually pre-treated, and some kind of micro/nano-sized coating. The textured surface is then covered with another substance, which makes the entire surface hydrophobic. The nanoparticles must be close together enough such that water can not penetrate between them (i.e. almost touching). These surfaces are commonly referred to as composite surfaces, because of high chance of having a composite mixture of water-solid interface area and water-air interface area underneath a macroscopic water droplet on the surface. By varying the size and the separation between the particles it is possible to prepare surfaces where the water droplet is pinned or rolls off easily. Among different fabrication methods available, spin coating was selected herein as the main

coating method for bringing the nanoparticles on the substrate surfaces. Spin coating is a commonly used technique for preparing uniform thin films on flat substrates.

4.1 Silver Nanoparticles

Three different approaches were attempted to prepare silver nanoparticles needed to make rough model surfaces. The experimental details and achieved results are as follows:

4.1.1 Silver Nanoparticles Type 1

The alcohol-base process is one of the most efficient ways for the preparation of fine powders of easily reducible metals [159,172]. Alcohol-medium preparation of nano-particles can be carried out using two approaches: (a) the "precursor heating" method, where a solution of metal salt in alcohol is prepared at room temperature then heated to the reaction temperature, and (b) the "precursor injection" method, in which a metal salt solution is injected into a hot solvent [173]. In the former approach, the rising rate for temperature is the main parameter governing the particle size. On the other hand, the injection rate and the reaction temperature are determining factors of the latter method. A precise control of temperature is essential to have more uniform particle size distribution (monodispersity) [173]. The second approach was followed here.

Under the effect of heating or additives, dehydration reaction of EG takes place where one molecule decomposes to two molecules of water and acetaldehyde. This reaction is reversible and can be affected by catalysts and by the pH of the solution [174].

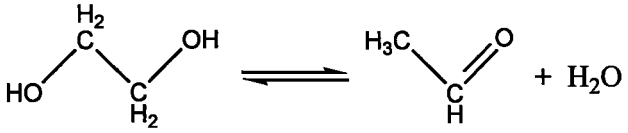

In the presence of Ag ions, a second reaction occurs in which simultaneous double oxidation of acetaldehyde leads to diacetyl and reduction of Ag^+ generates neutral Ag atoms [175]. The generated organic molecules are volatile and leave the solution as bubbles. Therefore, the reaction is almost irreversible.

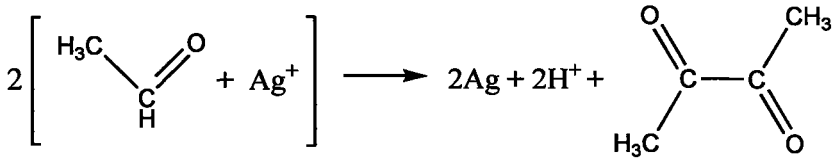

The generated Ag atoms in the solution associate to form small clusters, which are dynamic entities having continuous aggregation–dissociation evolutions.

$$n\,Ag \leftrightarrow (Ag)_n^{cluster}$$

When the solution reaches a saturation level of Ag atoms, the clusters absorb the excess atoms and grow to a critical size and thus form nuclei, which are the first stable entities of the metal [176].

$$(Ag)_n^{cluster} + m\,Ag \rightarrow (Ag)_{n+m}^{cluster}$$

The number and size of the nuclei depend on the reduction-oxidation potential of the reaction (redox), temperature, concentration of reactants and additives, and the properties of the solvent [157]. These nuclei grow rapidly and the Ag atom concentration is lowered to a point below the nucleation concentration, but high enough to allow particle growth to continue at a rate that can consume all the generating metal atoms [172]. As more metal

atoms are generated, the primary particles can continue to grow by diffusion to form larger single-crystal particles, or they may aggregate to form poly-crystal particles. The free growth of the particles leads to the particle sizes up to several micrometers and finally they precipitate, with a wide range of shapes and sizes (poly-dispersed).

To have nanoparticles with desirable properties, the growing and the aggregation processes must be controlled. A number of materials have been reported to act as protective agents for controlling the colloidal particle growth. Among them, PVP is one of the most commonly used (figure 4.2) [159,172]. Adding a precise amount of PVP inhibits the possibility of bonding the newly reduced Ag atoms and controls the particle size distribution.

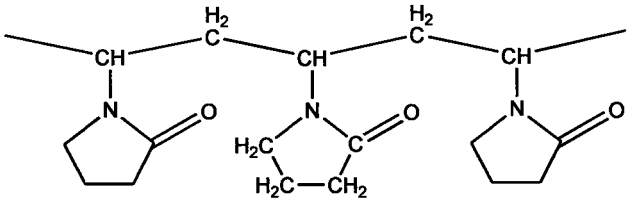

Figure 4.2: A group of three monomers in a PVP polymer chain.

It is worth noting that having a reaction termination step is essential after achieving a desirable colloid. This can be done by adding a proper amount of acetone [177].

UV–visible spectrometry is the standard measurement to trace the shape and size evolution of Ag nanoparticle during the growth process because Ag nanostructures with different shapes and sizes exhibit different surface plasmon resonance bands at different frequencies [178]. Appendix C includes more details about UV–visible spectrometry. Figure 4.3a shows the variation of the UV–visible absorption spectra of a Ag colloid, taken

at various reaction times from 1 to 60 min (after the addition of $AgNO_3$ and PVP). The strong resonance peak at 420nm clearly shows the presence of Ag particles [179]. At the initial stages, the solution exhibits a transparent pale brown color. After 5min, the solution turns slightly opaque and its color changes to dark yellow. The change in color implies that the most of Ag^+ ions are coordinated with PVP molecules [180].

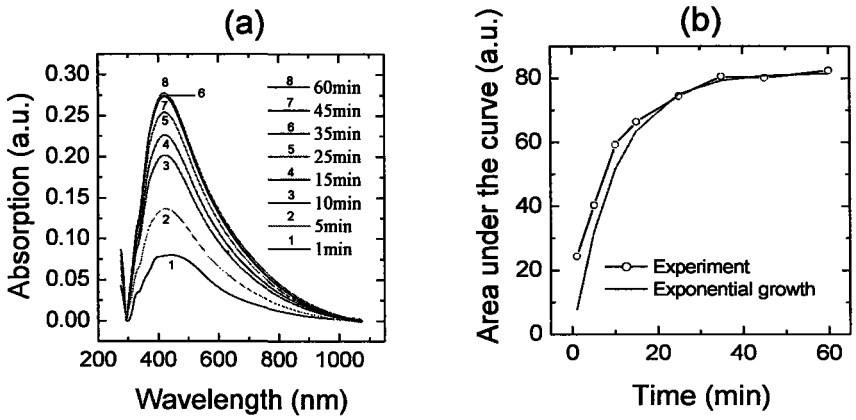

Figure 4.3 : Time evolution of nanoparticles in UV-visible spectra (a) the absorption spectra in different instants, and (b) the area under the curves in (a).

The appearance of plasmon resonance peak around 420 nm indicates the formation of nearly spherical Ag nanoparticles. Over time, the peak intensity increases and it became narrower, stating an increase in the number of Ag nanoparticles in the reaction solution. As the reaction proceeds over about 35 min, no obvious changes in the absorption spectrum are observed in figure 4.3a. The number density of the particles is proportional to the area of the absorption curve. The increment in this quantity in figure 4.3b is mostly related to the

larger number of particles with the same size distribution range, as no shift in peak position is seen.

The above mentioned experiment can provide stable Ag colloids which can keep their properties for more than two months (verified with UV-vis spectra). The reaction is not fast and can be terminated at any time to inhibit the particles from further growth by adding large amounts of acetone in the mixture [177]. Precise selection of ingredient quantities and reaction parameters may lead to desirable range of particle sizes and shapes. The particles did not precipitate on the flask walls and remained in the solution even after cooling down. Also, the molar ratio of $AgNO_3$ and PVP monomers was not high (~1.5), therefore removing of PVP from the particles was by washing with 1-2 fold acetone.

On the other hand, preparation of rough surfaces based on metallic nanoparticles, as one goal of this study, required relatively large amounts of such particles, which is not a straightforward task. Doubling the concentration of reactants leads to higher agglomeration rate and a much wider UV-vis spectrum, indicating a larger distribution of particle sizes. The reaction is also time-consuming and it takes four five hours including the preheating and cooling periods. Although having many adjustable parameters gives the flexibility to the reaction, but it makes the reaction hard to control and small inadvertent changes in parameters may result in unwanted outcomes. The UV-vis test showed that results were different when reaction was performed in an ordinary flat-bottom beaker or in a round-bottom flask. Apparently, in the case of beaker the circulation is not uniform throughout the solution so much wider UV-vis curves were achieved. Very precise control of the reaction temperature was also important. To have a better heat exchange rate between a planer hot-

plate and round flask, a bronze part was designed, which acted as both a heat conductor and heat capacitor (figure 3.1). Using this heat conductor led to much more reproducible experiments. The injected solutions of $AgNO_3$ and PVP are at room temperature so the injection rate can strongly influence the solution temperature and finally the achieved result. Although the experimental parameters used in this work were close to those applied by others [159], the particles obtained here spherical rather than cubic. The difference could be explained by the use of an automatic injection system and more precise control of solution temperature in the work of Sun and Xia [159].

Figure 4.4 shows SEM images of Ag nanoparticles prepared in alcoholic medium. These particles were washed with acetone three times to get rid of PVP traces then deposited on Si substrates. The Ag particles are almost spherical with distinguishable facets. It is worth mentioning that the particles in the SEM images were separated from colloid by using a centrifuge system which separates the bigger particles from liquid easier compared with smaller particles. It is possible that very small particles remained in the liquid and therefore one can not find them in figure 4.4.

At lease 10 different AFM images of a nanoparticle-coated silicon substrate were analyzed in order to understand the size distribution of nanoparticles. According to the manufacturer, the applied tapping-mode tip of AFM had a radius of curvature on the order of 30-50 nm which can lead to an increased apparent diameter of ~15 nm for each particle. However, this error has been neglected here. The selected size categories and the calculated percentage for each are depicted in figure 4.5. The range of particle sizes in these images is from 100 nm to 600 nm with an approximate average of 361 nm.

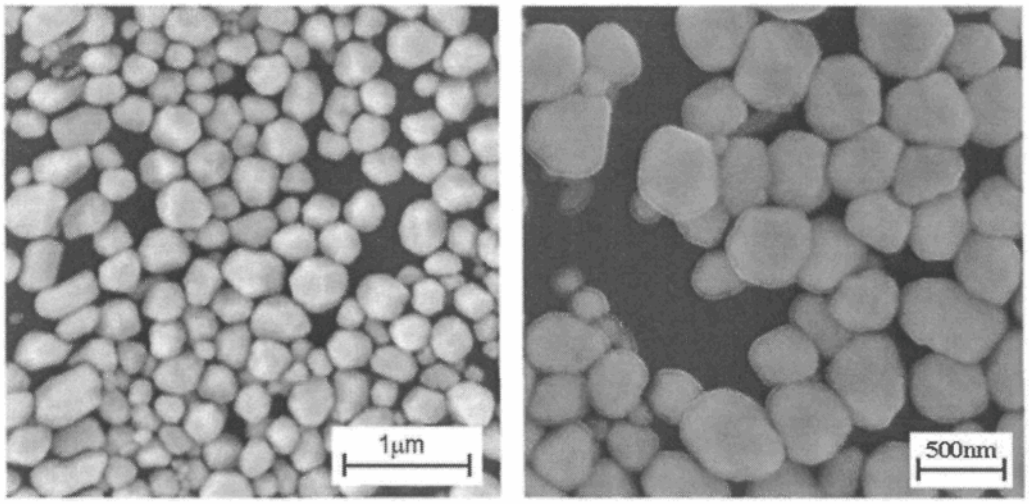

Figure 4.4: SEM images of silver nanoparticles prepared through precursor injection into alcohol medium at 160°C.

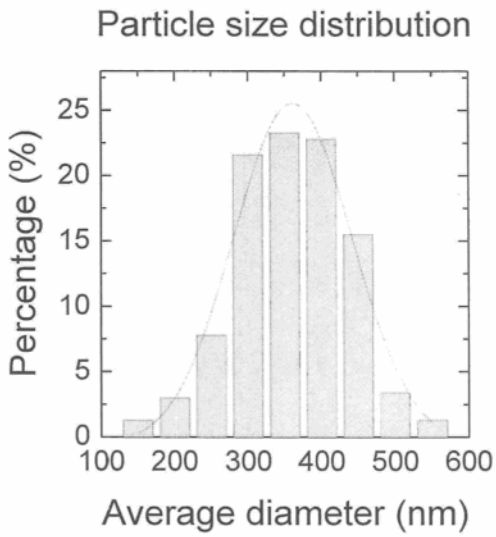

Figure 4.5: Size distribution of silver nanoparticles of type 1.

Table 4.1: Size distribution groups of silver nanoparticles of type 1, shown in figure 4.5.

Average diameter (nm)	Mid-size (nm)	Percentage
<174	150	1.3
175-224	200	3
225-274	250	7.8
275-324	300	21.6
325-374	350	23.3
375-424	400	22.8
425-474	450	15.5
475-524	500	3.4
>525	550	1.3

4.1.2 Silver Nanoparticles Type 2

Although the previous synthetic method is well-known and controllable, for our purpose it is quite time-consuming and complex. More rapid synthesis of nanoparticles, able to speed up the total process, was considered as more attractive. In aqueous state, silver nitrate solution has acidic pH (5 for 2% w/v). By adding strong bases, Ag^+ ions precipitate without being reduced as a solid mass of silver oxide. For example, in case of KOH we have:

$$2Ag^+(NO_3)^- + 2K^+OH^- \rightarrow Ag_2O\downarrow_S + K^+(NO_3)^- + H_2O$$

In presence of Ag_2O, the solution color changed to dark brown-black. The precipitation rate completely depends on the amount of PVP in the medium and higher PVP concentration reduces the particle sizes and increases the precipitation period.

Further conversion of Ag_2O to Ag particles was performed through the reaction below:

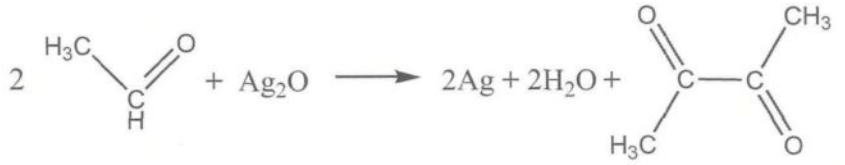

In this reaction, after adding KOH the color changes to green-brown indicating the presence of silver nanoparticles, as shown in figure 4.6.

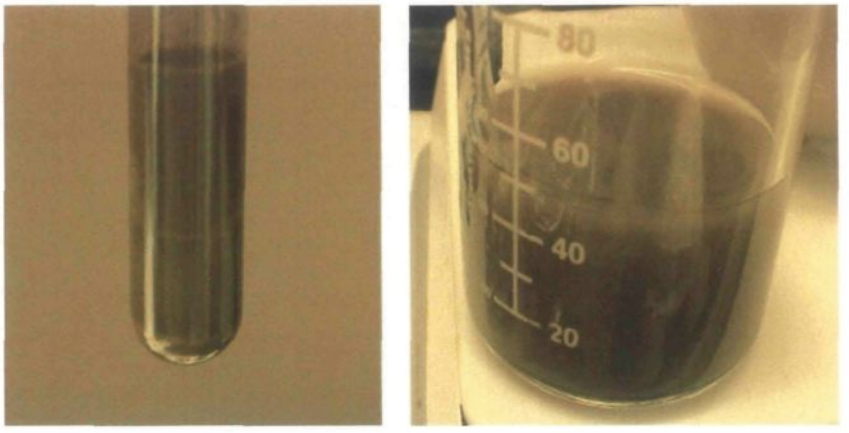

Figure 4.6: Colloid of silver nanoparticles prepared in aqueous basic medium.

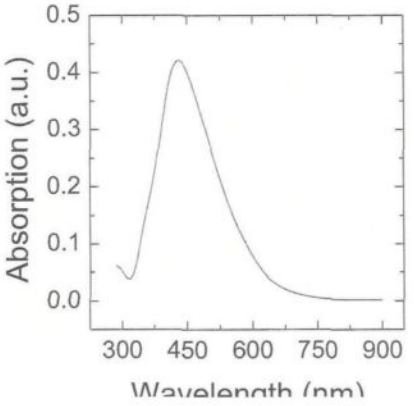

Figure 4.7 : UV-visible absorption of silver nanoparticles in basic medium.

Figure 4.7 presents the UV-visible spectrum of the as-prepared colloidal Ag particles in basic medium. Similar to the previous experiment, the prominent absorption peak at around 430 nm confirms the presence of Ag nanoparticles in the solution, compatible with reported in the literature [179].

Because of the strong base (KOH), the reaction is fast and the time evolution of particles is not possible. Immediately after injection of KOH into the mixture, a green-brown color appears indicating the presence of nanoparticles and it does not change with passing the time. This observation agrees well with UV-visible study which indicates no change in the absorption curve over time, except a decrease in amplitude caused by precipitation of particles after more than one day.

This method is fast, simple and practical. No heat source or hot-plate is required and only stirring is sufficient. It is also scalable and can be performed in higher quantities without a major change in results. No difference in UV-vis spectra was found between experiments with either flat-bottom or round-bottom flasks. Injection rate was not important too. On the other hand, the reaction is fast and not traceable with UV-vis. The particles are not very uniform in shape and removal of PVP from them is more difficult because of the higher ratio of PVP/Ag as compared to the previous experiment.

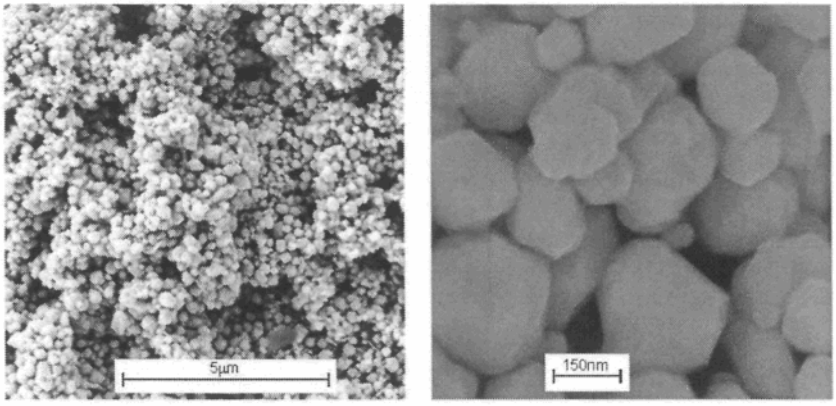

Figure 4.8: SEM images of silver nanoparticles of type 2, prepared in basic medium.

Figure 4.8 illustrates SEM images of Ag nanoparticles prepared in aqueous basic medium. The range of particle sizes in these images is from 80 nm to 400 nm with an average of ~263 nm, presented in figure 4.9.

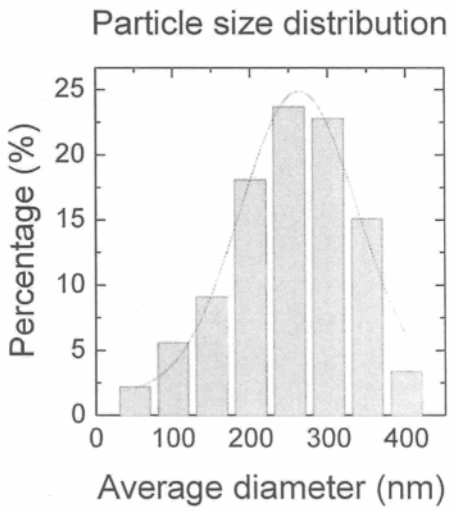

Figure 4.9: Size distribution of silver nanoparticles of type 2.

Table 4.2: Size distribution groups of silver nanoparticles of type 2, shown in figure 4.9.

Average diameter (nm)	Mid-size (nm)	Percentage
<74	50	2.2
75-124	100	5.6
125-174	150	9.1
175-224	200	18.1
225-274	250	23.7
275-324	300	22.8
325-374	350	15.1
>375	400	3.4

4.1.3 Silver Nanoparticles Type 3

Ascorbic acid ($C_6H_8O_6$) can react as a reducing agent via oxidation to semidehydro-ascorbate radical and dehydroascorbic acid [181], as shown in figure 4.10. The released hydrogen radicals react rapidly with free hydroxyl radicals and oxygen and prevent the nanoparticles from oxidation.

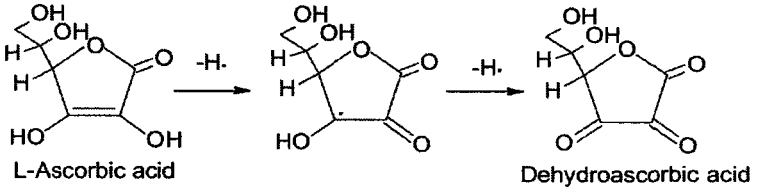

Figure 4.10: Antioxidation mechanism of ascorbic acid [181].

Thus, Ag^+ ions can be reduced to metal silver by ascorbic acid according to the following reaction [182]:

$$2Ag^+ + C_6H_8O_6 \rightarrow 2Ag^0 + C_6H_6O_6 + 2H^+$$

Figure 4.11 illustrates SEM images of Ag nanoparticles prepared in acidic medium. The particles are almost spherical. In absence of EG, the reaction was fast and the resulting solution was dark-gray color, indicating agglomeration process and large particles formations. The rapid precipitation of the colloid confirmed this fact. Addition of 25% (by volume) of EG reduced the rate of diffusion growth and the final colloid had a pale gray color with much longer stability.

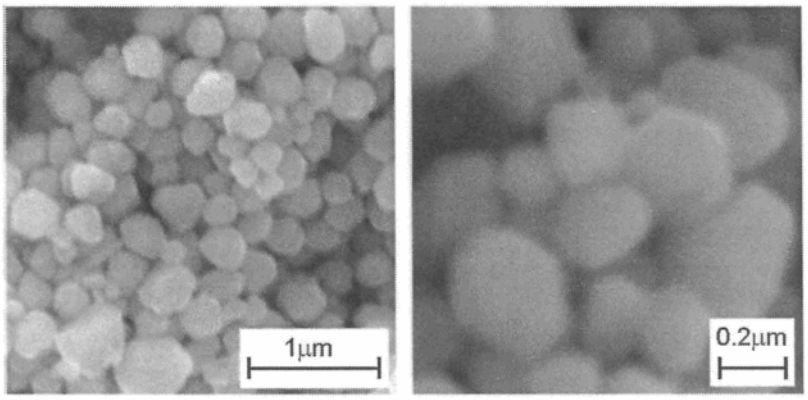

Figure 4.11: SEM images of silver nanoparticles prepared in acidic medium.

Table 4.3: Size distribution groups of silver nanoparticles of type 3, shown in Figure 4.12.

Average diameter (nm)	Mid-size (nm)	Percentage
<70	50	1.5
70-109	90	3.6
110-149	130	12.4
150-189	170	27.8
190-229	210	27.8
230-269	250	14.9
270-309	290	9.3
>310	330	2.6

As shown in figure 4.12, in this case the particles had a size range from 50 nm to 300 nm with an average of ~194 nm. Figure 4.13 depicts the UV-visible spectrum of the as-prepared colloidal Ag particles in acidic medium. Here, the peak position is at ~490 nm.

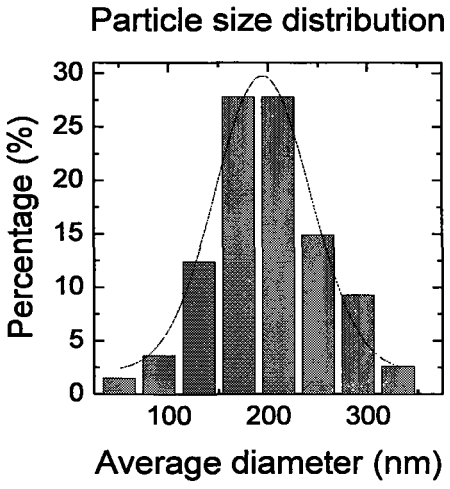

Figure 4.12: Size distribution of silver nanoparticles of type 3.

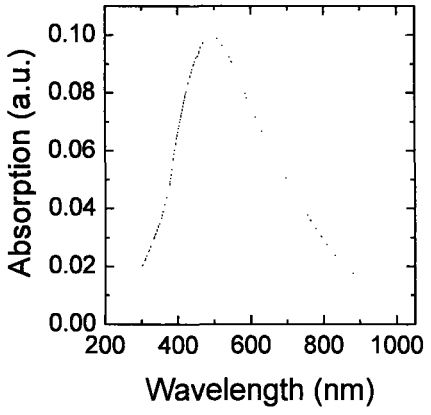

Figure 4.13: UV-visible absorption of silver nanoparticles in acidic medium.

This method is also fast and practical. No heat source or hot-plate is needed and only stirring suffices. The reaction vessel is not affecting and no difference in UV-vis spectra was detected by from experiments with flat-bottom or round-bottom flasks. The reaction is also scalable and can be performed in higher quantities with similar results. Injection rate was not important too. The particles were protected from oxidation and had relatively uniform size and shape (as seen in figure 4.11).

Due to rapid reaction, tracing the particle evolution with UV-vis was not possible. Separation of PVP from the particles was even more difficult because of high PVP/Ag ratio. The reaction should be terminated by adding large amounts of water, otherwise agglomeration leads to big formations which precipitate rapidly on the vessel walls.

4.2 Copper Nanoparticles

4.2.1 Copper Nanoparticles Type 1

In this experiment, EG was used as the solvent and not as a reducing agent. Although EG could serve as a reducer in many other cases, it could not be used as a reducing agent in a solution of Cu (II) [183]. It has been also reported that ascorbic acid alone can not reduce copper salt [184] or leads to very tiny particles [181]. In the present experiment, high temperature EG medium helps facilitate the reduction of Cu^{2+} ions at a temperature higher than the boiling point of water. Figure 4.14 shows a SEM image of Cu nanoparticles prepared in this experiment. Many different shapes and sizes of the particles are observed.

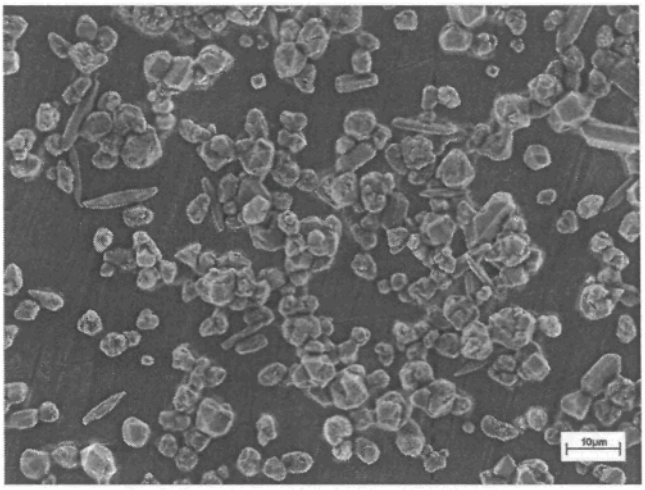

Figure 4.14: SEM image of copper nanoparticles of type 1, prepared in alcohol medium.

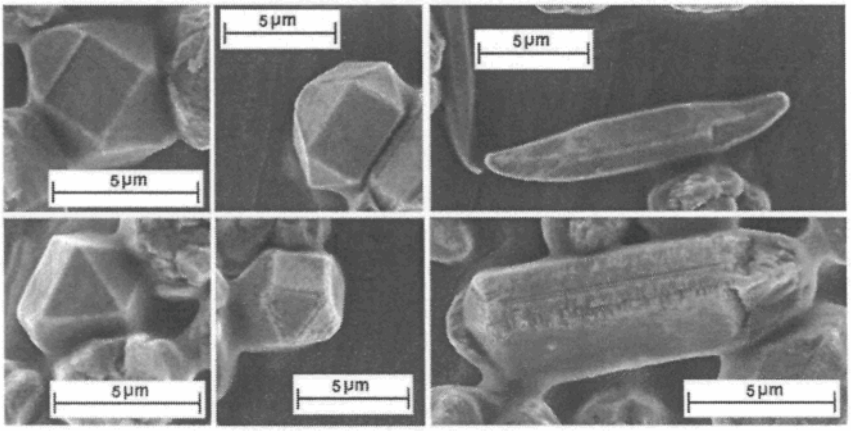

Figure 4.15: SEM images of different morphologies of copper particles of type 1.

Figure 4.15 depicts six different morphologies of copper particles found in the outcome of this experiment. The particles are in micrometer range with clear facets. Some reasons can be considered for the growth of large particles, such as difference in case of Cu compared with Ag, lower capping power of PVP for copper compared with silver and dissimilarity in reducing agent. Apparently, the last one is the most important one.

Figure 4.16 shows the UV-visible spectrum of the Cu particles. The prominent absorption peak at around 650 nm is close to those reported in the literature [183].

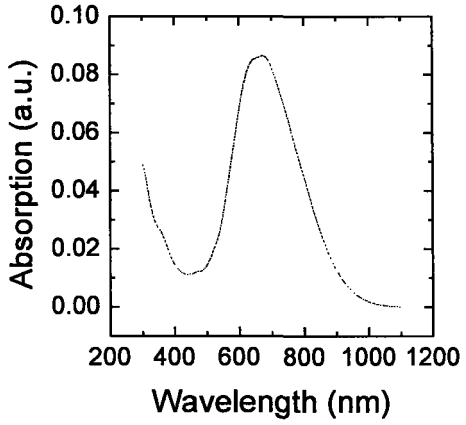

Figure 4.16: UV-visible absorption of copper particles prepared in alcohol medium.

It was detected that Cu particles precipitated on the flask walls even during initial steps of the reaction. Also, the colloid after centrifugation was not stable and the particles precipitated very fast. All these observations confirm the large sizes for particles in agreement with the SEM images in figure 4.15. At temperatures below 100°C, reaction rate was observed to be much lower and the reaction did not start under 70°C. Presence of very large particles caused some difficulties in separation procedure using centrifuge and the large fraction of copper mass was consumed by large particles. The reaction is very sensitive to injection rate of reactants which can strongly influence the temperature and finally particle size. To be evaporated, the water content of the injected ascorbic acid absorbed high amount of energy and decreased the solution temperature. To compensate for

this, it was necessary to use a temperature sensor inside the solution rather than the hot-plate sensor. Also, the thermal contact between the round-bottom flask and bronze heat conductor should be good enough to transfer the absorbed heat of boiling. Immediately after finishing the water in the mixture, a sharp increase in temperature is likely to happen so the temperature set point should be reduced in advance. This makes the procedure somewhat complex and far from being reproducible or scalable.

4.2.2 Copper Nanoparticles Type 2

In an initial step, copper particles were produced by reduction of Cu^{2+} ions with sodium borohydride, via this reaction.

$$Cu^{2+}SO_4^{2-} + 2NaBH_4 \rightarrow Cu^0 + H_2 + B_2H_6 + Na_2SO_4$$

This is approved by the appearance of a yellow color. $NaBH_4$ is a strong reducing agent which can produce instantaneously a large density of nucleation centers. The generation rate of reduced atoms is so high that these atoms reach together and form lots of clusters and finally many small particles.

Figure 4.17 depicts the UV-vis spectrum with an absorption peak at 260 nm. For this test a quartz cuvette was necessary to record a meaningful spectrum starting from 220 nm. The obtained particles were very sensitive to oxygen, which caused their instability. Even with N_2 purging, the yellow color of their solution turned to pale-blue of the initial solution after 30 min. In absence of purging, the particles got oxidized and finally black precipitate of copper oxide appeared within 30 min. In addition, due to its high amount, removing of

PVP from such small particles could not be done. This fact led to failure of SEM imaging and only some images of burned material were obtained. AFM was not helpful too.

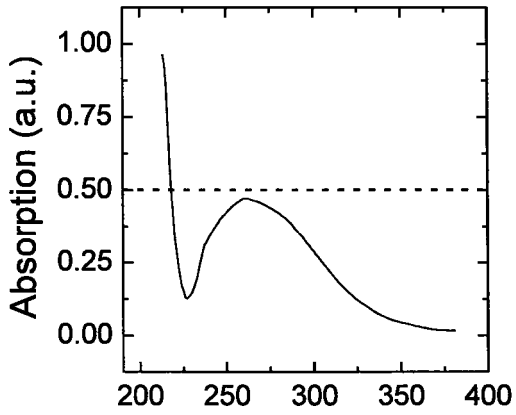

Figure 4.17: UV-visible spectrum of copper nanoparticles of type 2, prepared using $NaBH_4$.

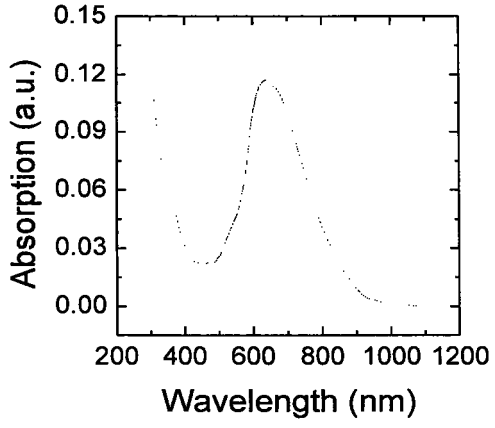

Figure 4.18: UV-visible spectrum of copper particles prepared using $NaBH_4$ followed by ascorbic acid.

Although ascorbic acid can not effectively reduce copper ions, it can be used to continue the reduction process which is initiated by other reducing agents. Herein, after generation of small Cu particles by reduction of Cu^{2+} by$NaBH_4$, the remaining ions were reduced and joined the particles to produce larger ones. This fact was verified by UV-vis spectrum of figure 4.18. An absorption peak appeared at 635 nm which indicates the presence of larger particles.

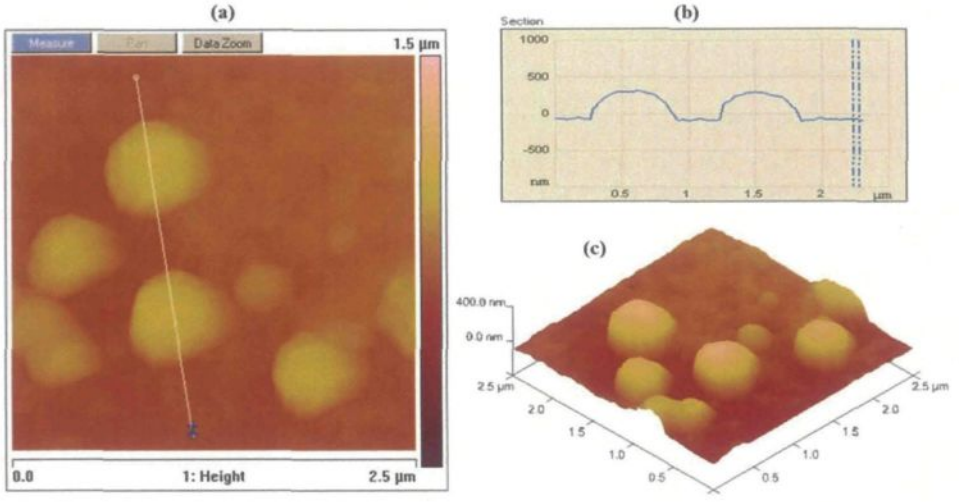

Figure 4.19: AFM results of copper nanoparticles prepared using $NaBH_4$ followed by ascorbic acid: (a) 2D image, (b) cross section along the white line in (a), and (c) 3D image of (a).

The particles were washed and coated on silicon and dried well for AFM imaging (see figure 4.19). Such particles were found to be almost spherical with average diameter of ~400 nm. No other shape was observed for the particles.

4.3 Summary

Experiments have been carried out to study three preparation methods for silver nanoparticles and two approaches for copper nanoparticles. Also, the outcomes of each experimental method have been discussed. From the obtained results, the following conclusions can be drawn:

- Different approaches are required to synthesize nanoparticles of different sizes or shapes. Depending to the type of material, a unique approach must be selected.
- In the case of silver, the largest particles were obtained by injecting precursor to alcoholic solution and the smallest ones by using ascorbic acid in aqueous/alcoholic medium.
- In the case of copper, reduction of copper sulphate with ascorbic acid in alcoholic medium resulted in larger particles compared with the particles prepared in two-step process: sodium borohydrade and ascorbic acid in aqueous/alcoholic medium.
- Silver nanoparticles were adequately stable and their colloid kept their properties for more than one month. Copper particles have generally limited stability and higher affinity to get oxidized or precipitate.

CHAPTER 5

RESLULTS AND DISCUSSION:

SUPERHYDROPHOBIC SURFACES

As mentioned previously, the work done here was aimed at developing of a model anti-icing coating. The preparation procedures of rough nanoparticle-based films are described in chapter 4. In this chapter, the achieved results on wetting properties of these model surfaces are presented and discussed.

5.1 Effect of Passivation on Smooth Surfaces

Passivation is the process of covering a solid surface with a specific substance in order to lower the surface energy. In this study, three kind of passivating material were used and the obtained results are presented below.

The first passivating agent examined here was a set of fatty acids with a single saturated hydrocarbon chain of different lengths, including lauric acid ($CH_3(CH_2)_{10}COOH$), palmitic acid ($CH_3(CH_2)_{14}COOH$) and stearic acid ($CH_3(CH_2)_{16}COOH$), as depicted in figure 5.1. Saturated long chain *n*-alkanoic acids ($C_nH_{2n+1}COOH$) have a polar unit (-COOH, also called as head) which can be absorbed on and make bonds with high energy solid surfaces. On the other hand, the non-polar saturated chain (tail) remains almost perpendicularly to the surface and has a low affinity to water. This absorption is an acid-base reaction, and the driving force is the formation of a surface salt between the carboxylate anion and a surface metal cation. There are reports confirming the adsorption of *n*-alkanoic acids on aluminum oxide [185,186] and silver [187]. An example of fatty acids is stearic acid which is shown to be chemisorbed on silver as carboxylate with its two oxygen atoms bound symmetrically to the surface [188].

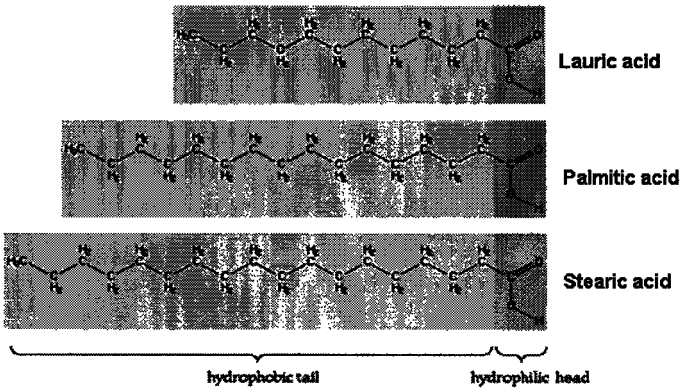

Figure 5.1 : Structure of stearic acid molecule.

Fourier transform infrared (FTIR) spectra can be used to track the presence of the $-CH_n$ groups. Figure 5.2 illustrates the obtained FTIR spectra of three silicon samples passivated by lauric acid, palmitic acid and stearic acid respectively, in high-frequency region (the wave number range of 2700-3100 cm^{-1}). The two large peaks at 2917 and 2850 cm^{-1} are close to those previously reported for asymmetric and symmetric C-H stretching modes of $-CH_2$ groups in organic acids, respectively, and the peak at 2954 cm^{-1} is related to the asymmetric in-plane C-H stretching mode of the $-CH_3$ group [189].

Surface energy of chemically homogenous surfaces is well known to decrease in the following order when hydrogen atoms are gradually substituted with fluorine in surface terminating groups: $-CH_2 > -CH_3 > -CF_2 > -CF_2H > -CF_3$ [102]. Therefore as an alternative approach, coating the surface with PTFE was selected which is known to be rich in fluorine. A thin layer of PTFE was coated by sputtering by argon plasma. Figure 5.3 depicts the FTIR absorption spectrum of a silicon substrate coated with sputtered PTFE. The strong peak located around 1215 cm^{-1} is assigned to the vibrations of $-CF_2$ groups

[190]. The deposited passivation layer is believed to be chemically close to PTFE, as the dominating species observed is $-CF_2$, similar to PTFE [191].

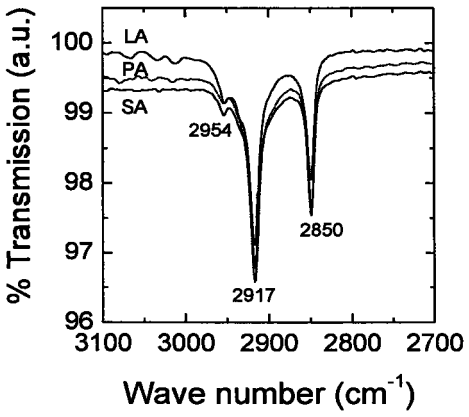

Figure 5.2: Transmission FTIR spectra for lauric acid (LA), palmitic acid (PA) and stearic acid (SA) on silicon in the high-frequency region.

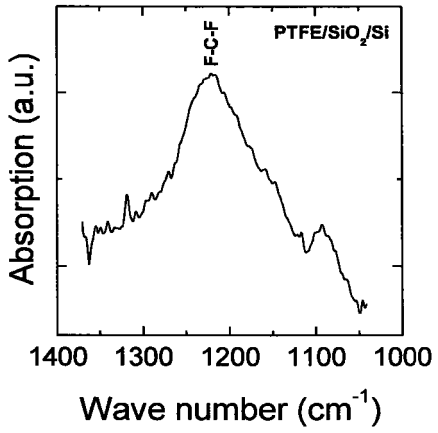

Figure 5.3: FTIR absorption spectrum of PTFE coated on silicon by sputtering.

Another passivation approach was carried out using a perfluroalkyl methacrylic copolymer called Zonyl 8740. According to the supplier, Zonyl 8740 is an aqueous fluorochemical that provides a durable, subsurface, transparent protective barrier against oil and water on porous minerals [192]. This material is believed to act effectively as a binder for nanoparticles as well, and some superhydrophobic surfaces have been reported on its application as a binder for metal oxides nanoparticles [164,165]. Similar to fatty acids, Zonyl 8740 has a -COOH group [193], compatible with our measured pH of ~6 for an aqueous solution containing 5 wt.%. It has been reported that the adsorption of Zonyl 8740 onto boehmite (aluminum oxide hydroxide) surface is through the bonding between the OH group in the boehmite and the COOH group in the material [194].

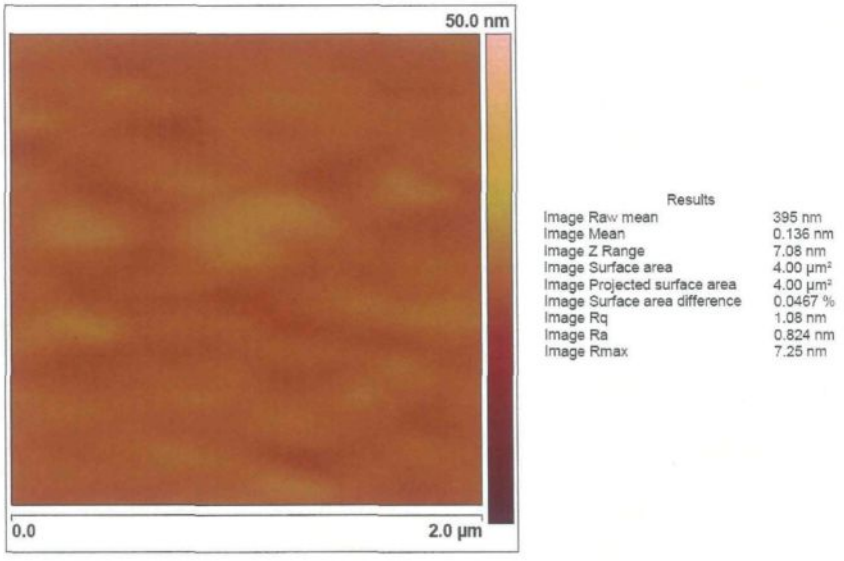

Figure 5.4: The AFM image of the smooth silver surface and its corresponding parameters.

To know the effect of passivation on highly planar silver surfaces, a smooth thin film of silver was prepared on silicon substrate (100) and its morphology was studied with AFM

(section 3.5.1 or [195]). AFM images revealed that the silver layer was homogenous and highly flat. For example, in figure 5.4, the measured RMS roughness (Rq) is determined to have a maximum value of 1.08 nm for an area with 2 μm scan length. This value of roughness is small enough to consider the surface smooth and use this sample for evaluating water contact angle on smooth silver after passivation.

Figure 5.5 depicts a water drop on the smooth silver surface passivated with stearic acid. All the measured values of water contact angles on smooth silver after passivation with different substances (for 30 min in the case of fatty acids and Zonyl 8740) are shown in figure 5.6. The measured contact angles on the fatty acid-passivated surfaces are all smaller than 90°, implying that those surfaces are slightly hydrophilic. The majority of reported superhydrophobic surfaces are based on the materials with water contact angle greater than 90° in their smooth form. However, that is not a necessary condition and it is possible to develop superhydrophobic surfaces using slightly hydrophilic materials [141,196].

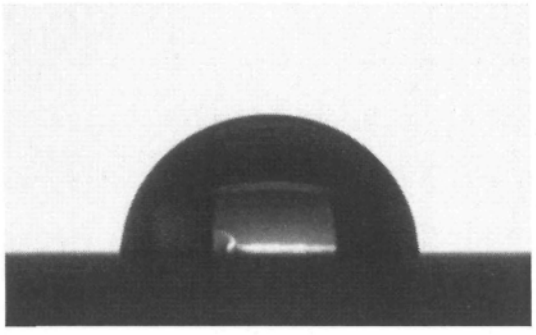

Figure 5.5: A water droplet of 6 μL on the smooth silver surface passivated with stearic acid.

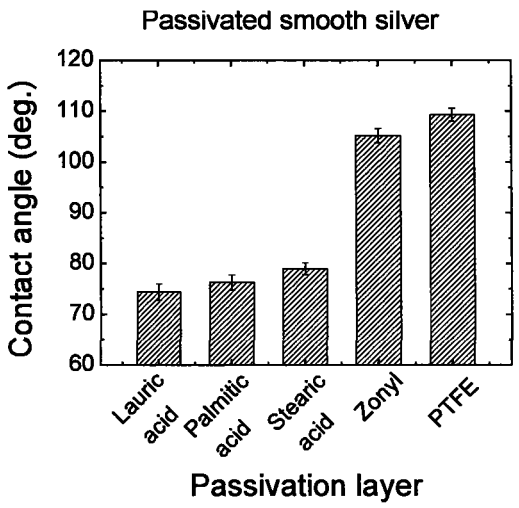

Figure 5.6: Water CA of smooth silver passivated with different substances.

Table 5.1: Measured water contact angle on a smooth thin film of silver with different passivations.

Passivation layer	Contact angle (deg.)
Lauric acid	74.4 ± 1.6
Palmitic acid	76.3 ± 1.5
Stearic acid	79.0 ± 1.2
Zonyl 8740	105.2 ± 1.4
PTFE	109.3 ± 1.3

Self-assembled-monolayer (SAM) is a highly very ordered and packed arrangement of a specific type of molecule on a clean solid surface [197].A self-assembled-monolayer can cover the entire surface. Fatty acids and alkylsilane are examples of such molecules. The arrangement of molecules on the solid surface is not always perfect and there is a probability of having pores, collapsed molecules and lying down monomers as well as self-assembled ones [22]. According to [198] a smooth surface covered entirely with molecules

ending with $-CH_2$ or $-CH_3$ should show a water contact angle of 94° or 110° respectively, but our experiments with fatty acids showed smaller numbers. The possibility of not enough passivation time is not the case because no change has observed with longer passivation periods. It can be deduced that there was a plenty of uncovered areas. The achieved surfaces were not covered perfectly, but their performance was acceptable to be used in subsequent experiments.

5.2 Effect of Coating with Nanoparticles

As mentioned previously, passivation on smooth surfaces can not provide water contact angles larger than 120°, and some surface roughness is needed for higher contact angles. Herein, coating the substrates with a thin film of metallic nanoparticles was the main approach to gain a suitable roughness.

Spin-coating was selected as the main coating method for preparing the nanoparticle-based rough coatings. This is a well-established method to achieve thin films on planer substrates. In a typical spin coating procedure, enough amount of the liquid material is deposited onto the center of a planar substrate. Spinning leads to centrifugal acceleration, providing a uniform coating. Film properties depend both on the nature of colloid, such as viscosity, weight percentage of solid, drying rate, etc. and on spin coating parameters, for example final speed, rotation period and so on.

Selection of proper liquid for carrying the particles on the surface is important. In the present study, the particles were metallic so they had much higher density compared to the liquid in which they were suspended (10.49 $g \cdot cm^{-3}$ for silver and 8.96 $g \cdot cm^{-3}$ for copper).

Therefore, it was necessary to use a high viscosity liquid; otherwise all the nanoparticles would be thrown out of the surface. For this reason, EG was added as a high-viscosity liquid, with viscosity of ~18 times larger than that of water. The colloid should also have a relatively low evaporation temperature and ability to wet the substrate. To satisfy all these requirements a mixture of EG and MeOH was selected, with a ratio of EG:MeOH=1:20. The weight percentage of solid was kept at 10%.

Experiments showed that conventional spin-coating procedure was not successful to provide a film with enough number of particles and a very low amount of nanoparticles remained on the substrate. Heating at 80°C after deposition of colloid and before spinning was found to be effective in increasing the number of remaining particles on the substrate. Such a heating period was called a waiting-time. During waiting-time, a fraction of solvent evaporated and the concentration of particles in the solution increased. A hot-plate warmer than 90°C could result in unwanted agglomeration of particles and a temperature lower than 70°C had no substantial effect.

Table 5.2: The values shown in Figure 5.7.

Waiting time (min)	CA (deg.)	CAH (deg)
0	118.4 ± 2.0	---
10	133.5 ± 1.8	28.2 ± 2.1
15	136.6 ± 1.5	20.5 ± 1.9
20	137.2 ± 1.6	13.5 ± 1.8
25	136.8 ± 1.5	12.1 ± 1.7
30	136.1 ± 1.5	12.0 ± 1.6
60	135.6 ± 1.7	12.2 ± 1.7

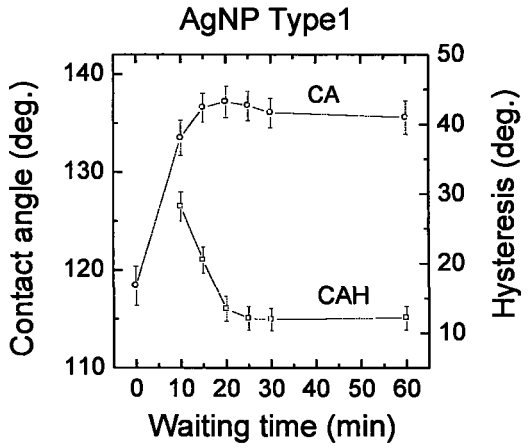

Figure 5.7 : Variation of water CA and CAH versus waiting time for one layer coating of Ag nanoparticles of type 1, coated on copper, and passivated with SA.

Figures 5.7 and 5.8 indicate the behaviour of water contact angle and hysteresis versus waiting time on copper samples coated with one layer of silver nanoparticles of type 1 and type 2 respectively and passivated with stearic acid. When there is no waiting time period both types of nanoparticles showed very low contact angles. The droplets were sticky and hysteresis was not measureable. A 10 min waiting time could result in 15° and 20° increments for the sample coated with nanoparticles of type 1 and 2, respectively.Heating the samples before spinning helped the excess liquid to evaporate and give a more concentrated solution. This increased the possibility of having more particles on the surface after spinning. With very long waiting times some unwanted agglomeration could happen, leading to lower quality and uniformity of the final coating. Based on experimental results, a waiting time of 20 min gives the highest contact angle and reasonably low contact angle hysteresis. This value of waiting time was kept constant for all the subsequent experiments.

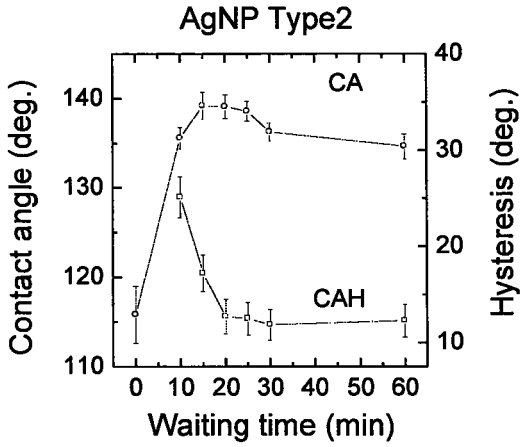

Figure 5.8 : Variation of water CA and CAH versus waiting time for one layer coating of Ag nanoparticles of type 2, coated on copper, and passivated with SA.

Table 5.3: The values shown in Figure 5.8.

Waiting time (min)	CA (deg.)	CAH (deg)
0	115.8 ± 3.2	---
10	135.6 ± 1.2	25.1 ± 2.1
15	139.2 ± 1.5	17.2 ± 1.9
20	139.1 ± 1.3	12.7 ± 1.8
25	138.6 ± 1.1	12.5 ± 1.7
30	136.3 ± 1.0	11.9 ± 1.6
60	134.7 ± 1.4	12.3 ± 1.7

The applied spin-coating process had three steps: 10 s at 300 rpm, 30 s at 600 rpm and 20 s at a range of speeds. Figure 5.9 demonstrates the behaviour of water contact angle and hysteresis versus third spinning speed on copper samples coated with one layer of silver nanoparticles of type 2 after passivation with stearic acid. Increasing the third speed, the contact angle increases rapidly then starts to drop slowly (smaller than error bars, and

negligible). The qualitative effect of speed increment was that using higher speed values led to more uniform and reproducible coatings. When the same amount of particles was better distributed, more surface area was covered by nanoparticles which led to higher roughness and 19° increment in measured contact angle. More uniformity resulted in less variation in contact angles, as indicated by smaller error bars at higher speeds. In addition, with more uniform coatings, the pinning happened rarely and hysteresis had lower values. The value of 2400 rpm was kept constant for all other experiments.

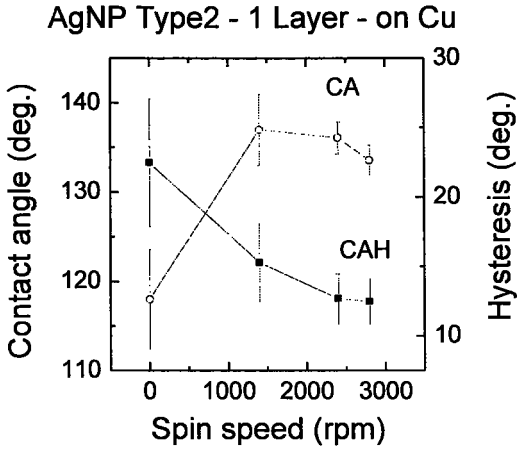

Figure 5.9: Variation of water CA and CAH versus third spinning speed for one layer coating of Ag nanoparticles of type 2, coated on copper, and passivated with SA.

Table 5.4: The values shown in Figure 5.9.

Spin speed (rpm)	CA (deg.)	CAH (deg)
0	118.0 ± 5.6	22.5 ± 4.6
1400	137.0 ± 4.0	15.3 ± 2.8
2400	136.1 ± 1.8	12.7 ± 1.8
2800	133.6 ± 1.7	12.5 ± 1.6

5.3 Effect of Annealing

Heating the samples after coating showed desirable effects in two ways:

- **Evaporation of excess liquids**:

  Although the last step of spin-coating process was a high-speed spinning to dry the sample, it was found to be insufficient. Keeping the samples in an oven at 80°C facilitated the evaporation of remaining solvents after spinning or passivating in liquids.

- **Sintering:**

  Another step of heating at temperatures higher than 100°C was found to substantially improve the mechanical properties. This step, also named as annealing, was preformed in tube furnace after each spin-coating. Injecting thermal energy helps the surface atoms of the nanoparticles and substrates activate and make stronger bonds. Some unwanted events may also happen, such as penetration of particles into the substrates and oxidation.

Figure 5.10 is an SEM image of silver nanoparticles of type 2 coated on a copper substrate and annealed at 200°C for 30 min under atmosphere pressure. The tube furnace was kept at the adjusted temperature for 30 min before putting the sample to reach to the stable conditions. No purging with N_2 flow was performed. Comparing with figure 4.8 which shows the same type of particles without annealing, one can observe that after annealing the particles have some inter-connections between them which enhance mechanical properties of coating layer.

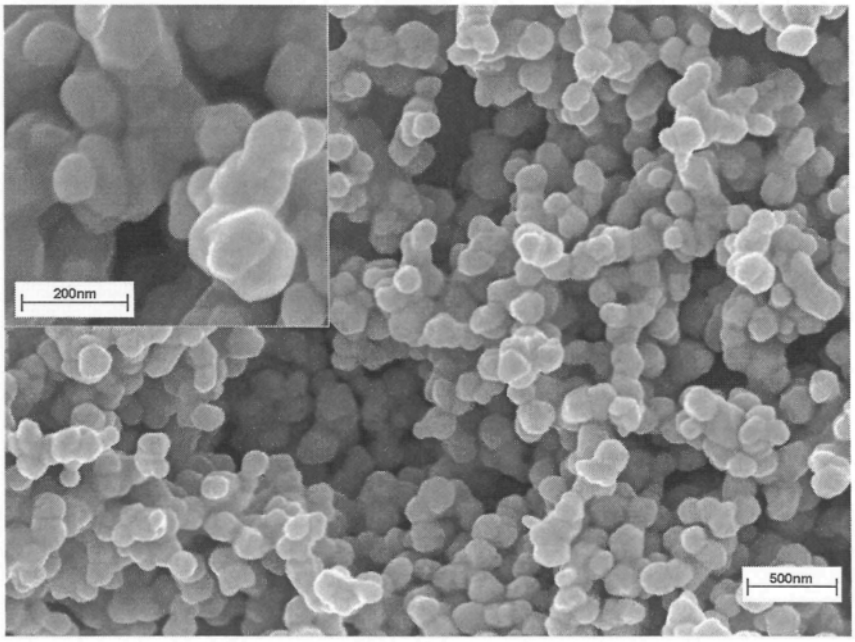

Figure 5.10: the effect of annealing at 200°C for 30 min on silver nanoparticles, in two different magnifications.

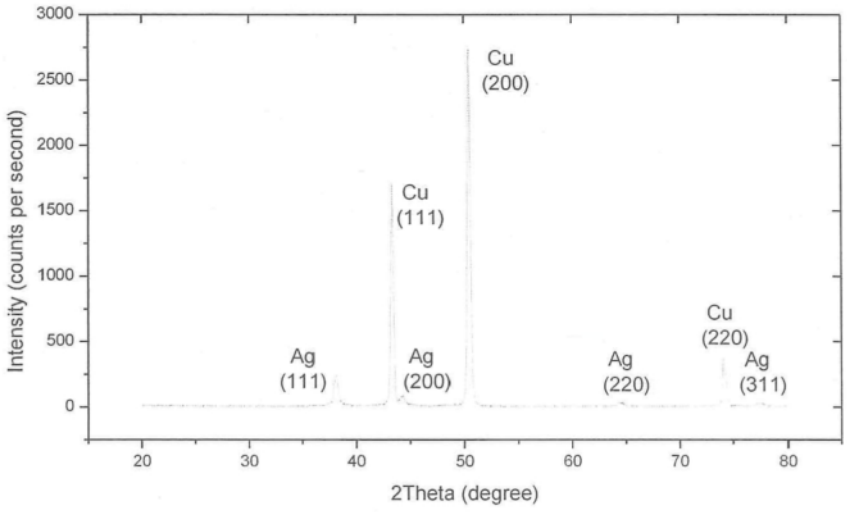

Figure 5.11 : XRD pattern of the Ag nanoparticles on copper substrate.

After coating, it was essential to know about the content of the obtained thin film and effect of coating parameters. X-ray diffraction can provide some information of chemical composition and crystal structure of solid materials. An XRD experiment was performed to identify the elements in a copper substrate coated with silver nanoparticles and annealed. The XRD pattern was recorded by a diffractometer using Cu K_α radiation (λ = 1.540 Å) in 2θ varying from 20° to 80° and is shown in figure 5.11. It suggests that silver exists purely in a fcc (face-centered cubic) structure. The four peaks detected for the silver nanoparticles were assigned to diffraction from the (111), (200), (220) and (311) planes of fcc silver, respectively. Also there are three peaks which belong to the (111), (200) and (220) planes of fcc cupper substrate. Another important outcome of this test is lack of peakes related to crystalline silver oxides. Comparing with reported XRD patterns of Ag and Ag_2O, for example in [199], one can deduce that the amount of crystalline silver oxide is less than the XRD detection level.

Figure 5.12 shows the measured water contact angles versus annealing temperature, for the copper samples covered with one layer of silver nanoparticles of type 2, annealed for 20 min, and then passivated with stearic acid. A monotonic decrease in contact angle showed that the morphology of coating was highly temperature dependent. We know that the bonding between stearic acid and metal film highly depends on the oxidation level [197]. Following the outcome of figure 5.11, a negligible change in chemical composition of coating during annealing, the quality of passivation layer was similar in the samples of

figure 5.12. Therefore, the sharp reduction of contact angle at higher annealing temperatures was due to change in the roughness of coating.

Table 5.5: The values shown in Figure 5.12.

Annealing temperature (°C)	CA (deg.)
100	136.3 ± 2.1
200	136.1 ± 1.8
250	134.3 ± 1.6
300	129.9 ± 1.7
400	117.9 ± 1.9
500	94.7 ± 1.8

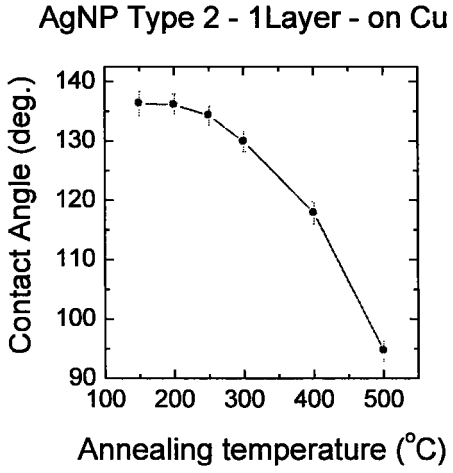

Figure 5.12: Variation of water CA versus annealing temperature for one layer coating of Ag nanoparticles of type 2, coated on copper, and passivated with SA.

Table 5.6: The values shown in Figure 5.13.

Annealing time (min)	CA (deg.)
10	141.4 ± 2.2
15	139.7 ± 2.1
25	136.1 ± 1.8
40	132.7 ± 1.7
60	130.2 ± 1.7

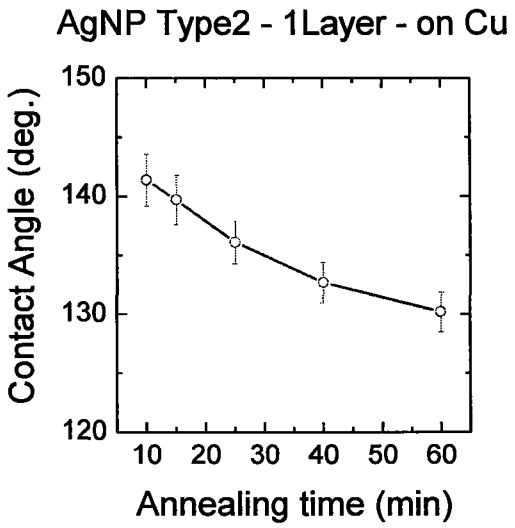

Figure 5.13: Variation of water CA versus annealing time for one layer coating of Ag nanoparticles of type 2, coated on copper, and passivated with SA.

Figure 5.13 depicts the variation of water contact angle versus annealing time, related to a set of copper samples covered with silver nanoparticles of type 2, and annealed at 200°C and finally passivated by SA. Again a monotonic reduction was detected in measured contact angle: It decreases from 141.4° to 130.2° by increasing the annealing time from 10 to 60 min. To justify this observation the following experiment was arranged.

To have a direct evidence of morphology change versus annealing time, a set of coatings on silicon substrate was studied by AFM and was presented in figure 5.14. Figure 5.14a shows the AFM image of as-deposited sample (2 layers) where the subsequent images depict the surface morphology of the samples annealed for 10, 40 and 60min. These images reveal a decrement in number of particles as well as an increment in particles sizes. A sharp increase in particles size was observed when the film has been annealed for 60

minutes. Largely, the AFM study confirms that particle size grows as a function of annealing time. It can be seen that the nearby particles agglomerate and form the larger particles. Having a constant amount of silver and wider particles means smoother surface. This agglomeration process clearly affects the morphology of the surface towards lower roughness and lower contact angles. These results are compatible with [200].

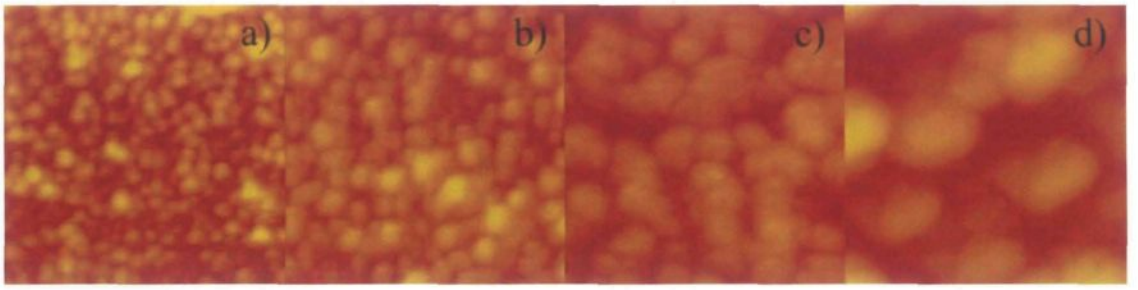

Figure 5.14: AFM images of samples annealed at 300°C for different times with a scan size of 1 μm: (a) as-deposited, (b) 10 min, (c) 40 min, and (d) 60 min.

5.4 Effect of Multi-layer Coating

Figure 5.15 shows the morphology of a silicon substrate covered with silver nano-particles of type 1. Silicon substrates are selected for AFM studies. The smoothness of substrate helped to detect the nanoparticles in AFM images. The solid weight percentage of injected colloid for this sample was 5%. The sample was dried at 80°C without being annealed. It is evident that the entire substrate surface is not covered with particles and the covered area is less than 10%. The cross section profile reveals comparable values of height and width for each particle, considering that AFM tip can not detect the hidden areas from top-view point. This indicates that the particles are settled on the surface without being

embedded. Using this relatively smooth morphology is not possible to have large contact angles.

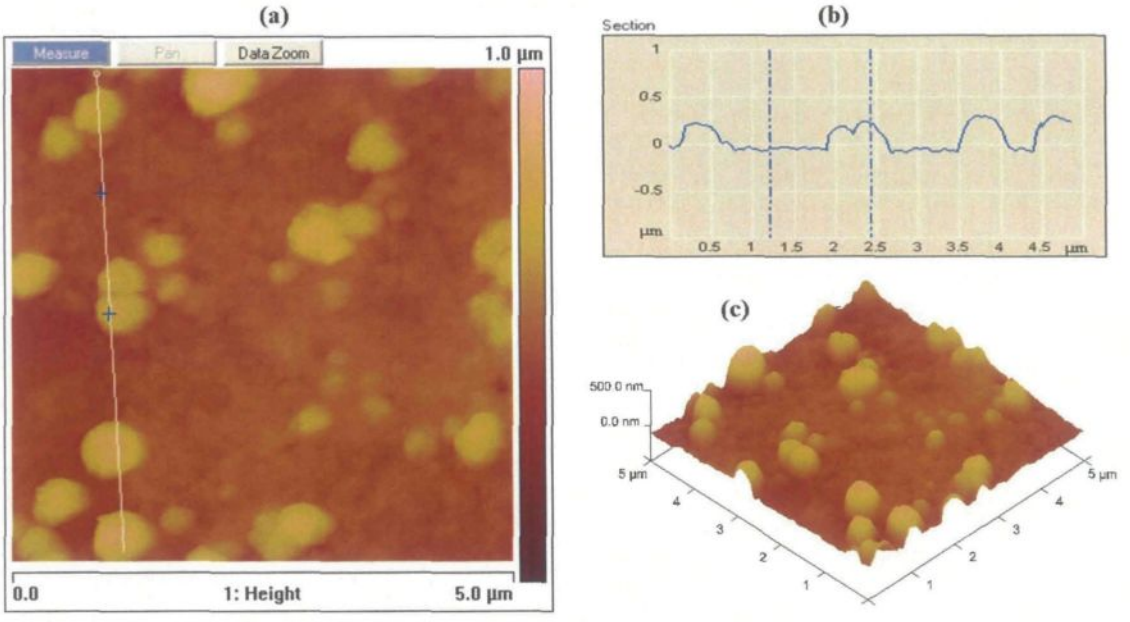

Figure 5.15: AFM images of a silicon substrate coated with one layer of silver nanoparticles of type 1: (a) 2D image, (b) vertical cross section along white line in (a), and (c) 3D image.

In figure 5.16 the morphology of a silicon substrate coated with silver nanoparticles of type 2 is depicted. The weight percentage of solid in the injected colloid was increased to 10% for this sample while all other parameters were kept constant (liquid composition, spin coating parameters and drying). Again, the entire surface is not covered by nanoparticles and some empty places are evident which water drop can be pinned in contact angle measurements. The covered area is approximately 75%. In cross section graph and 2D image it is observed that the particles are not distributed in one layer, however there are agglomerations of particles that reach to more than 500nm in height.

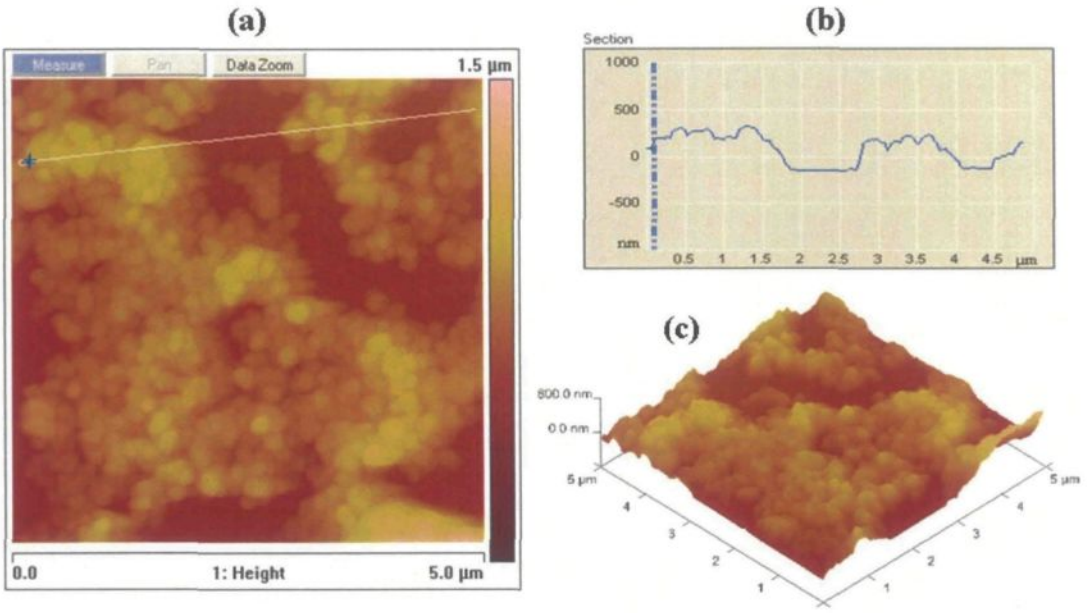

Figure 5.16: AFM images of a silicon substrate coated with one layer of silver nanoparticles of type 2: (a) 2D image, (b) vertical cross section along white line in (a), and (c) 3D image.

Figure 5.17 illustrates the AFM images of the morphology of a silicon substrate coated with silver nanoparticles of type 3 with weight percentage of solid equal to 10%. Clearly, the amount of agglomerated particles is lower compared with previous case. Also, the covered area is around 60%. During contact angle measurements, the pinning of water drop to the surface was detected all over the sample.

A complete coverage of the substrates is required to have an equal degree of roughness and uniform wetting properties for the entire surface. Increasing the weight percentage of solid in the colloid to 15% was tested and no clear difference was detected. Also, higher percentage of solid could result in unwanted agglomeration of nanoparticles and presence of millimetre-size aggregations during waiting. More practical approach is using multi-layer coatings.

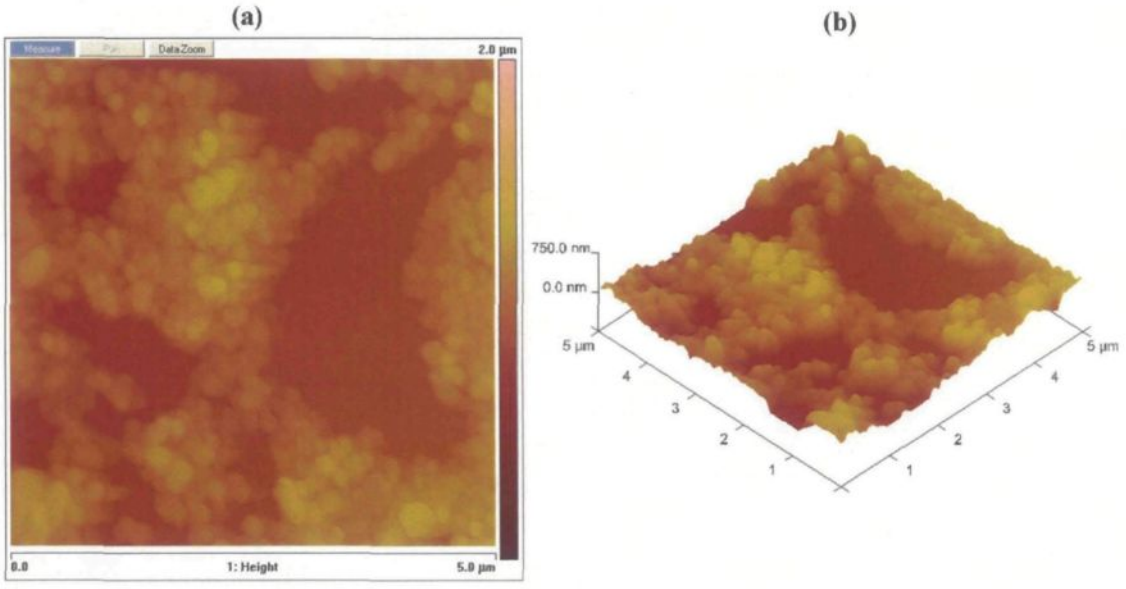

Figure 5.17: AFM images of a silicon substrate coated with one layer of silver nanoparticles of type 3: (a) 2D image, and (b) 3D image.

Figure 5.18 shows the effect of multi-layer coating on UV-vis spectra. The clean glass substrates were coated by silver nanoparticles of type 2 in one and four layers. These curves showed that multilayer coating increased the number of particles on the surface. There is also a considerable increment in the peak at 358 nm after multilayer coating. It is related to quadrupole plasmon resonance [201] while the original peak at 456nm belongs to dipole resonance. Excitation of quadrupole and higher multipole plasmon resonances in the UV-vis range can happen from larger particle sizes or agglomerations of them as they have electrical connections [201]. The latter case is more probable in the present coatings.

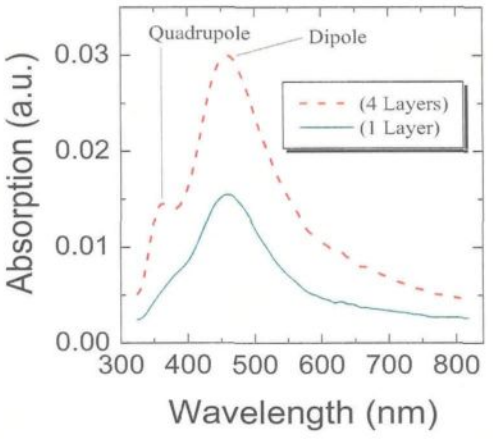

Figure 5.18 : UV-visible absorption spectra of glass substrates coated by silver particles of type 2, in 1 and 4 layers.

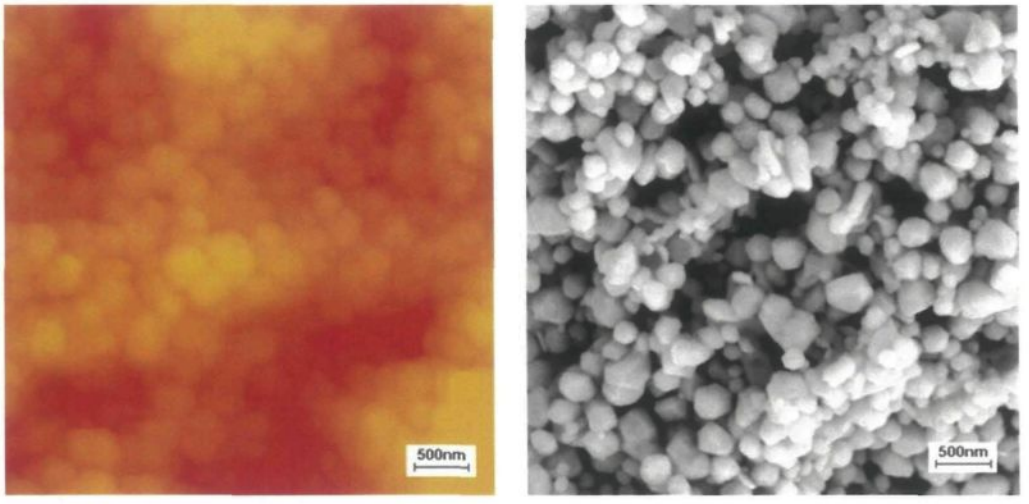

Figure 5.19 : AFM (left) and SEM (right) images of the morphology of silver nanoparticles of type 2, coated on copper substrate, in two layers.

In preparation of multi-layer coatings, it is essential that the coating process of upper layers do not affect the layers underneath. For this reason, a process of annealing at 200°C

for 30 min was performed prior to second layer of coating. Figure 5.19 depicts two SEM and AFM images with similar magnifications taken of a copper substrate coated with two layers of silver nanoparticles of type 2 (not annealed after coating of second layer). The particles sizes and morphologies are comparable in AFM and SEM images.

Figure 5.20 shows two SEM images of silver nanoparticles types 1 and 2 with similar magnifications. The difference in particles sizes and morphologies are evident. For the case of type 2 it is possible to find some nanorods as well, but their concentration is very low. In addition the presence of nanorods can not deteriorate the hydrophobicity properties of the model surfaces prepared by them. In fact many superhydrophobic surfaces are reported using nanorods to roughen the surfaces.

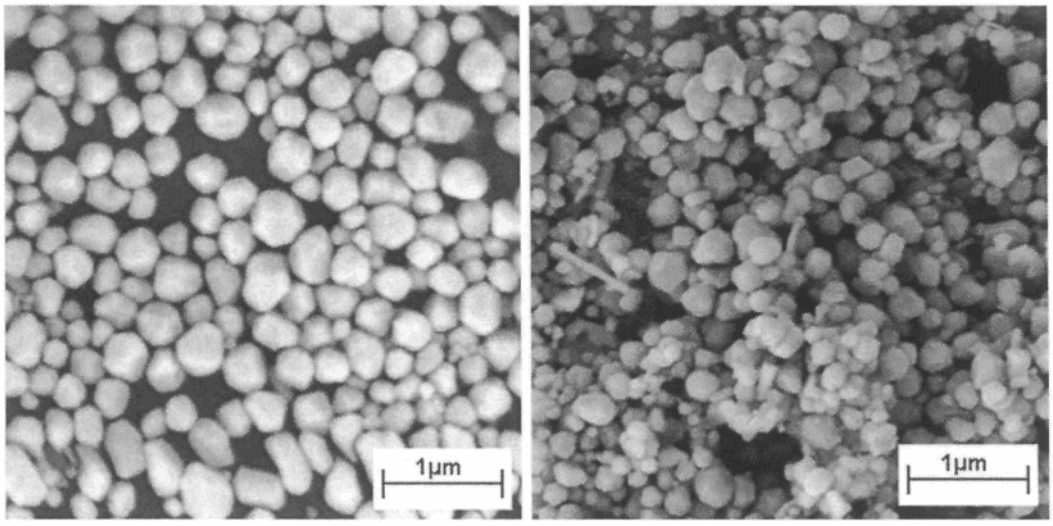

Figure 5.20: SEM (right) images of silver nanoparticles of type 1 (left) and type 2 (right) in a similar magnification scale (before annealing).

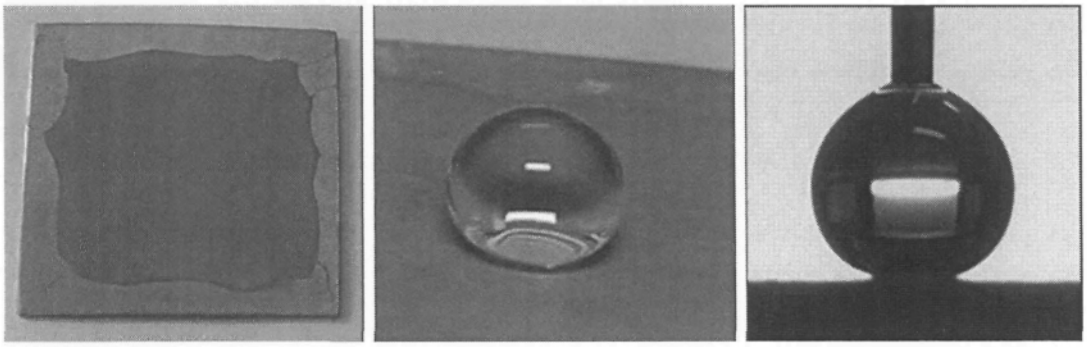

Figure 5.21: Images of a sample with silver nanoparticles of type 2 and photographs of water drops on those surfaces taken by a digital camera or by the CA goniometer built-in camera.

In table 5.7 the measured water contact angle and hysteresis for three different substrates, three types of silver nanoparticles and two passivating material are gathered. Substrates of copper, aluminum and silicon were used. Each table is related to one type of silver nanoparticles. The passivating materials were stearic acid and Zonyl 8740, dissolved in acetone and methanol, respectively.

In figure 5.22, the systematic variations of measured water contact angle and hysteresis versus number of coating layers are presented. On all the samples with one layer of coating water drops were detected to be sticky, regardless of nanoparticles type or passivating material. This observation is compatible with AFM images showing the partial coverage of substrates by nanoparticles. Water could reach the substrate and pinning was occurred which reflected in not very high contact angles and high hystereses. This is the common behaviour of Wenzel wetting regime.

Table 5.7: Water CA and CAH for different substrates coated with one, two, or three layers of various particles types, and passivated with stearic acid or Zonyl 8740.

Silver Nano-particles	Substrate Material	Layer(s)	Passivated with Stearic Acid (2mM)		Passivated with Zonyl 8740 (10%)	
			CA (°)	CAH (°)	CA (°)	CAH (°)
Type 1	Cu	1	137.2 ± 1.9	13.5 ± 1.9	137.7 ± 1.8	14.8 ± 1.9
		2	153.2 ± 1.6	7.6 ± 1.6	153.5 ± 1.3	8.9 ± 1.7
		3	153.5 ± 2.0	7.7 ± 1.3	153.7 ± 1.4	9.1 ± 1.4
	Al	1	135.3 ± 1.7	15.4 ± 1.9	135.5 ± 1.6	16.5 ± 1.8
		2	151.1 ± 1.1	9.1 ± 1.8	151.1 ± 1.3	9.8 ± 1.7
		3	152.2 ± 1.6	9.7 ± 2.0	152.3 ± 1.5	10.1 ± 1.7
	Si	1	130.4 ± 1.8	19.8 ± 2.1	131.0 ± 2.0	21.1 ± 2.0
		2	147.3 ± 1.7	10.2 ± 1.8	147.6 ± 1.8	12.5 ± 1.6
		3	148.2 ± 1.8	11.9 ± 1.9	148.4 ± 1.8	12.9 ± 1.5
Type 2	Cu	1	139.1 ± 1.6	12.7 ± 1.8	141.1 ± 1.6	13.9 ± 1.6
		2	153.9 ± 1.1	6.1 ± 1.2	154.9 ± 1.4	8.3 ± 1.4
		3	153.9 ± 1.8	7.1 ± 1.2	155.1 ± 1.8	8.9 ± 1.2
	Al	1	132.9 ± 1.9	13.4 ± 1.9	136.4 ± 1.6	17.8 ± 1.4
		2	152.5 ± 1.3	7.1 ± 1.8	152.8 ± 1.4	9.7 ± 1.4
		3	152.9 ± 2.1	12.7 ± 2.2	153.1 ± 1.2	9.9 ± 1.6
	Si	1	132.0 ± 2.0	17.8 ± 2.1	137.4 ± 1.9	18.1 ± 1.8
		2	148.6 ± 1.7	11.2 ± 1.5	149.5 ± 1.6	12.5 ± 1.5
		3	148.9 ± 1.9	12.5± 1.5	150.0 ± 2.2	14.4 ± 1.6
Type 3	Cu	1	139.8 ± 1.4	13.7 ± 1.9	140.2 ± 1.5	14.9 ± 1.9
		2	153.7 ± 1.2	6.6 ± 1.8	154.1 ± 1.5	8.8 ± 1.7
		3	153.4 ± 1.5	8.1± 1.9	154.2 ± 1.6	9.2 ± 1.5
	Al	1	131.3 ± 1.6	14.4 ± 2.1	132.4 ± 1.4	18.3 ± 1.5
		2	152.3 ± 1.6	8.8 ± 1.7	152.5 ± 1.4	9.8 ± 1.8
		3	152.6 ± 1.8	10.7 ± 2.2	152.9 ± 1.2	10.9 ± 1.7
	Si	1	136.9 ± 2.2	18.1 ± 2.1	137.0 ± 1.5	19.2 ± 2.2
		2	147.2 ± 1.7	12.8 ± 1.8	148.3 ± 1.5	13.7 ± 1.6
		3	148.1 ± 1.9	13.9 ± 1.9	148.9 ± 2.0	14.2 ± 1.8

Silver nanoparticles Type 1	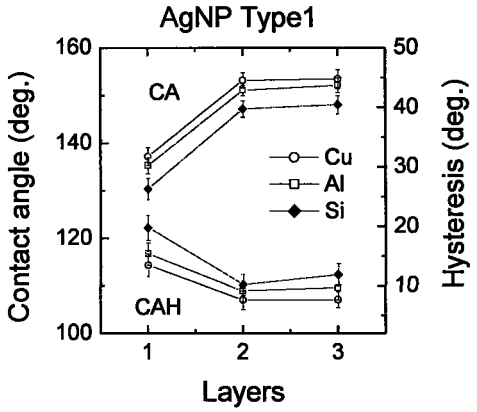
Silver nanoparticles Type 2	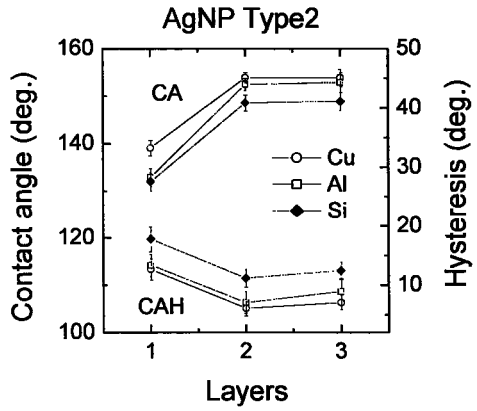
Silver nanoparticles Type 3	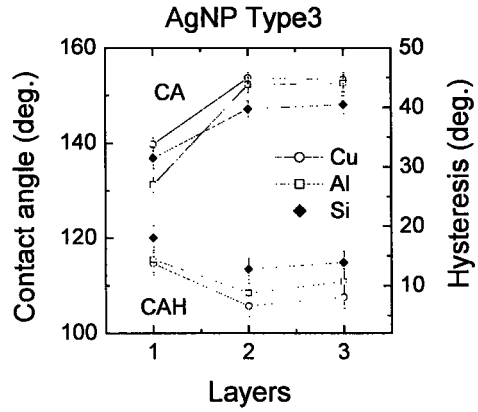

Figure 5.22: Variation of water CA versus number layers, for the samples passivated with SA.

For all the three types of nanoparticles and all the substrates, adding a second layer of coating increased the contact angle to superhydrophobic region (CA>150°) and resulted in 10° change in the hysteresis (or even more). . The water drops could roll off easily on the surface with slight inclination angles. This is the property of the Cassie-Baxter regime of wetting. The wetting behaviour remains same on the surfaces coated with a second layer of the metallic nanostructures, which could be due to no change in the surface roughness after second layer coating. The third layer of coating had no substantial effect on contact angle and an adverse effect on hysteresis. The roughness might have changed to a lower value in this case which leads to a higher CAH. Also say, in case of different substrates, the CAs obtained are different possibly due to different bonding nature of the metallic nanoparticles with different substrates.

Generally, the contact angles for copper substrates were higher than other substrates. On copper substrates, third layer resulted in slightly lower contact angle (compared with two layers) but this was not the case for aluminum and silicon substrates. In all the experiments, the measured hysteresis was found to be increasing from two layers to three layers. From all these observations, the two layer coating was found to be appropriate to the experiments of next chapter.

5.5 Effect of Passivation after Coating

Two sets of copper and aluminum substrates were coated with two layers of silver particles of type 2, annealed at 200°C for 30 min, and then passivated exactly similar to the case of figure 5.6. According to previous sections, it is believed that the surfaces of all

substrates were covered completely so the outermost surfaces were from silver. The measured water contact angles are presented in figure 5.23.

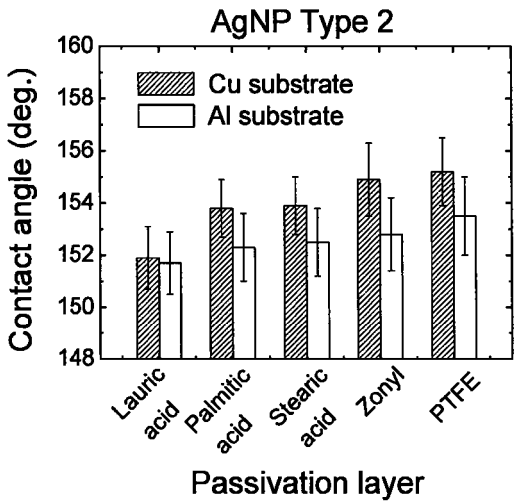

Figure 5.23: Variation of water CA versus different passivating substance for two layer coating of Ag nanoparticles of type 2, coated on copper or aluminum.

Table 5.8: The values shown in Figure 5.23

Passivating substance	CA (deg.)	
	Cu	Al
Lauric acid	151.9 ± 1.2	151.7 ± 1.2
Palmitic acid	153.8 ± 1.1	152.3 ± 1.3
Stearic acid	153.9 ± 1.1	152.5 ± 1.3
Zonyl 8740	154.9 ± 1.4	152.8 ± 1.4
PTFE	155.2 ± 1.3	153.5 ± 1.5

All the contact angles are in superhydrophobic range, and it is mainly due to roughness. In all the cases, copper-based samples showed higher contact angles compared with their aluminum-based counterparts. In fatty acids, longer chain length led to higher contact

angles but the difference between palmitic acid and stearic acid was less than the normal error of our measurement method. The fluorine content in Zonyl 8740 and PTFE reflected in higher contact angles than fatty acids. Stearic acid, Zonyl 8740 and PTFE were selected as main passivating substances for the samples used in icing experiments of next chapter.

5.6 Effect of Particle Size

Figures 5.24 and 5.25 are two sets of graphs indicating the variation of water contact angle and hysteresis versus the size of applied silver particles. In all the experiments, each sample was coated with two layers of nanoparticles, annealed after each coating, and passivated with stearic acid (figure 5.24) or with Zonyl 8740 (figure 5.25). Recalling from chapter 4, nanoparticles of type 1 to 3 were found to have average sizes of 361, 263 and 194nm, respectively. According to the experimental results, the nanoparticles of type 2 (263 nm) resulted in higher contact angles regardless of substrate and passivation materials. Also, in many cases the particles of type 1 (361 nm) were more effective compared to the particles of type 3 (194 nm). Similarly, the samples coated with nanoparticles of type 2 had relatively lower hysteresis for the copper and aluminum substrates. On the other hand for silicon-based samples the least measured hysteresis belonged to the particles of type 3, when passivated with stearic acid. In general, the particles with 263 nm average diameter were found to be more effective in achieving superhydrophobicity and were selected for the experiments of chapter 6.

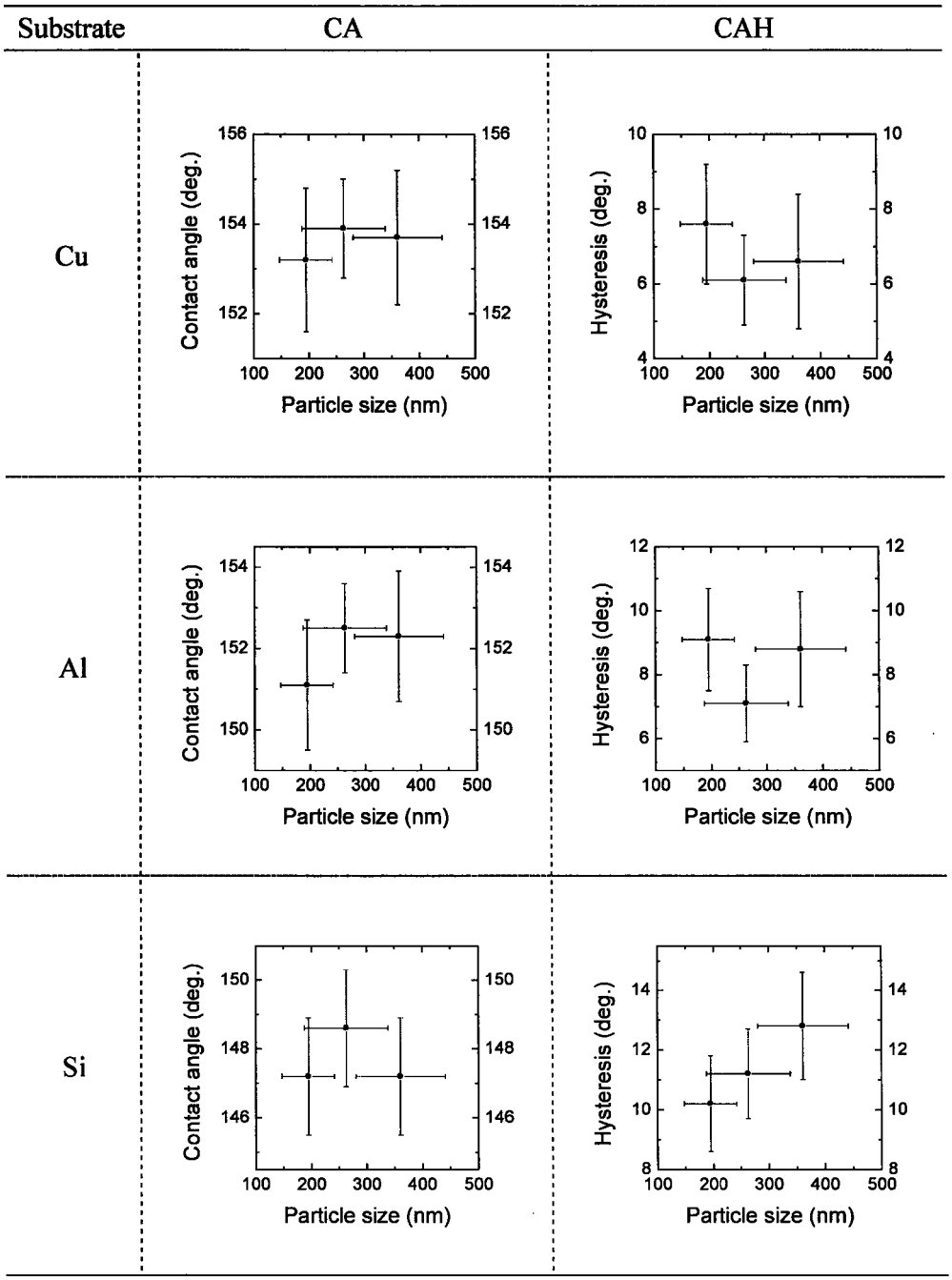

Figure 5.24: Variation of water CA and CAH versus particle size, for the samples coated with two layers and passivated with SA.

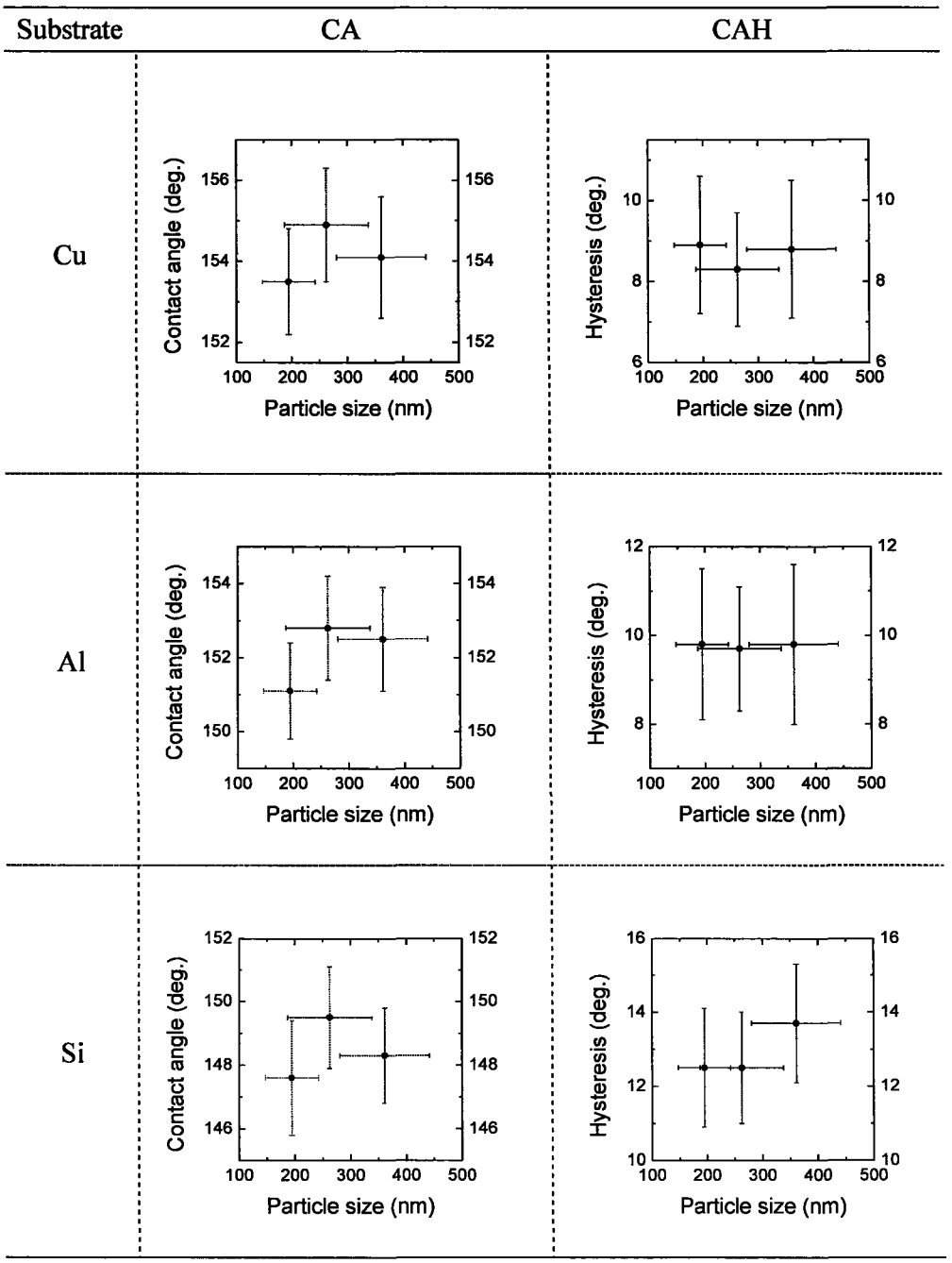

Figure 5.25: Variation of water CA and CAH versus particle size, for the samples coated with two layers and passivated with Zonyl 8740.

5.8 Stability of Superhydrophobic Samples

The stability of the passivation layers was verified by immersing them in water and some other organic solvents, i.e. ethanol, acetone and hexane, prior to performing the contact angle measurements. One set of similar samples, each with two layers coating of silver particles type 2 on aluminum substrate and passivated with Zonyl 8740 was selected and each sample was immersed for 1 h in particular solvent. Figure 5.26 shows the resulted values of water contact angle and hysteresis. As a whole, the variations of contact angle and hysteresis are found to be less than 0.6 and 0.4, respectively, after treating with either water or other organic solvents. All the variations were smaller than measurement errors and thus negligible.

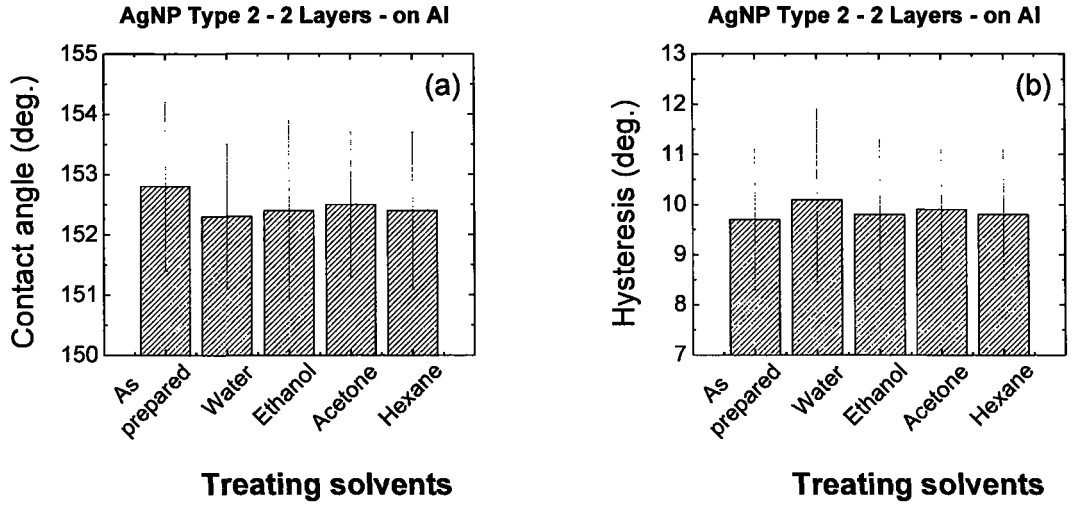

Figure 5.26: Variation of water CA and CAH after immersion in different solvents.

Figure 5.27 illustrates the variations of water contact angle and hysteresis of a sample with two layers of silver particles type 2 on aluminum and passivated with Zonyl 8740, in the period of February 2007 to December 2007. Over 11 months in laboratory environment, a 2° reduction in contact angle and less than 1° increment in hysteresis were detected, which were smaller than measurement errors and thus negligible. This is a good stability for a model sample surface.

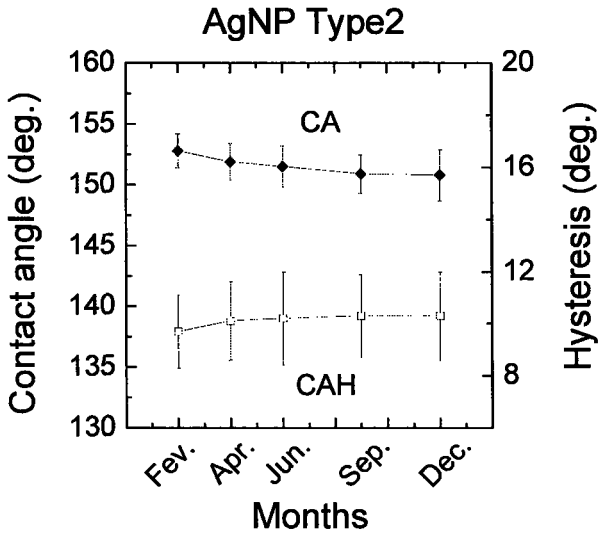

Figure 5.27: Variation of water CA and CAH over long period of time (year 2007).

5.9 Superhydrophobicity with Copper Nanoparticles.

Many experimental methods were attempted to achieve a good quality coating of copper nanoparticles on different materials. Heating when the colloid was deposited on the substrates could not help achieve a better coating. The particles were found to be very

unstable and the visible agglomerations appeared immediately, which could not remain on the surface while substrate was spinning. No stable superhydrophobic surface could be obtained on aluminum or copper substrates and resulted contact angles were always less than 150°. Regardless of difficulties in coating, the copper particles were highly unstable for this application. They were so prone to be oxidized or hydrated. The only superhydrophobic surface was achieved on silicon substrate, shown in figure 5.28. Because of high tendency of copper atoms to release one or two electrons and the absorb water molecules to be hydrated, the sample surface was turn from red (color of copper particles) to black (by oxidizing) or to green (by hydrating). Although purging the tube furnace with flow of N2 could reduce the oxidation of copper particles in annealing, but the particles could get oxidized even at room temperature. The oxidized copper could absorb water and get hydrated. The superhydrophobicity of silicon-based samples were also unstable and after some minutes water could find a path and penetrate into the coating and wet the surface. For these reasons, the copper nanoparticles were found impractical for the intention of this research.

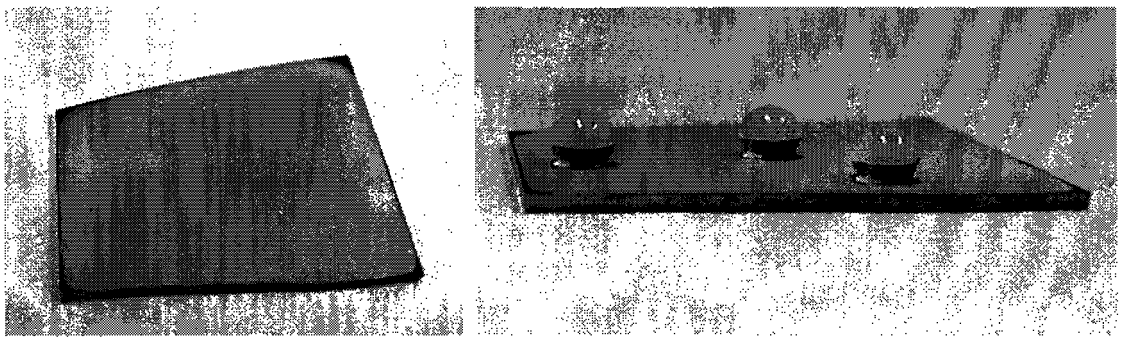

Figure 5.28: images of superhydrophobic sample prepared by deposition of Cu nanoparticles on silicon.

5.10 Summary

These general trends were distinguished:

- Water drops were sticky on all the samples with one layer of coating, regardless of type of nanoparticles. This is compatible with AFM images showing the partial coverage of substrates by nanoparticles. Water could reach the substrate and pinning was occurred.
- An increment of more than 10° was observed in water contact angle on all the samples, from one-layer to two-layer coating. None of the samples showed superhydrophobicity (CA>150°) with one layer coating but almost all could reach above 150° after being coated by second layer. The third layer of coating had no substantial effect on contact angle and adverse effect on hysteresis.
- One layer coating did not result in contact angle hysteresis less than 13° on any of samples. But a second layer could reduce its value to less than 10° and the water drops could roll off easily. This is the behaviour of the Cassie-Baxter wetting regime.
- In general higher contact angle values were achieved on the samples coated with nanoparticles of type 2, (section 3.1.3) and lower values were found for samples covered by nanoparticles of type 1 (section 3.1.2) or type 3 (section 3.1.4). Due to the relatively similar shapes of nanoparticles, it could be related to the range of the particles sizes. In other word, nanoparticles with the average size of ~263 nm resulted in the highest contact angles whereas the particles with average size of ~195 nm or ~360 nm showed lower values.

- A general trend was observed for passivation: the similar samples passivated with PTFE or Zonyl 8740 showed higher contact angle compared with those passivated with stearic acid. It can be related to the presence of fluorine in those two materials.

CHAPTER 6

RESLULTS AND DISCUSSION:

BEHAVIOUR OF SUPERHYSROPHOBIC SURFACES

UNDER ICING CONDITIONS

In this chapter the behaviour of the model superhydrophobic surfaces, developed in previous chapters, under atmospheric icing conditions are presented and discussed. The main quantitative parameters considered here are ice adhesion reduction factor (ARF) and contact angles. The calculation of ARF and its standard error is given in appendix E.

6.1 Effect of Passivation on Not-coated Surfaces

The results of ice removal test with centrifuge method (section 3.5.8) are depicted in figure 6.1. The aluminum and copper samples were passivated similarly. None of the three fatty acids used, namely lauric, palmitic and stearic acids, revealed any effect on ice adhesion. The results reported in [191] confirm a good coverage of fatty acids on aluminum (through achievement of superhydrophobicity), so it is possible to conclude that (1) the passivation layer was present and (2) it did not change the ARF effectively.

It worth mentioning that in the works of many researchers the meaning of reducing the surface energy by passivation have been expressed by hydrophobicity [202]. However, it has been found that there is no unique relation between ice adhesion strength and hydrophobicity. This is fairly compatible with what is presented in figure 6.1.

Zonyl 8740 showed a very small reduction in adhesion: ARF was equal to 1.1 on aluminum and 1.05 on copper. A few-percent reduction in ice adhesion on aluminum by Zonyl 8740 is compatible with the results in [60] and [104] when the differences in materials and coating process are taken into consideration. The other passivating material considered in chapter 5 was PTFE which is mentioned in the next section.

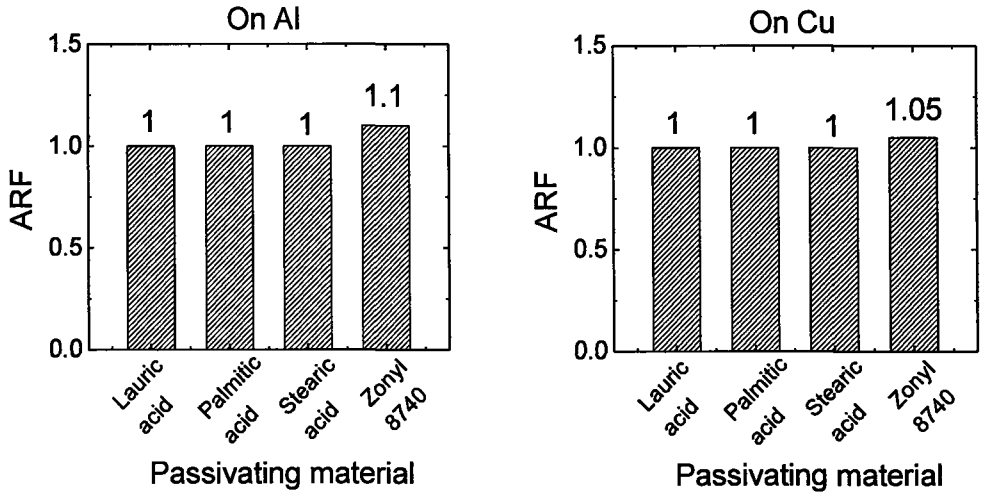

Figure 6.1: ARF for bare (not-coated with nanoparticles) aluminum (left) and copper (right) samples, passivated with lauric acid, palmitic acid, stearic acid and Zonyl 8740.

6.2 Effect of Freezing-thawing Cycles on Passivation Layer

To study the stability of passivating materials in icing conditions, a freezing-thawing experiment was arranged as follows: three similar samples with aluminum substrate and two-layer coating of silver particles type 2 were prepared and each was passivated with stearic acid, Zonyl 8740 or PTFE. After measuring the water contact angles, each sample was immersed slowly in a 100mL beaker with 20mL of de-ionized water. The beakers were placed in a freezer at -30°C to freeze completely. After two hours the beakers were brought out and kept at room temperature until the ice melted. The samples were removed from the beaker and dried in an oven at 80°C for one hour prior to contact angle measurement. These freezing-thawing cycles were repeated five times.

Figure 6.2 illustrates the variation of water contact angles for the samples passivated with stearic acid or Zonyl 8740 and figure 6.3 belongs to the sample passivated with PTFE. All the samples are in superhydrophobicity range. For the case of stearic acid, a reduction of less than 1° was detected in contact angle after the first freezing-thawing cycle and after that it remains essentially constant within the measurement error range. For Zonyl-passivated samples a minor reduction was found in contact angle as well. However, within error bars, there is no variation in the contact angles among freezing-thawing cycles and the value remains essentially constant.

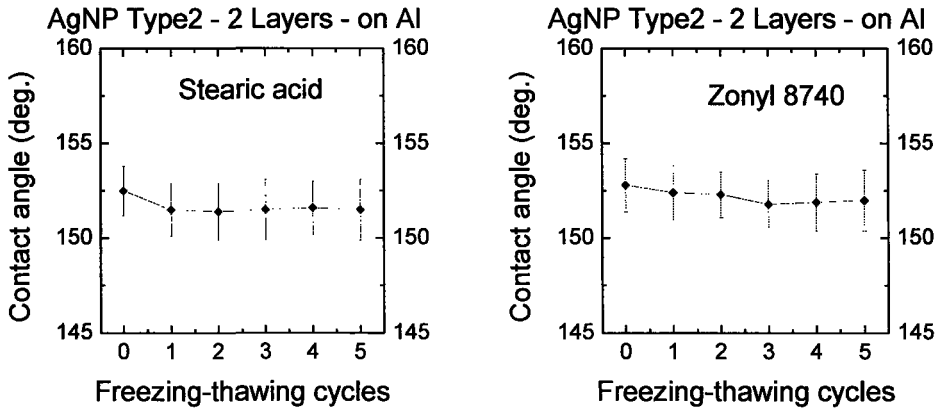

Figure 6.2 : Variation of water CA versus freezing-thawing cycles for two layer coating of Ag nanoparticles of type 2, coated on aluminum, and passivated with stearic acid or Zonyl 8740.

The behaviour of PTFE-passivated sample was found to be much different. Just after the first freezing-thawing experiment, the initial water contact angle of 153.9°±1.4° dropped to less than 150° and after fifth cycle reached 136.1°±2.8°. By repeating the passivation, it was possible to regain the initial contact angle value. This proves that the

passivation layer is not stable and in each freezing-thawing cycle a fraction of PTFE is removed. For this reason, PTFE was not suitable and not used for ice removal experiments.

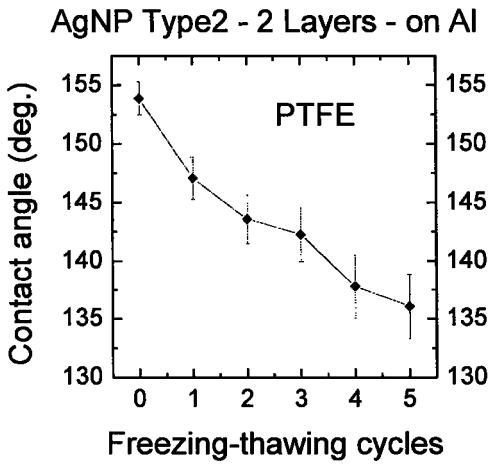

Figure 6.3 : Variation of water CA versus freezing-thawing cycles for two layer coating of Ag nanoparticles of type 2, coated on aluminum, and passivated with PTFE.

6.3 Effect of Coating

Figure 6.4 illustrates the 2D and 3D optical profilometry results for an aluminum substrate coated with one layer of silver nanoparticles type 2, without any passivation. The RMS roughness of whole surface was determined to be 191.25nm. This is a low degree of roughness compared with the reported values for other anti-icing candidate coatings, for example in [202]. Without coating, the RMS roughness was found to be ~115 nm using the optical profilometer. According to [52] one expects to have higher ice adhesion when roughness is increased and there is a higher chance of mechanical interlocking. To verify this, an ice removal experiment was performed on the sample and an ARF value of 0.9 was

obtained. An ARF less than one means higher adhesion stress and the experiment is compatible with the expected trend.

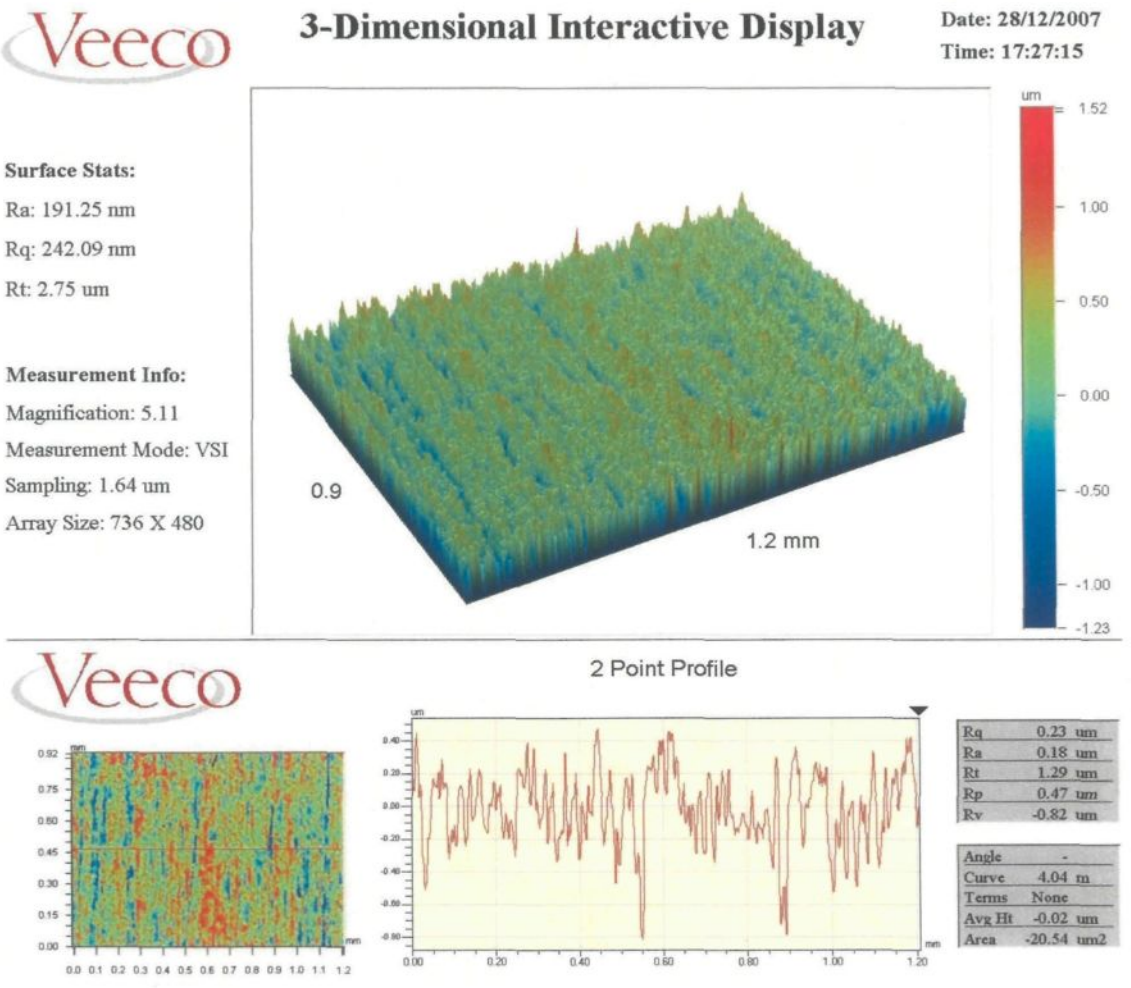

Figure 6.4: 2D and3D profiles for one-layer coating of Ag nanoparticles of type 2, covered on Al.

A similarly-prepared sample was passivated with Zonyl 8740 and was tested in an ice removal test. The result is presented in figure 6.5. The ARF of 1.6 was determined. Usually the passivation layer is thin and does not change the morphology, but in this experiment its

effect was to increase the ARF from 0.9 to 1.6. According to ARF of 1.1 for Zonyl 8740 on not-coated aluminum, one can deduce that a collective effect of both the higher roughness and lower surface energy led to the lower ice adhesion.

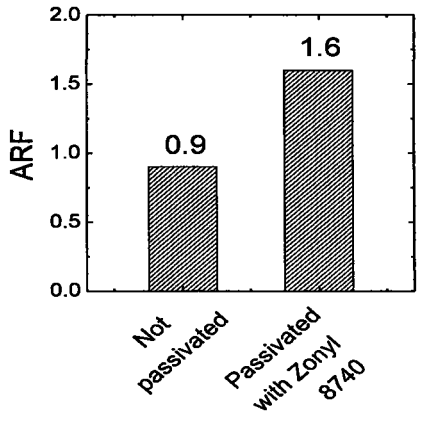

Figure 6.5: ARF for not-passivated and Zonyl-passivated samples with one-layer coating of Ag nanoparticles of type 2 on aluminum substrates.

6.4 Effect of Multi-layer Coating

Figure 6.6 shows the ARF values versus number of coating layers of silver particles of type 2 on aluminum substrates and passivated with Zonyl 8740. The behaviour of ARF is similar to what was observed in figure 5.20 for water contact angle. Adding just one layer of nanoparticles could increase the ARF from 1.6 for one layer to 8.1 for two layers. This also intensifies the main hypothesis of having low ice adhesion by lowering the wettability.

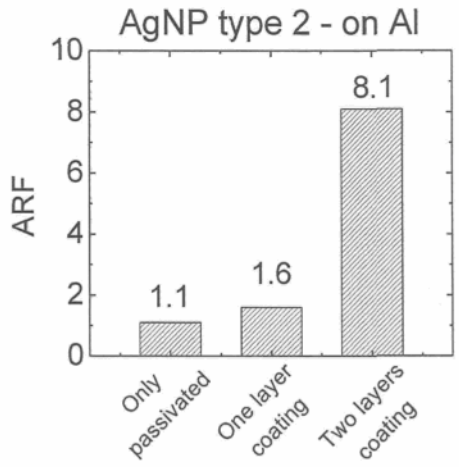

Figure 6.6: ARF for Zonyl-passivated samples with zero-, one-, and two-layer coatings of Ag nanoparticles of type 2 on aluminum substrates.

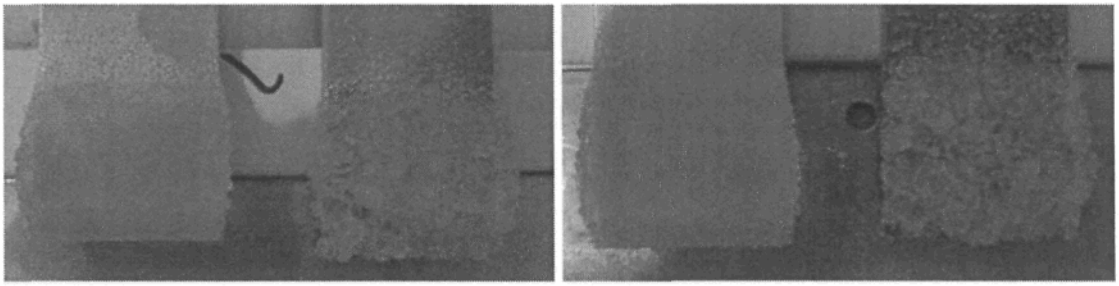

Figure 6.7: The ice accumulated on bare aluminum and on coated aluminum with (a) one layer and (b) two layers of Ag nanoparticles of type 2 and passivated with Zonyl 8740.

Figures 6.7a and 6.8a depict the ice accumulated on aluminum samples coated with one or two layers of silver nanoparticles of type 2, respectively, followed by passivation with Zonyl 8740. The ice shape is completely different on not-coated and coated samples.

6.6 Effect of Particle Size

Similar to the case of hydrophobicity, it was expected to find some relation between ice adhesion and nanoparticle sizes. Three aluminum substrates were coated with two layers of nanoparticles types 1 to 3 and then passivated with Zonyl 8740. The results are presented in figure 6.8.

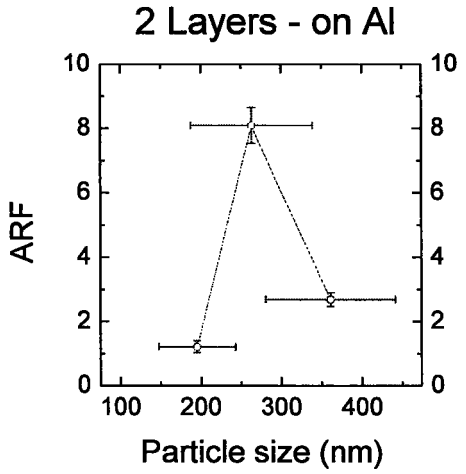

Figure 6.8: Variation of ARF versus particle size, for two layer coating of Ag nanoparticles of type 2, coated on aluminum, and passivated with Zonyl 8740.

Table 6.1: The values shown in Figure 6.8.

Particle size (nm)	ARF
195 ± 47.5	1.214 ± 0.182
263 ± 75.5	8.095 ± 0.562
361 ± 80.5	2.680 ± 0.213

Among three groups of silver nanoparticles, the larger particles of type 3 with average size of 361 nm showed an ARF of 2.68 and the smaller ones, type 1 with average size of

195 nm resulted in even smaller ARF of ~1.21. On the other hand, the medium range of particles, type 2 with average size of 263 nm revealed an ARF more than 8, which means 8 times less ice adhesion to the sample surface.

6.7 Effect of Ice Removal Repetition on Ice Adhesion

Are the ARF values found in previous sections stable? To verify the stability two samples were examined for five sequential ice removal cycles. Both the samples had aluminum substrates and Zonyl passivation, but one of the samples had a two-layer coating of silver particles type 1 and the second sample was coated with two layers of particles type 2.. After each ice removal experiment, the samples were detached from the beam and placed in an oven to dry up before contact angle measurements. The obtained ARF results are gathered in figures 6.9 and 6.10 and the measured contact angles are presented in figures 6.11 and 6.12.

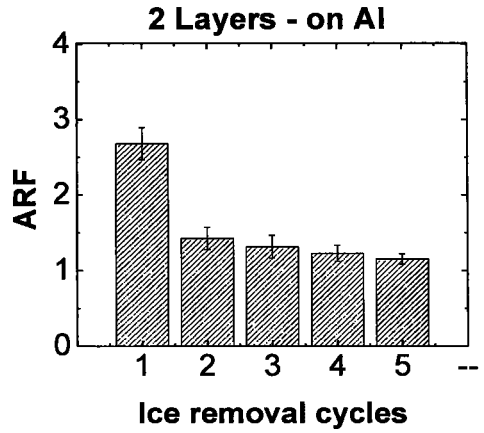

Figure 6.9 : Variation of ARF versus ice removal cycles for two layer coating of Ag nanoparticles of type 1, coated on aluminum, and passivated with Zonyl 8740.

Table 6.2: The values shown in Figure 6.9.

Ice removal cycles	ARF
1	2.680 ± 0.213
2	1.427 ± 0.149
3	1.317 ± 0.150
4	1.229 ± 0.106
5	1.155 ± 0.068

The sample with particles type 1 had an initial ARF of 2.68 which dropped to less than 1.56 after five ice removal cycles. This reducing ARF did not reach to a steady value. On the other hand, the sample made of particles type 2 reached to steady ARF value of ~1.7 after three ice removal cycles. Although the steady state ARF of 1.7 is much smaller than initial 8.1, it is the number which should be considered as effective ARF value. This experiment reveals that without repeating the ice removal test it is not possible to judge about the measured ARF value of an anti-icing candidate material.

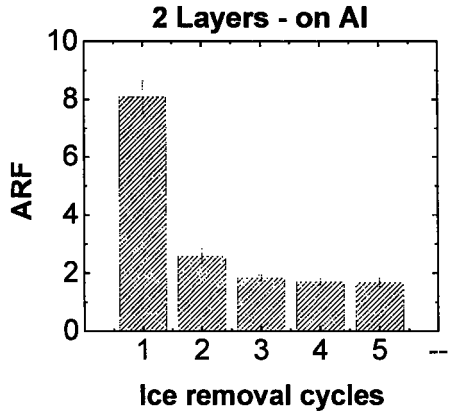

Figure 6.10 : Variation of ARF versus ice removal cycles for two layer coating of Ag nanoparticles of type 2, coated on aluminum, and passivated with Zonyl 8740.

Table 6.3: The values shown in Figure 6.10.

Ice removal cycles	ARF
1	8.095 ± 0.562
2	2.596 ± 0.257
3	1.834 ± 0.102
4	1.706 ± 0.111
5	1.685 ± 0.147

6.8 Effect of Ice Removal Repetition on Hydrophobicity

Repeating the ice removal test had some effects on wettability of the samples as well. The measured contact angles are shown in figures 6.11 and 6.12 for coating of particles type 1 and type 2 respectively.

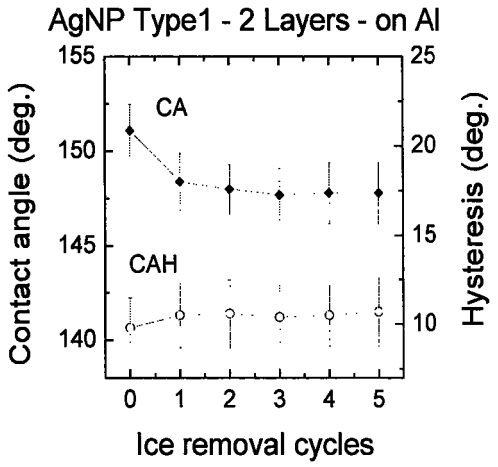

Figure 6.11 : Variation of water CA and CAH versus ice removal cycles for two layer coating of Ag nanoparticles of type 1, coated on aluminum, and passivated with Zonyl 8740.

Table 6.4: The values shown in Figure 6.11.

Ice removal cycles	CA (deg.)	CAH (deg)
0	151.1 ± 1.4	9.8 ± 1.7
1	148.4 ± 1.5	10.5 ± 1.8
2	148.0 ± 1.3	10.6 ± 1.9
3	147.7 ± 1.4	10.4 ± 1.8
4	147.8 ± 1.6	10.5 ± 1.7
5	147.8 ± 1.6	10.7 ± 1.9

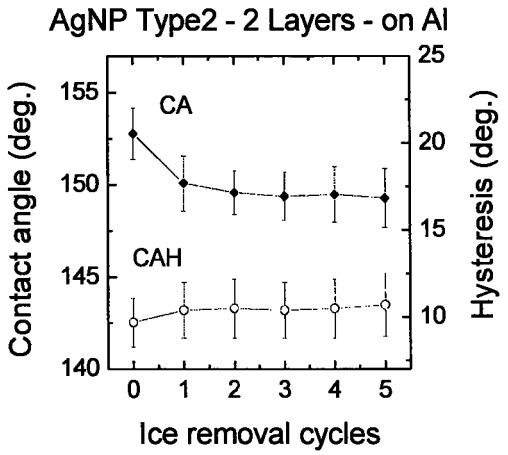

Figure 6.12 : Variation of water CA and CAH versus ice removal cycles for two layer coating of Ag nanoparticles of type 2, coated on aluminum, and passivated with Zonyl 8740.

Table 6.5: The values shown in Figure 6.12.

Ice removal cycles	CA (deg.)	CAH (deg)
0	152.8 ± 1.4	9.7 ± 1.4
1	150.1 ± 1.5	10.4 ± 1.6
2	149.6 ± 1.2	10.5 ± 1.7
3	149.4 ± 1.3	10.4 ± 1.6
4	149.5 ± 1.5	10.5 ± 1.7
5	149.3 ± 1.6	10.7 ± 1.8

For both samples, the contact angle reduced and the hysteresis increased. This could be due to loss of coating and/or loss of passivation. If the coating was lost, the newly exposed surface did not have a passivating layer. Assuming that, a pinning of water in those not-passivated areas would happen so that one could expect a substantial decrement in contact angle and sharp increment in hysteresis which was not the case. To clarify the kind off loss the samples were repassivated and the contact angles were measured. The obtained values showed that deteriorating of hydrophobicity was mainly from loss of passivation and not from loss of coating.

6.9 Effect of Substrate Material

The effect of substrate material was examined by repeating the experiment of figures 6.10 and 6.12 but using copper substrates. The sample had two layer coatings of silver particles of type 2 and a passivation of Zonyl 8740. The measured results of ARF and contact angle are illustrated in figures 6.13 and 6.14 respectively.

Two major noticeable issues were observed in the case of copper. The first issue was a much smaller drop in ARF by repetition of ice removal, from ~4 in first test to ~2.5 in fifth test while it was 8.1 to 1.68 in the case of aluminum. Another observation was persistence of contact angle in superhydrophobic range even after five ice removal cycle. This may be related to different reactions at the interface of silver/copper compared to silver/aluminum. In [200] we showed a partial penetration of silver nanoparticles into copper substrates

leading to a higher adhesion. This can explain the less drop of ARF by repetition of ice removal cycles.

Table 6.6: The values shown in Figure 6.13.

Ice removal cycles	ARF
1	4.011 ± 0.315
2	2.827 ± 0.215
3	2.644 ± 0.27
4	2.553 ± 0.187
5	2.508 ± 0.191

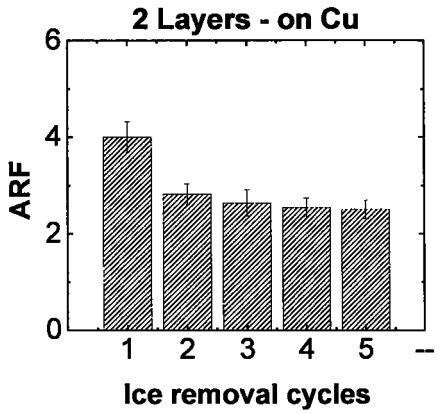

Figure 6.13 : Variation of ARF versus ice removal cycles for two layer coating of Ag nanoparticles of type 2, coated on copper, and passivated with Zonyl 8740.

Table 6.7: The values shown in Figure 6.14.

Ice removal cycles	CA (deg.)	CAH (deg)
0	154.9 ± 1.4	8.3 ± 1.7
1	152.1 ± 1.5	8.9 ± 1.8
2	151.7 ± 1.3	9.0 ± 1.9
3	151.8 ± 1.4	9.1 ± 1.8
4	151.5 ± 1.6	8.9 ± 1.7
5	151.6 ± 1.6	9.2 ± 1.9

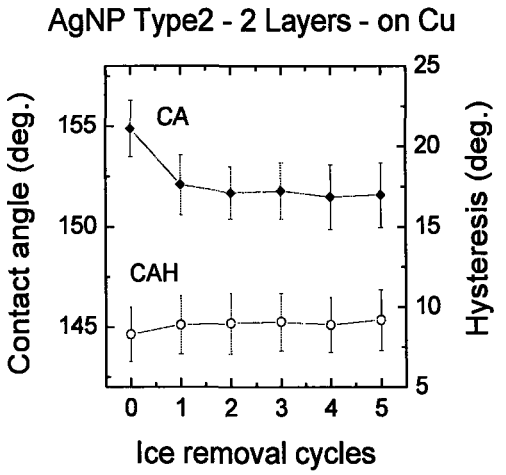

Figure 6.14 : Variation of water CA and CAH versus ice removal cycles for two layer coating of Ag nanoparticles of type 2, coated on copper, and passivated with Zonyl 8740.

6.10 The Freezing-thawing of Macroscopic Drops

All the previous experiments were dealing with supercooled droplets in the range of 10-100μm in diameter. One experiment was performed to study the freezing of millimetre size water drop on one of the model surface of this research. A copper -based sample with two layer coating of silver particles type 2 and passivated with Zonyl 8740 was inside the Peltier chamber described in section 3.5.7. Initially, when the sample was at room temperature, the contact angle of a water drop of ~6 μL was measured as ~151° at room temperature. On freezing, this contact angle of the drop decreased to 136.7°. The shape evolution happened very fast because of rapid freezing by high heat flow rate of Peltier element and small mass of water drop. Figure 6.15 depicts the drop shape before and after freezing. After increasing the set point of controller to room temperature the contact angle

increased slightly to ~138°. After removing the droplet and blowing the sample with flow of N_2, the entire sample surface was superhydrophobic with low hysteresis, but the droplet spot had lower contact angle and very high hysteresis. Only after keeping the sample in a oven at 80° for more than two hours the spot regained its original behaviour. From this experiment one can conclude: Before experiment and when the sample was at room temperature the wetting regime was Cassie-Baxter regime. During the freezing of macroscopic drop, some of water molecules penetrated the pores underneath the droplet and a fraction of pores near the water were filled, at least partially. Even after thawing and blowing the sample these water molecules remained in the pores and caused Wenzel regime for the area of the spot. By keeping the sample in the oven, these molecules could get enough energy to escape from the pores and wetting returned to Cassie-Baxter regime. This experiment also shows that the behaviour of superhydrophobic samples during freezing is dependent on the size of droplet and the way it is placed on the surface.

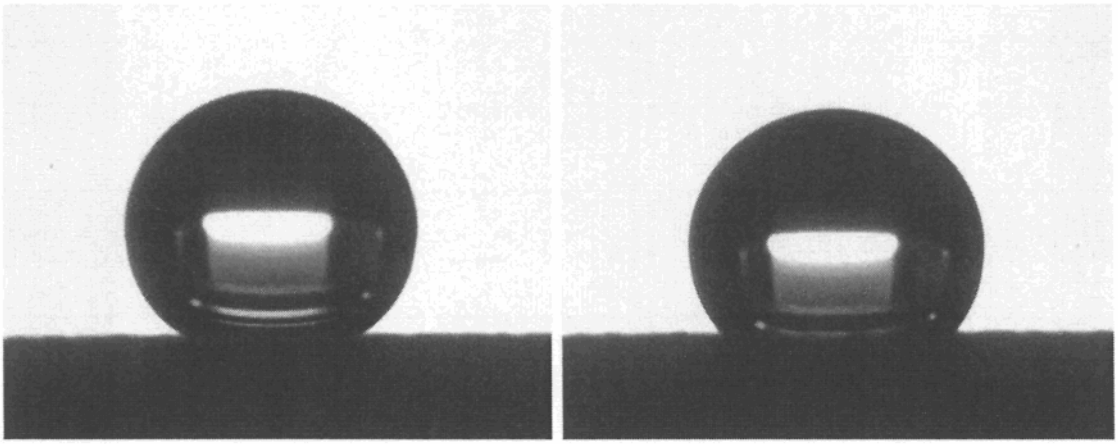

Figure 6.15: A water droplet on a superhydrophobic surface before (left) and after (right) freezing.

6.11 Summary

Several tests were conducted to study the behaviour of model superhydrophobic surfaces in atmospheric icing conditions. The different aspects of the surfaces and of the silver nanoparticles were taken into consideration. It was possible to study the effect of icing on wettability parameters. From the results obtained, the following conclusions can be drawn:

- Both on aluminum and copper substrates, performing the passivation with fatty acids did not change the ice adhesion. Also the effect of passivation with Zonyl 8740 on ice adhesion was very small.
- Stearic acid and Zonyl 8740 showed relatively stable in subsequent freezing-thawing cycles compared with PTFE.
- By covering the substrates with only one layer of nanoparticles of any type could not provide an ARF greater than 1.6. However by adding a second layer, it could be as large as 8.1
- Two layers coating of the silver nanoparticles with the average size of ~263 nm led to the highest ARF of 8.1 whereas the particles with average size of ~195 nm or ~360 nm showed lower ARF values of 1.21 and 2.68 respectively.
- By repeating the ice removal test for five times, ARF values reduced from 8.1 to 1.69 on aluminum and from 4 to 2.5 on copper.

CHAPTER 7

CONCLUSIONS AND RECOMMENDATIONS

7.1 Concluding Remarks

The current research was mainly dealing with developing a new superhydrophobic coating, based on metallic nanoparticles, to be used as an anti-icing agent. There are several process parameters that directly affect the final surface structure and the reduction of ice adhesion of surface. We did not aim at studying the entire range of all the parameters involved and their interaction but intended to demonstrate the possibility of preparing artificial superhydrophobic surfaces which can provide efficient anti-icing protection.

The present study was carried out within the framework of CIGELE/INGIVRE at UQAC, aimed at achieving a reliable model surface and obtaining a set of values for the essential parameters. For this purpose concluding remarks are divided to three parts as follows:

7.1.1 Nanoparticle Characteristics

The development of three preparation methods for silver nanoparticles and two approaches for copper nanoparticles has been addressed in this thesis. From the obtained results, the following conclusions can be drawn:

- In the case of silver, the largest particles (with average diameter of ~361 nm) were obtained by injecting precursor to alcoholic solution and the smallest ones (~195 nm) by using ascorbic acid in aqueous/alcoholic medium. Reduction of silver ions in basic medium in presence of ethylene glycol resulted in silver particles of medium size (~263 nm). The capping agent for all the reactions was PVP.

- In the case of copper, reduction of copper sulphate with ascorbic acid in alcoholic medium resulted in larger particles compared with the particles prepared in two-step process: sodium borohydrade and ascorbic acid in aqueous/alcoholic medium.
- Silver nanoparticles were essentially stable and their colloid kept their properties for more than one month. Copper particles have higher affinity to agglomerate and precipitate in the colloids and to get oxidized or hydrated when coated on the substrates. Their limited stability made them useless for this kind of applications.

7.1.2 Superhydrophobicity Characteristics

Superhydrophobicity was obtained on aluminum, copper and silicon substrates. The main trends were as follows:

- Water drops were sticky on all the samples with one layer of coating, regardless of type of nanoparticles. AFM images explained this observation, showing the partial coverage of substrates by nanoparticles. Water could reach the substrate and pinning occurred.
- Water contact angles were increased by more than 10° on all the samples, just by adding a second coating layer. None of the samples showed superhydrophobicity (CA>150°) with one layer coating but almost all could reach above 150° after being coated by second layer. The third layer of coating had no beneficial effect on water contact angle and adverse effect on hysteresis.
- One layer coating did not result in contact angle hysteresis less than 13° in any of samples. But a second layer could reduce its value to less than 10° and the water

drops could roll off easily. This is the behaviour of the Cassie-Baxter wetting regime.

- In general higher contact angle values were achieved on the samples coated with nanoparticles with the average size of ~263 nm. Both smaller particles (~195 nm) and larger ones (~360 nm) were found to have lower contact angle values.
- A general trend was observed for passivation: the similar samples passivated with PTFE or Zonyl 8740 showed higher contact angle compared with those passivated with stearic acid. This observation can be related to the presence of fluorine in the composition of this material.

7.1.3 Ice adhesion Characteristics

The developed model superhydrophobic surfaces were examined in atmospheric icing conditions. The different aspects of the samples and of the silver nanoparticles were considered precisely. We also studied the effect of icing on wettability parameters. From the results obtained, the following conclusions may be concluded:

- Performing the passivation with fatty acids did not alter the ice adhesion on aluminum and copper. The effect of passivation with Zonyl 8740 on ice adhesion was found to be very small.
- Stearic acid and Zonyl 8740 were relatively stable in subsequent freezing-thawing cycles but PTFE deteriorated.
- A maximum ARF of 1.6 was achieved by one layer coating of nanoparticles. On the other hand by adding a second layer, it could reach to 8.1

- The silver nanoparticles with the average size of ~263 nm led to the highest ARF of 8.1 whereas the particles with average size of ~195 nm or ~360 nm showed lower ARF values of 1.21 and 2.68 respectively.
- The ARF was found to vary substantially by repeating the ice removal cycle. After five cycles, ARF reduced from 8.1 to 1.69 on aluminum and from 4 to 2.5 on copper.

7.2 Future Trends

A comprehensive study was done on the effect of nanoparticles, coating parameters and passivation on adhesion of ice on these model superhydrophobic surfaces. To proceed further and fill the gap between the model surfaces prepared in this study and more economic anti-icing superhydrophobic coatings the following points can be suggested:

- It is proposed to use some hard substrates instead of metallic ones. Certain types of materials can partially embed the particles and make stronger bonding, in order to increase the coating life time.
- It is suggested to use electrically and thermally nonconductive substrates or equivalently coating a substrate with an insulating material such as diamond-like carbon coatings. In this way it would be possible to take advantage of the conductivity of the nanoparticle-based coating. By applying a DC or AC currents through the conductive coating local heat will be generated without penetrating the bulk material and can effectively melt the ice from the inevitable

solid-ice area fraction. For each icing condition, finding the best current density and frequency will be an interesting practical problem.

- It is recommended to further investigate the other chemical binders such as various Zonyl products introduced by DuPont for improved coating adherence quality.
- One important extension of this work can be through testing other coating methods which can be used on non-planar surface such as spray coating. Also nanoparticles can be added to some fluorinated paints and applied to the surface.
- It is also proposed to find more cost-effective substance instead of silver as a precursor of nanoparticles. Aluminum nanoparticles can be a choice.
- It is worth investigating other types of passivation materials with better adhesion to the nanostructured metallic thin films coatings, to increase the durability under severe icing conditions.
- Last but not the least recommendation is to investigate the stability of the sample surfaces with ice accumulation time. This experiment can provide valuable information on the durability and efficiency of the sample surfaces to withstand longer ice accumulation periods as often encountered in natural conditions.

REFERENCES

[1] M. Farzaneh, Ed., *Atmospheric Icing of Power Networks*. Berlin: Springer, 2008.

[2] M. Van Dyke, D. Havard, and A. Laneville, "Effects of Ice and Snow on the Dynamics of Transmission Line Conductors," in *Atmospheric Icing of Power Networks*, M. Farzaneh, Ed.: Springer, 2008, ch. 5, pp. 171 - 228.

[3] M. Farzaneh, "Ice and Snow Shedding," in *EPRI Transmission Line Reference Book - Wind- induced Conductor Motion.*: Electric Power Research Institute, 2006, ch. 7.4, pp. 7.19 - 25.

[4] G. Poots, *Ice and Snow Accretion on Structures.*: Research Studies Press, 1996.

[5] M. Farzaneh, "Rapport sur la Tempête de Verglas de Janvier 1998, Comite d'experts d'Hydro- Quebec (Comite Varennes)," 1998.

[6] M. Farzaneh et al., "Insulator Icing Test Methods and Procedures," *IEEE Trans. Power Delivery*, vol. 18, no. 4, pp. 1503 - 1515, 2003.

[7] M. Farzaneh et al., "Selection of Station Insulators with Respect to Ice or Snow - Part I: Technical Context and Environmental Exposure," *IEEE Trans. Power Delivery*, vol. 20, no. 1, pp. 264 - 270, 2005.

[8] M. Farzaneh et al., "Selection of Station Insulators with Respect to Ice or Snow - Part II: Methods of Selection and Options for Mitigation," *IEEE Trans. Power Delivery*, vol. 20, no. 1, pp. 271 - 277, 2005.

[9] M. Farzaneh et al., "Selection of Line Insulators With Respect to Ice and Snow - Part I: Context and Stresses," *IEEE Trans. Power Delivery*, vol. 22, no. 4, pp. 2289 - 2296, 2007.

[10] M. Farzaneh et al., "Selection of Line Insulators with Respect to Ice and Snow - Part II: Selection Methods and Mitigation Options," *IEEE Trans. Power Delivery*, vol. 22, no. 4, pp. 2297 - 2304, 2007.

[11] G. McClure, K. C. Johns, F. Knoll, and G. Pichette, "Lessons from the Ice Storm of

1998," in *International Workshop on Atmospheric Icing on Structures (IWAIS)*, Brno, Czech Republic, 2002, p. 7.

[12] M. Farzaneh, C. Volat, and A. Leblond, "Anti-icing and De-icing Techniques for Overhead Lines," in *Atmospheric Icing of Power Networks*, M. Farzaneh, Ed.: Springer, 2008, ch. 6, p. 229.

[13] B. Wejden and J. Øvstedal, "Contamination and Degradation of De-Icing Chemicals in the Unsaturated and Saturated Zones at Oslo Airport, Gardermoen, Norway," in *NATO Science Series, IV: Earth and Environmental Sciences.*: Springer, 2006, vol. 74, pp. 205 - 218.

[14] J. L. Laforte, M. A. Allaire, and J. Laflamme, "State-of-the-art on Power Line De-icing," *Atmos. Res.*, vol. 46, no. 1-2, pp. 143 - 158, 1998.

[15] Z. Peter, M. Farzaneh, and L. I Kiss, "Assessment of the Current Intensity for Preventing Ice Accretion on Overhead Conductors," *IEEE Trans. Power Delivery*, vol. 22, no. 1, pp. 565 - 574, 2007.

[16] B. Y. Yang and R. Montgomery, "De-icers Derived from Corn Steep Water," *Bioresource Technol.*, vol. 90, no. 3, pp. 265 - 273, 2003.

[17] V. F. Petrenko and S. G. Qi, "Reduction of Ice Adhesion to Stainless Steel by Ice Electrolysis," *J. Appl. Phys.*, vol. 86, no. 10, pp. 5450 - 5454, 1999.

[18] C. Laforte and A. Beisswenger, "Icephobic Material Centrifuge Adhesion Test," in *International Workshop on Atmospheric Icing on Structures (IWAIS)*, Montreal, Canada, 2005.

[19] G. H. Ahlborn and H. C. Poehlmann, "Development of a Hydrophobic Substance to Mitigate Pavement Ice Adhesion," Report EPA-600/2-76-242, 1976.

[20] W. J. Dohaney and J. D. Innes, "Ice-Free Pavement - Evaluation of a Verglimit as a De-Icing Agent," Canadian Technical Asphalt Association, 1979.

[21] V. K. Croutch and R. A. Hartley, "Adhesion of Ice to Coatings and the Performance of Ice Release Coatings.," *J. Coat. Technol.*, vol. 64, pp. 41 - 53, 1992.

[22] S. A. Kulinich and M. Farzaneh, "Alkylsilane Self-assembled Monolayers: Modeling Their Wetting Characteristics," *Appl. Surf. Sci.*, vol. 230, no. 1-4, pp. 232 - 240, 2004.

[23] M. Farzaneh and D. K. Sarkar, "Superhydrophobic and Icephobic Nanometric Coatings," in *International Conference on Polymeric Materials in Power Engineering (ICPME)*, Bangalore, India, 2007, p. IVB–4.

[24] G. Palasantzas and J. T. M. de Hosson, "Wetting on Rough Surfaces," *Acta mater.*, vol. 49, no. 17, pp. 3533 - 3538, 2001.

[25] N. Eustathopolous, "Dynamics of Wetting in Reactive Metal/Ceramic Systems," *Acta mater.*, vol. 46, no. 7, pp. 2319 - 2327 , 1998.

[26] N. J, Shirtcliffe, G. McHale, and M. I, Perry, C. C Newton, "Wetting and Wetting Transitions on Copper-Based Super-Hydrophobic Surfaces," *Langmuir*, vol. 21, no. 3, pp. 937 - 943, 2005.

[27] L. Feng et al., "Super-Hydrophobic Surfaces: From Natural to Artificial," *Adv. Mater.*, vol. 14, no. 24, pp. 1857 - , 2002.

[28] Y. Zheng, X. Gao, and L. L. Jiang, "Directional Adhesion of Superhydrophobic Butterfly Wings," *Soft Matter*, vol. 3, pp. 178 - 182, 2007.

[29] W. Barthlott and C. Neinhuis, "Purity of the Sacred Lotus, or Escape from Contamination in Biological Surfaces," *Planta*, vol. 202, no. 1, pp. 1 - 8, 1997.

[30] D. Quéré, "Non-sticking Drops," *Rep. Prog. Phys.*, vol. 68, pp. 2495 - 2532, 2005.

[31] J. Kreuter, "Nanoparticles - A Historical Perspective," *Int. J. Pharm.* , vol. 331, no. 1, pp. 1 -10, 2007.

[32] N. Anton, J. P. Benoit, and P. Saulnier, "Design and Production of Nanoparticles Formulated from Nano-emulsion Templates - A Review," *J. Controlled Release*, vol. 128, no. 3, pp. 185 - 199, 2008.

[33] M. Hosokawa, K. Nogi, M. Naito, and T. Yokoyama, *Nanoparticle Technology Handbook.*: Elsevier, 2007.

[34] M. C. Roco, "Nanoparticles and Nanotechnology Research," *J. Nanopart. Res.*, vol. 1, no. 1, pp. 1 - 6, 1999.

[35] S. Chen and D. L. Carroll, "Synthesis and Characterization of Truncated Triangular Silver Nanoplates," *Nano Lett.*, vol. 2, no. 9, pp. 1003 - 1007, 2002.

[36] E. Burkarter et al., "Superhydrophobic Electrosprayed PTFE," *Surf. Coat. Technol.* , vol. 202, pp. 194 - 198, 2007.

[37] M. Farzaneh, "Ice Accretions on High-Voltage Conductors and Insulators and Related Phenomena," *Philosophical Transactions: Mathematical, Physical and Engineering Sciences*, vol. 358, no. 1776, pp. 2971 - 3005, 2000.

[38] A. Goel, "Design of Transmission Lines for Atmospheric Icing," in *Atmospheric Icing of Power Networks*, M. Farzaneh, Ed.: Springer, 2008, ch. 8, pp. 327 - 371.

[39] J. Levine, "Statistical Explanation of Spontaneous Freezing of Water Droplets," NASA Center: Glenn Research Center, Report NACA-TN-2234, 1950.

[40] Freezing Nucleus in Britannica Online Encyclopedia. [Online]. http://www.britannica.com/EBchecked/topic/218741/freezing-nucleus

[41] X. L. Hu and A. Michaelides, "Ice Formation on Kaolinite: Lattice Match or Amphoterism?," *Surf. Sci.*, vol. 601, no. 23, pp. 5378 - 5381, 2007.

[42] M. Palanisamy, K. Thangaraj, R. Gobinathan, and P. Ramasamy, "X-Ray Diffraction and Ice Nucleation Studies of AgI-AgBr-CuI System," *J. Mater. Sci.*, vol. 21, no. 3, pp. 1075 - 1079, 1986.

[43] H. P. Pruppacher and J. D. Klett, *Microphysics of Clouds and Precipitation*, 2nd ed.: Springer, 1997.

[44] D. Rosenfeld and W. L. Woodley, "Deep Convective Clouds with Sustained Supercooled Liquid Water Down to -37.5°C," *Nature*, vol. 405, pp. 440 - 442, 2000.

[45] A. Tabazadeh, Y. S. Djikaev, and H. Reiss, "Surface Crystallization of Supercooled Water in Clouds," *PNAS*, vol. 99, no. 25, pp. 15873 - 15878, 2002.

[46] M. Farzaneh, J. Kiernicki, and F. J. Drapeau, "Ice Accretion on Energized Line

Insulators," *IJOPE*, vol. 2, no. 3, 1992.

[47] D. Kuroiwa, "Icing and Snow Accretion on Electric Wires," CRREL Res. Report 123, 1965.

[48] Glaze in the Glossary of Meteorology. [Online]. http://amsglossary.allenpress.com/glossary/search?id=glaze1

[49] Rime Ice in the Glossary of Meteorology. [Online]. http://amsglossary.allenpress.com/glossary/search?id=rime-ice1

[50] D. L. Minsk, "Ice Accumulation on Ocean Structures," CRREL Res. Report 77-17 , 1977.

[51] V. K. Jaiswal, Finite Element Modeling of Electric Field Distributions around A Resistive Glazed Post Station Insulator Covered with Ice, Ph.D. thesis, University of Quebec at Chicoutimi, 2005.

[52] M. Landy and A. Freiberger, "Studies of Ice Adhesion, I: Adhesion of Ice to Plastics," *J. Colloid Interface Sci.*, vol. 25, pp. 231 - 244, 1967.

[53] U. Bovensiepen, "Ultrafast Electron Transfer, Localization and Solvation at Ice-Metal Interfaces: Correlation of Structure and Dynamics," *Prog. Surf. Sci.*, vol. 78, no. 3-4, 87 - 100 2005.

[54] I. A. Ryzhkin and V. F. Petrenko, "Proton Ordering in Ice at an Ice–Metal Interface," *J. Exp. Theor. Phys.*, vol. 101, no. 2, pp. 317 - 321, 2005.

[55] G. R. Desiraju, "Hydrogen Bridges in Crystal Engineering: Interactions without Borders," *Acc. Chem. Res.* , vol. 35, no. 7, pp. 565 - 573, 2002.

[56] M. R. Kasaai and M. Farzaneh, "Analytical Evaluation of Existing Mechanisms of Ice Adhesion on Power Network Equipment," in *The 23rd International Conference on Offshore Mechanics and Arctic Engineering*, Vancouver, Canada, 2004, p. 51267.

[57] M. Javan-Mashmool, C. Volat, and M. Farzaneh, "A New Method for Measuring Ice Adhesion Strength at an Ice / Substrate Interface," *Hydrol. Processes*, vol. 20, no. 4, pp. 645 - 655, 2006.

[58] M. R. Kasaai and M. Farzaneh, "A Critical Evaluation of the Existing Methods to Determine Ice Adhesion Strength," in *The 23rd International Conference on Offshore Mechanics and Arctic Engineering*, Vancouver, Canada, 2004, p. 51264.

[59] J. M. Sayward, "Seeking Low Ice Adhesion," US Army Regions Research and Engineering Laboratory, Special Report AD-A071-040, 1979.

[60] P. Archer and V. Gupta, "Measurement and Control of Ice Adhesion to Aluminum 6061 Alloy," *J. Mech. Phys. Solids*, vol. 46, no. 10, pp. 1745 - 1771, 1998.

[61] S. Krongelb, "Electromagnetic Tensile Adhesion Tests Methods," in *Adhesion Measurements of Thin Films, Thick Films and Bulk Coatings*, L. K. Mittal, Ed.: American Society for Testing and Materials, 1978, vol. 640, pp. 107 - 121.

[62] J. Ahn, L. K. Mittal, and R. H. McQueen, "Hardness and Adhesion of Filmed Structures as Determined by the Scratch Techniques," in *Adhesion Measurements of Thin Films, Thick Films and Bulk Coatings*, L. K. Mittal, Ed.: American Society for Testing and Materials, 1978, pp. 134 - 157.

[63] J. W. McBain and W. B. Lee, "Third and Final Report of the Adhesives Research Committee," *J. Phys. Chem.*, vol. 37, no. b, pp. 826 - 827, 1933.

[64] D. L. Loughborough and E. G. Hass, "Reduction of the Adhesion of Ice to De-Icer Surfaces," *J. Aero. Sci.*, vol. 13, p. 126, 1946.

[65] D. L. Loughborough, "The Physics of the Mechanical Removal of Ice from Aircraft," *Aeronautical Engineering Review*, vol. 11, no. 2, pp. 29 - 34, 1952.

[66] C. L. Phan, P. McComber, and A. Mansianx, "Adhesion of Rime and Glaze on Conductors Protected by Various Materials," *Transactions CSME*, vol. 4, no. 4, pp. 204 - 208, 1976.

[67] J. Druez, C. L. Phan, J. L. Laforte, and D. D.. Nguyen, "The Adhesion of Glaze and Rime on Aluminum Electric Conductors," *Transactions CSME*, vol. 5, no. 4, pp. 215 - 220, 1979.

[68] J. L. Laforte, C. L. Phan, B. Felin, and R. Martin, "Adhesion of Ice on Aluminum

Conductor and Crystal Size in the Surface Layer," CRREL Special Report, pp. 83 - 91, 1983.

[69] J. W. Beams, J. B. Breazeale, and W. L. Bart, "Mechanical Strength of Thin Film of Metals," *Phys. Rev.*, vol. 100, no. 6, pp. 1657 - 1661, 1955.

[70] L. E. Raraty and D. Tabor, "The Adhesion and Strength Properties of Ice," *Proc. R. Soc. Lond. A* , vol. 245, no. 1241, pp. 184 - 201, 1958.

[71] J. R. Stallabrass and R. D. Price, "On the Adhesion of Ice to Various Materials," NRC Report LR-350, 1962.

[72] K. Itagaki, "Adhesion of Ice to Polymers and Other Surfaces," in *Physicochemical Aspects of Polymer Surfaces*, K. L. Mittal, Ed.: Plenum Press, 1983, p. 241.

[73] K. Itagaki, "The Implications of Surface Energy in Ice Adhesion," *J. Adhesion*, vol. 16, pp. 41 - 48, 1983.

[74] I. E. Kozitsokii, "The Shear Strength of Ice," *Metoralgiya I. Gidrolgiya*, no. 3, pp. 103 - 105 , 1978.

[75] V. F. Petrenko, "Study of the Surface of Ice, Ice/Solid and Ice/Liquid Interfaces with Scanning Force Microscopy," *J. Phys. Chem. B*, vol. 101, no. 32, p. 6276 – 6281, 1997.

[76] J. G. Dash, A. W. Rempel, and J. S. Wettlaufer, "The Physics of Premelted Ice and Its Geophysical Consequences," *Rev. Mod. Phys.*, vol. 78, no. 3, pp. 695 - 741, 2006.

[77] W. A. Weyl, "Surface Structure of Water and Some of Its Physical and Chemical Manifestations," *J. Colloid Sci.*, vol. 6, no. 5, pp. 389 - 405, 1951.

[78] N. V. Churaev, S. A. Bardasov, and V. D. Sobolev, "On the Non-Freezing Water Interlayers between Ice and a Silica Surface," *Colloids Surf. A*, vol. 79, no. 1, pp. 11 - 24, 1993.

[79] D. Beaglehole and P. Wilson, "Extrinsic Premelting at the Ice-glass Interface," *J. Phys. Chem.* , vol. 98, no. 33, pp. 8096 - 8100, 1994.

[80] H. Bluhm, D. F. Ogletree, C. S. Fadley, Z. Hussain, and N. Salmeron, "The

Premelting of Ice Studied with Photoelectron Spectroscopy," *J. Phys.: Condens. Matter*, vol. 14, pp. L277 - L233, 2002.

[81] T. Ishizaki, M. Maruyama, Y. Furukawa, and J. G. Dash, "Premelting of Ice in Porous Silica Glass," *J. Cryst. Growth*, vol. 163, no. 4, pp. 455 - 460, 1996.

[82] L. Daikhin and V. Tsionsky, "Hydration Forces and Liquid-like Layer on the Ice/metal Interface," *J. Phys.: Condens. Matter*, vol. 19, no. 37, pp. 376109.1 - 376109.16, 2007.

[83] I. Golecki and C. Jaccard, "Intrinsic Surface Disorder in Ice Near the Melting Point," *J. Phys. C*, vol. 11, pp. 4229 - 4237, 1978.

[84] H. Dosch, A. Lied, and J. H Bilgram, "Glancing-angle X-ray Scattering Studies of the Premelting of Ice Surfaces," *Surf. Sci.*, vol. 327, no. 1-2, pp. 145 - 164, 1995.

[85] S. Engemann et al., "Interfacial Melting of Ice in Contact with SiO2," *Phys. Rev. Lett.*, vol. 92, no. 20, pp. 205701 - 205705, 2004.

[86] A. Döppenschmidt and H. J. Butt, "Measuring the Thickness of the Liquid-like Layer on Ice Surfaces with Atomic Force Microscopy," *Langmuir*, vol. 16, no. 16, pp. 6709 - 6714, 2000.

[87] R. R. Gilpin, "Wire Regelation at Low Temperatures," *J. Colloid Interface Sci.*, vol. 77, no. 2, pp. 435 - 448, 1980.

[88] K. R. Wilson et al., "Surface Relaxation in Liquid Water and Methanol Studied by X-Ray Absorption Spectroscopy," *J. Chem. Phys.*, vol. 17, no. 16, pp. 7738 - 7744, 2002.

[89] X. Wang et al., "The Calculation of the Surface Energy of High-Index Surfaces in Metals at Zero Temperature," *Surf. Sci.* , vol. 551, no. 3, pp. 179 - 188, 2004.

[90] J. M. Zhang, F. Ma, and K. W. Xu, "Calculation of the Surface Energy of FCC Metals with Modified Embedded-Atom Method," *Chinese Phys.*, vol. 13, no. 7, pp. 1082 - 1090, 2004.

[91] K. F. Wojciechowski, "Surface Energy of Metals: Theory and Experiment," *Surf.*

Sci., vol. 437, no. 3, pp. 285 - 288, 1999.

[92] L. Vitos, A. V. Ruban, H. L. Skriver, and J. Kollar, "The Surface Energy of Metals," *Surf. Sci.*, vol. 411, no. 1, pp. 186 - 202, 1998.

[93] J. N. Israelachvili, *Intermolecular and Surface Forces*, 2nd ed.: Academic Press, 1992.

[94] P. Roura and J. Fort, "Local Thermodynamic Derivation of Young's Equation," *J. Colloid Interface Sci.*, vol. 272, no. 2, pp. 420 - 429, 2004.

[95] D. Öner and T. J. McCarthy, "Ultrahydrophobic Surfaces. Effects of Topography Length Scales on Wettability," *Langmuir*, vol. 16, no. 20, pp. 7777 - 7782, 2000.

[96] B. He, J. Lee, and N. A. Patankar, "Contact Angle Hysteresis on Rough Hydrophobic Surfaces," *Colloids Surf., A* , vol. 248, no. 1-3, pp. 101 - 104, 2004.

[97] D. Li and A. W. Neumann, "Surface heterogeneity And Contact Angle Hysteresis," *Colloid Polym. Sci.*, vol. 270, no. 5, pp. 498 - 504, 1992.

[98] G. McHale, N. J. Shirtcliffe, and M. I. Newton, "Contact-Angle Hysteresis on Super-Hydrophobic Surfaces," *Langmuir*, vol. 20, no. 23, pp. 10146 - 10149, 2004.

[99] A. Maestre Caro, G. Maes, G. Borghs, and C. M. Whelan, "Screening Self-assembled Monolayers as Cu Diffusion Barriers," *Microelectron. Eng.*, vol. 85, no. 10, pp. 2047 - 2050, 2008.

[100] G. Bracco, D. Cavanna, S. Thea, and V. D. Renzi, "Structural Study of CH3S Self-assembled Monolayers on Au(111)," *Vacuum*, vol. 82, no. 12, pp. 1421 - 1424, 2008.

[101] X. F. Ang, F. Y. Li, J. Wei, W. L. Tan, and C. C. Wong, "A Thermal and Passivation Study of Self-assembled Monolayers on Thin Gold Films," *Thin Solid Films*, vol. 516, no. 16, pp. 5721 - 5724, 2008.

[102] E. F. Hare, E. G. Shafrin, and W. A. Zisman, "Properties of Films of Adsorbed Fluorinated Acids," *J. Phys. Chem.* , vol. 58, no. 3, pp. 236 - 239, 1954.

[103] T. Nishino, M. Meguro, K. Nakamae, M. Matsushita, and Y. Ueda, "The Lowest Surface Free Energy Based on -CF3 Alignment," *Langmuir*, vol. 15, no. 13, pp. 4321

- 4323, 1999.

[104] B. Solmo and V. Gupta, "A Hydrophobic Self-assembled Monolayer with Improved Adhesion to Aluminum for Deicing Application," *Mech. Mater.* , vol. 33, no. 8, pp. 471 - 480, 2001.

[105] D. N. Anderson and A. D. Reich, "Tests of the Performance of Coatings for Low Ice Adhesion," NASA Technical Memorandum, Report 107399 AIAAA-97-0303, 1997.

[106] E. G. Shafrin and W. A. Zisman, "Upper Limits to the Contact Angles of Liquids on Solids," in *Contact Angle, Wettability and Adhesion, vol 34 of Advances in Chemistry Series*, Fowkes, Ed.: American Chemical Society, 1964, p. 145.

[107] M. Ma and R. M. Hill, "Superhydrophobic Surfaces," *Curr. Opin. Colloid Interface Sci.*, vol. 11, no. 4, pp. 193 - 202, 2006.

[108] C. Neinhuis and W. Barthlott, "Characterization and Distribution of Water-repellent, Self-cleaning Plant Surfaces," *Anal. Bot.*, vol. 79, no. 6, pp. 667 - 677, 1997.

[109] A. Marmur, "Wetting on Hydrophobic Rough Surfaces: To Be Heterogeneous or Not To Be?," *Langmuir*, vol. 19, no. 20, pp. 8343 - 8348, 2003.

[110] R. N. Wenzel, "Resistance of Solid Surfaces to Wetting by Water," *Ind. Eng. Chem.*, vol. 28, pp. 988 - 994, 1936.

[111] M. Nosonovsky and B. Bhushan, "Stochastic Model for Metastable Wetting of Roughness-Induced Superhydrophobic Surfaces," *Microsyst. Technol.*, vol. 12, no. 3, pp. 231 - 237, 2006.

[112] A. B. D. Cassie and S. Baxter, "Wettability of Porous Surfaces," *Trans. Faraday Soc.*, vol. 40, pp. 546 - 551, 1944.

[113] J. Bico, C. Marzolin, and D. Quéré, "Pearl Drops," *Europhys. Lett.*, vol. 47, no. 2, pp. 220 - 226, 1999.

[114] A. Nakajima, K. Hashimoto, and T. Watanabe, "Recent Studies on Super-Hydrophobic Films," *Monatsh. Chem.*, vol. 132, no. 1, pp. 31 - 41, 2001.

[115] G. Wolansky and A. Marmur, "Apparent Contact Angles on Rough Surfaces: the

Wenzel Equation Revisited," *Colloids Surf., A*, vol. 156, no. 1-3, pp. 381 - 388, 1999.

[116] S. Brandon, N. Haimovich, E. Yeger, and A. Marmur, "Partial Wetting of Chemically Patterned Surfaces: The Effect of Drop Size," *J. Colloid Interface Sci.*, vol. 263, no. 1, pp. 237 - 243, 2003.

[117] R. E. Johnson and R. H. Dettre, "Contact Angle Hysteresis - I. Study of an Idealized Rough Surface," in *Contact Angle, Wettability and Adhesion, vol 34 of Advances in Chemistry Series*, R. F. Gould, Ed.: American Chemical Society, 1964, p. 112.

[118] N. A. Patankar, "Transition between Superhydrophobic States on Rough Surfaces," *Langmuir*, vol. 20, no. 17, pp. 7987 - 7102, 2004.

[119] J. L. Zhang, J. A. Li, and Y. C. Han, "Superhydrophobic PTFE Surfaces by Extension," *Macromol. Rapid Commun.*, vol. 25, no. 11, pp. 1105 - 1108, 2004.

[120] R. Menini and M. Farzaneh, "Production of Superhydrophobic Polymer Fibers with Embedded particles using the Electrospinning Technique," *Polym. Int.*, vol. 57, no. 1, pp. 77 - 84, 2008.

[121] A. Singh, L. Steely, and H. R. Allcock, "Poly[bis(2,2,2-trifluoroethoxy)phosphazene] Superhydrophobic Nanofibers," *Langmuir*, vol. 21, no. 25, pp. 11604 - 11607, 2005.

[122] M. T. Khorasani, H. Mirzadeh, and Z. Kermani, "Wettability of Porous Polydimethylsiloxane Surface: Morphology Study," *Appl. Surf. Sci.*, vol. 242, no. 3-4, pp. 339 - 345, 2005.

[123] M. H. Jin et al., "Superhydrophobic PDMS Surface with Ultra-low Adhesive Force," *Macromol. Rapid Commun.*, vol. 26, no. 22, pp. 1805 - 1809, 2005.

[124] M. H. Sun et al., "Artificial Lotus Leaf by Nanocasting," *Langmuir*, vol. 21, no. 19, pp. 8978 - 8981, 2005.

[125] X. Y. Lu, C. C. Zhang, and Y. C. Han, "Low-density Polyethylene Superhydrophobic Surface by Control of Its Crystallization Behavior," *Macromol. Rapid Commun.*, vol. 25, no. 18, pp. 1606 - 1610, 2004.

[126] L. Jiang, Y. Zhao, and J. Zhai, "A Lotus-Leaf-Like Superhydrophobic Surface: A

Porous Microsphere/Nanofiber Composite Film Prepared by Electrohydrodynamics," *Angew. Chem. Int. Ed.*, vol. 43, no. 33, pp. 4338 - 4341, 2004.

[127] H. Yan, K. Kurogi, H. Mayama, and K. Tsujii, "Environmentally Stable Super Water-repellent Poly(alkylpyrrole) Films," *Angew. Chem. Int. Ed.*, vol. 44, no. 22, pp. 3453 - 3456, 2005.

[128] N. Saleema and M. Farzaneh, "Thermal Effect on Superhydrophobic Performance of Stearic Acid Modified ZnO Nanotowers," *Appl. Surf. Sci.*, vol. 254, no. 9, pp. 2690 - 2695, 2008.

[129] Y. H. Yang et al., "Self-assembled ZnO agave-like Nanowires and Anomalous Superhydrophobicity," *J. Phys. Condens. Matter*, vol. 17, no. 35, pp. 5441 - 5446, 2005.

[130] X. J. Feng, J. Zhai, and L. Jiang, "The Fabrication and Switchable Superhydrophobicity of TiO_2 Nanorod Films," *Angew. Chem. Int. Ed.*, vol. 44, no. 32, pp. 5115 - 5118, 2005.

[131] K. Teshima, H. Sugimura, Y. Inoue, O. Takai, and A. Takano, "Transparent Ultra Water-Repellent Poly(Ethylene Terephthalate) Substrates Fabricated by Oxygen Plasma Treatment and Subsequent Hydrophobic Coating," *Appl. Surf. Sci.*, vol. 244, no. 1-4, pp. 619 - 622, 2005.

[132] X. Y. Song, J. Zhai, Y. L. Wang, and L. Jiang, "Fabrication of Superhydrophobic Surfaces by Self-Assembly and Their Water-Adhesion Properties," *J. Phys. Chem. B*, vol. 109, no. 9, pp. 4048 - 4052, 2005.

[133] B. T. Qian and Z. Q. Shen, "Fabrication of Superhydrophobic Surfaces by Dislocation-Selective Chemical Etching on Aluminum, Copper, and Zinc Substrates," *Langmuir*, vol. 21, no. 20, pp. 9007 - 9009, 2005.

[134] M. E. Abdelsalam, P. N. Bartlett, T. Kelf, and J. Baumberg, "Wetting of Regularly Structured Gold Surfaces," *Langmuir*, vol. 21, no. 5, pp. 1753 - 1757, 2005.

[135] E. Martines et al., "Superhydrophobicity and Superhydrophilicity of Regular

Nanopatterns," *Nano Lett.*, vol. 5, no. 10, pp. 2097 - 2103, 2005.

[136] N. J. Shirtcliffe, G. McHale, M. I. Newton, C. C. Perry, and P. Roach, "Porous Materials Show Superhydrophobic to Superhydrophilic Switching," *Chem. Commun.*, no. 25, pp. 3135 - 3137 , 2005.

[137] M. Hikita, K. Tanaka, T. Nakamura, T. Kajiyama, and A. Takahara, "Superliquid-Repellent Surfaces Prepared by Colloidal Silica Nanoparticles Covered with Fluoroalkyl Groups," *Langmuir*, vol. 21, no. 16, pp. 7299 - 7302, 2005.

[138] F. Shi, Z. Q. Wang, and X. Zhang, "Combining a Layer-by-layer Assembling Technique with Electrochemical Deposition of Gold Aggregates to Mimic the Legs of Water Striders," *Adv. Mater.*, vol. 17, no. 8, pp. 1005 - 1009, 2005.

[139] N. Zhao, F. Shi, Z. Q. Wang, and X. Zhang, "Combining Layer-by-Layer Assembly with Electrodeposition of Silver Aggregates for Fabricating Superhydrophobic Surfaces," *Langmuir*, vol. 21, no. 10, pp. 4713 - 4716, 2005.

[140] X. Zhang et al., "Polyelectrolyte Multilayer as Matrix for Electrochemical Deposition of Gold Clusters: Toward Super-Hydrophobic Surface," *J. Am. Chem. Soc.*, vol. 126, no. 10, pp. 3064 - 3065, 2004.

[141] E. Hosono, S. Fujihara, I. Honma, and H. S. Zhou, "Superhydrophobic Perpendicular Nanopin Film by the Bottom-up Process," *J. Am. Chem. Soc.*, vol. 127, no. 39, pp. 13458 - 13459, 2005.

[142] L. Huang et al., "Stable Superhydrophobic Surface via Carbon Nanotubes Coated with a ZnO Thin Film," *J. Phys. Chem. B*, vol. 109, no. 16, pp. 7746 - 7748, 2005.

[143] S. Shibuichi, T. Onda, N. Satoh, and K. Tsujii, "Super Water-Repellent Surfaces Resulting from Fractal Structure," *J. Phys. Chem.*, vol. 100, no. 50, pp. 19512 - 19517, 1996.

[144] S. Veeramasuneni, J. Drelich, J. D. Miller, and G. Yamauchi, "Hydrophobicity of Ion-plated PTFE Coatings," *Prog. Org. Coat.*, vol. 31, no. 3, pp. 265 - 270, 1997.

[145] M. Farzaneh and D. K. Sarkar, "Nanostructured Superhydrophobic Coatings," *The*

Journal of Central Power Research Institute, vol. 4.(2008) 135. , no. 2, pp. 135 - 147.

[146] T. Kako et al., "Adhesion and Sliding of Wet Snow on A Super-Hydrophobic Surface with Hydrophilic Channels," *J. Mater. Sci.*, vol. 39, no. 2, pp. 547 - 555, 2004.

[147] H. Saito, K. Takai, and G. Yamauchi, "Water- and Ice-repellent Coatings," *Surf. Coat. Int. 80 (1997) 168.* , vol. 80, no. 4, pp. 168 - 171, 1997.

[148] J. Y. Shiu, C. W. Kuo, P. Chen, and C. Y. Mou, "Fabrication of Tunable Superhydrophobic Surfaces by Nanosphere Lithography," *Chem. Mater.*, vol. 16, no. 4, pp. 561 - 564, 2004.

[149] A. T. Bell, "The Impact of Nanoscience on Heterogeneous Catalysis," *Science*, vol. 229, no. 5613, pp. 1688 - 1691, 2003.

[150] J. G. Pepin, "Multilayer Ceramic Capacitor Electrodes: Powder Technology and Fired Properties," *J. Mater. Sci. - Mater. Electron.*, vol. 2, no. 1, pp. 34 - 39, 1991.

[151] M. D. Musick, C. D. Keating, M. Keefe, and M. J. Natan, "Stepwise Construction of Conductive Au Colloid Multilayers from Solution," *Chem. Mater.*, vol. 9, no. 7, pp. 1499 - 1501, 1997.

[152] N. Pradhan, A. Pal, and T. Pal, "N. Pradhan, A. Pal, T. Pal, "Silver Nanoparticle Catalyzed Reduction of Aromatic Nitro Compounds," *Colloids Surf. A*, vol. 196, no. 2-3, pp. 247 - 257, 2002.

[153] P. Yáñez-Sedeño and J. M. Pingarrón, "Gold Nanoparticle-Based Electrochemical Biosensors," *Anal. Bioanal. Chem.*, vol. 382, no. 4, pp. 884 - 886, 2005.

[154] Q. L. Feng, F. Z. Cui, T. N. Kin, and J. W. Kin., "Ag-Substituted Hydroxyapatite Coatings with Both Antimicrobial Effects and Biocompatibility," *J. Mater. Sci. Lett.*, vol. 18, no. 7, pp. 559 - 561, 1999.

[155] H. Inouye, K. Tanaka, I. Tanahashi, T. Hattori, and H. Nakatsuka, "Ultrafast Optical Switching in a Silver Nanoparticle System," *Jpn. J. Appl. Phys. Part 1*, vol. 39, no. 9A, pp. 5132 - 5133, 2000.

[156] S. Sun and C. B. Murray, "Synthesis of Monodisperse Cobalt Nanocrystals and Their

Assembly into Magnetic Superlattices," *J. Appl. Phys.*, vol. 85, no. 8, pp. 4325 - 4330, 1999.

[157] D. V. Goia, "Preparation and Formation Mechanisms of Uniform Metallic Particles in Homogeneous Solutions," *J. Mater. Chem.*, vol. 14, no. 4, pp. 451 - 458, 2004.

[158] S. Griffith, M. Mondol, D. S. Kong, and J. M. Jacobson, "Nanostructure Fabrication by Direct Electron-beam Writing of Nanoparticles," *J. Vac. Sci. Technol. B*, vol. 20, no. 6, pp. 2768 - 2772, 2002.

[159] Y. Sun and Y. Xia, "Shape-controlled Synthesis of Gold and Silver Nanoparticles," *Science*, vol. 298, no. 5601, pp. 2176 - 2179, 2002.

[160] B. Wiley, Y. Sun, B. Mayers, and Y. Xia, "Shape-controlled Synthesis of Metal Nanostructures: The Case of Silver," *Chem. Eur. J.*, vol. 11, no. 2, pp. 454 - 463, 2005.

[161] R. J. Chimentão et al., "Different Morphologies of Silver Nanoparticles as Catalysts for the Selective Oxidation of Styrene in the Gas Phase," *Chem. Commun.*, no. 7, pp. 846 - 847, 2004.

[162] Y. Liu, X. Chen, and J. H. Xin, "Super-Hydrophobic Surfaces from a Simple Coating Method: A Bionic Nanoengineering Approach," *Nanotechnology*, vol. 17, pp. 3259 - 3263, 2006.

[163] H. M. Shang et al., "Optically Transparent Superhydrophobic Silica-Based Films," *Thin Solid Films*, vol. 472, no. 1 - 2, pp. 37 - 43, 2005.

[164] T. Lin, C. Wu, and C. Hsieh, "Enhancement of Water-repellent Performance on Functional Coating by Using the Taguchi Method," *Surf. Coat. Technol.*, vol. 200, no. 18 - 19, pp. 5253 - 5258, 2006.

[165] C. Hsieh, J. Chen, R. Kuo, T. Lin, and C. Wu, "Influence of Surface Roughness on Water- and Oil-Repellent Surfaces Coated With Nanoparticles," *Appl. Surf. Sci.*, vol. 240, no. 1 - 4, pp. 318 - 326, 2005.

[166] Y. Zhao, Q. Lu, D. Chen, and Y. Wei, "Superhydrophobic Modification of Polyimide

Films Based on Gold-Coated Porous Silver Nanostructures and Self-assembled Monolayers," *J. Mater. Chem.*, vol. 16, no. 46, pp. 4504 - 4509, 2006.

[167] L. Zhai, F. C. Cebeci, R. E. Cohen, and M. F. Rubner, "Superhydrophobic Coatings," US Patent #20060029808, 2006.

[168] User Manual of DSA1 V1.9-02, Drop Shape Analysis Software for DSA100, KRÜSS GmbH, Hamburg, 2004.

[169] M. Callies, Y. Chen, F. Marty, A. Pépin, and D. Quéré, "Microfabricated Textured Surfaces for Super-hydrophobicity Investigations," *Microelectron. Eng.*, vol. 78 - 79, pp. 100 - 105, 2005.

[170] M. Mousavi, Experimental and Theoretical Verification of Two Icing Codes, M.Sc. thesis, University of Quebec at Chicoutimi, 2003.

[171] M. Kermani, Ice Shedding from Cables and Conductors - A Cracking Model of Atmospheric Ice, Ph.D. thesis, University of Quebec at Chicoutimi, 2007.

[172] G. Carotenuto, G. P. Pepe, and L. Nicolais, "Preparation and Characterization of Nano-sized Ag/PVP Composites for Optical Applications," *Eur. Phys. J. B*, vol. 16, no. 1, pp. 11 - 17, 2000.

[173] D. Kim, S. Jeong, and J. Moon, "Synthesis of Silver Nanoparticles using the Polyol Process and the Influence of Precursor Injection," *Nanotechnology*, vol. 17, pp. 4019 - 4024, 2006.

[174] S. S. Rozengauz, L. P. Repina, and É. M. Aizenshtein, "Effect of Technological Additives on the Dehydration of Ethylene Glycol in Polyethylene Terephthalate Synthesis," *Fibre Chem.*, vol. 13, no. 1, pp. 7 - 9, 1981.

[175] D. Chen and L. Gao, "Large-scale Growth and End-to-end Assembly of Silver Nanorods by PVP-directed Polyol Process," *J. Cryst. Growth*, vol. 264, no. 1 - 3, pp. 216 - 222, 2004.

[176] F. Fievet, J. P. Lagier, and M. Figlarz, "Preparing Monodisperse Metal Powders in Micrometer and Submicrometer Sizes by the Polyol Process," *MRS Bull.*, vol. 14, pp.

29 - 34, 1989.

[177] G. Carotenuto, "Synthesis and Characterization of Poly(N-vinylpyrrolidone) Filled by Monodispersed Silver Clusters with Controlled Size," *Appl. Organomet. Chem.*, vol. 15, no. 5, pp. 344 - 351, 2001.

[178] R. Jin et al., "Controlling Anisotropic Nanoparticle Growth through Plasmon Excitation," *Nature*, vol. 425, no. 6957, pp. 487 - 490, 2003.

[179] M. Andersson, J. S. Pedersen, and A. E. C. Palmqvist, "Silver Nanoparticle Formation in Microemulsions Acting Both as Template and Reducing Agent," *Langmuir*, vol. 21, no. 24, pp. 11387 - 11396, 2005.

[180] Z. Zhang, B. Zhao, and L. Hu, "PVP Protective Mechanism of Ultrafine Silver Powder Synthesized by Chemical Reduction Processes," *J. Solid State Chem.*, vol. 121, no. 1, pp. 105 - 110, 1996.

[181] C. Wu, B. P. Mosher, and T. Zeng, "One-step Green Route to Narrowly Dispersed Copper Nanocrystals," *J. Nanopart. Res.*, vol. 8, no. 6, pp. 965 - 969, 2006.

[182] K. P. Velikov, Zegers. G. E., and A. V. Blaaderen, "Synthesis and Characterization of Large Colloidal Silver Particles," *Langmuir*, vol. 19, no. 4, pp. 1384 - 1389, 2003.

[183] Y. Wang, P. Chen, and M. Liu, "Synthesis of Well-defined Copper Nanocubes by a One-Pot Solution Process," *Nanotechnology*, vol. 17, pp. 6000 - 6006, 2006.

[184] N. R. Jana, Z. L. Wang, T. K. Sau, and T. Pal, "Seed-mediated Growth Method to Prepare Cubic Copper Nanoparticles," *Curr. Sci.*, vol. 79, pp. 1367 - 1370, 2000.

[185] D. L. Allara and R. G. Nuzzo, "Spontaneously Organized Molecular Assemblies. 1. Formation, Dynamics, and Physical Properties of n-Alkanoic Acids Adsorbed from Solution on an Oxidized Aluminum Surface," *Langmuir*, vol. 1, no. 1, pp. 45 - 52, 1985.

[186] D. L. Allara and R. G. Nuzzo, "Spontaneously Organized Molecular Assemblies. 2. Quantitative Infrared Spectroscopic Determination of Equilibrium Structures of Solution-Adsorbed n–alkanoic Acids on An Oxidized Aluminum Surface,"

Langmuir, vol. 1, no. 1, pp. 52 - 66, 1985.

[187] N. E. Schlotter, M. D. Porter, T. B. Bright, and D. L. Allara, "Formation and Structure of A Spontaneously Adsorbed Monolayer of Arachidic on Silver," *Chem. Phys. Lett.*, vol. 132, no. 1, pp. 93 - 98, 1986.

[188] S. J. Lee and K. Kim, "Diffuse Reflectance Infrared Spectra of Stearic Acid Self-Assembled on Fine Silver Particles," *Vib. Spectrosc.*, vol. 18, no. 2, pp. 187 - 201, 1998.

[189] S. Ren, S. Yang, and Y. Zhao, "Micro- and Macro-Tribological Study on a Self-Assembled Dual-Layer Film," *Langmuir*, vol. 19, no. 7, pp. 2763 - 2767, 2003.

[190] M. Jiang and Z. Ning, "Influence of Deposition Pressure on The Structure and Properties of Fluorinated Diamond-like Carbon Films Prepared by RF Reactive Magnetron Sputtering," *Surf. Coat. Technol.*, vol. 200, no. 12 - 13, pp. 3682 - 3686 , 2006.

[191] D. K. Sarkar, M. Farzaneh, and R. W. Paynter, "Superhydrophobic Properties of Ultrathin rf-sputtered Teflon Films Coated Etched Aluminum Surfaces," *Mater. Lett.*, vol. 62, no. 8 - 9, pp. 1226 - 1229, 2008.

[192] Zonyl 8740 from DuPont. [Online]. http://www2.dupont.com/Zonyl_Foraperle/en_US/assets/downloads/Zonyl_8740.pdf

[193] H. I. Hsiang, M. T. Liang, H. C. Huang, and F. S. Yen, "Preparation of Superhydrophobic Boehmite and Anatase Nanocomposite Coating Films," *Mater. Res. Bull.*, vol. 42, no. 3, pp. 420 - 427, 2007.

[194] P. H. McCluskey, R. L. Snyder, and R. A. S. Condrate, "Infrared Spectral Studies of Various Metal Polyacrylates," *J. Solid State Chem.*, vol. 83, no. 2, pp. 332 - 339, 1989.

[195] A. Safaee, D. K. Sarkar, and M. Farzaneh, "Superhydrophobic Properties of Silver-Coated Films on Copper Surface by Galvanic Exchange Reaction," *Appl. Surf. Sci.*, vol. 254, no. 8, pp. 2493 - 2498, 2008.

[196] J. Shirtcliffe et al., "The Use of High Aspect Ratio Photoresist (SU-8) for Super-hydrophobic Pattern Prototyping," *J. Micromech. Microeng.*, vol. 14, no. 10, pp. 1384 - 1389, 2004.

[197] A. Ulman, "Formation and Structure of Self-assembled Monolayers," *Chem. Rev.*, vol. 96, no. 4, pp. 1533 - 1554, 1996.

[198] S. A. Kulinich and M. Farzaneh, "Hydrophobic Properties of Surfaces Coated with Fluoroalkylsiloxane and Alkylsiloxane Monolayers," *Surf. Sci.*, vol. 573, no. 3, pp. 379 - 390, 2004.

[199] D. G. Shchukin, I. L. Radtchenko, and G. B. Sukhorukov, "Photoinduced Reduction of Silver inside Microscale Polyelectrolyte Capsules," *Chemphyschem.*, vol. 4, no. 10, pp. 1101 - 1103, 2003.

[200] A. Safaee, D.K. Sarkar, and M. Farzaneh, "Large Scale Synthesis of Ordered Silver Nanoparticles Superhydrophobic and Anti-icing Applications," in *the NSTI Nanotechnology Conference and Trade Show*, Boston, Massachusetts, 2006, p. 190.

[201] R. He, X. Qian, J. Yin, and Z. Zhu, "Preparation of Polychrome Silver Nanoparticles in Different Solvents," *J. Mater. Chem.*, vol. 12, no. 12, pp. 3783 - 3786, 2002.

[202] C. Laforte, Étude de L'adhérence de la Glace sur des Solides À Caractère Glaciophobe, M.Sc. thesis, University of Quebec at Chicoutimi, 2001.

[203] Surface Tension Values of Some Common Test Liquids for Surface Energy Analysis. [Online]. http://www.surface-tension.de/

[204] V. N. Pustovit and T. V. Shahbazyan, "Quantum-size Effects in SERS from Noble-metal Nanoparticles," *Microelectron. J.*, vol. 36, no. 3 - 6, pp. 559 - 563, 2005.

[205] U. Kreibig and M. Vollmer, *Optical Properties of Metal Clusters.*: Springer, 1995.

[206] N. W. Ashcroft and N. D. Mermin, *Solid State Physics*. New York: Holt, Rinehart and Winston, 1976.

[207] H. Haberland, *Clusters of Atoms and Molecules: Theory, Experiment, and Clusters of Atoms.*: Springer-Verlag, 1994.

[208] G. Mie, "Optics of Turbid Media," *Ann. Phys.*, vol. 25, no. 3, pp. 377 - 445, 1908.

[209] S. Link and M. A. El-Sayed, "S. Link and M.A. El-Sayed, "Shape and Size Dependence of Radiative, Non-Radiative and Photothermal Properties of Gold Nanocrystals," *Int. Rev. Phys. Chem.*, vol. 19, no. 3, pp. 409 - 453, 2000.

[210] U. Kreibig, G. Bour, A. Hilger, and M. Gartz, "Optical Properties of Cluster-Matter: Influences of Interfaces," *Phys. Status Solidi A.*, vol. 175, no. 1, pp. 351 - 366, 1999.

[211] J. A. Greighton and D. G. Eaton, "Ultraviolet–visible Absorption Spectra of the Colloidal Metallic Elements," *J. Chem. Soc., Faraday Trans.*, vol. 78, no. 24, pp. 3881 - 3891, 1991.

[212] A. Taleb, C. Petit, and M. P. Pileni, "Optical Properties of Self-Assembled 2D and 3D Superlattices of Silver Nanoparticles," *J. Phys. Chem. B*, vol. 102, no. 12, pp. 2214 - 2220, 1998.

[213] B. N. J. Persson, "Polarizability of Small Spherical Metal Particles: Influence of the Matrix Environment," *Surf. Sci.*, vol. 281, no. 1 - 2, pp. 153 - 162, 1993.

[214] H. C. Hulst, *Light Scattering by Small Particles*, 2, Ed. New York, Courier Dover Publications Inc., 1981, pp. 11 - 13.

[215] H. Lamb, *Hydrodynamics*, 6th ed.: University Press, 1993, p. 599.

[216] D. R. Lide. CRC Handbook of Chemistry and Physics, Internet Version, CRC Press, Boca Raton, FL, 2005. [Online]. http://www.hbcpnetbase.com

APPENDIX A

SURFACE TENSION OF SOME LIQUIDS

Surface tension values of some common liquids for surface energy analysis [203]

Name	CAS Ref.-No.	Surface tension at 20°C in mN/m	Temperature coefficient in mN/(m K)
1,2-Dichloro ethane	107-06-2	33.30	-0.1428
1,2,3-Tribromo propane	96-11-7	45.40	-0.1267
1,3,5-Trimethylbenzene (Mesitylene)	108-67-8	28.80	-0.0897
1,4-Dioxane	123-91-1	33.00	-0.1391
1,5-Pentanediol	111-29-5	43.30	-0.1161
1-Chlorobutane	109-69-3	23.10	-0.1117
1-Decanol	112-30-1	28.50	-0.0732
1-nitro propane	108-03-2	29.40	-0.1023
1-Octanol	111-87-5	27.60	-0.0795
Acetone (2-Propanone)	67-64-1	25.20	-0.1120
Aniline 22°C (AN)	62-53-3	43.40	-0.1085
2-Aminoethanol	141-43-5	48.89	-0.1115
Anthranilic acid ethylester 22°C	87-25-2	39.30	-0.0935
Anthranilic acid methylester 25 °C	134-20-3	43.71	-0.1152
Benzene	71-43-2	28.88	-0.1291
Benzylalcohol	100-51-6	39.00	-0.0920
Benzylbenzoate (BNBZ)	120-51-4	45.95	-0.1066
Bromobenzene	108-86-1	36.50	-0.1160
Bromoform	75-25-2	41.50	-0.1308
Butyronitrile	109-74-0	28.10	-0.1037
Carbon disulfid	75-15-0	32.30	-0.1484
Quinoline	91-22-5	43.12	-0.1063
Chloro benzene	108-90-7	33.60	-0.1191
Chloroform	67-66-3	27.50	-0.1295
Cyclohexane	110-82-7	24.95	-0.1211
Cyclohexanol 25 °C	108-93-0	34.40	-0.0966
Cyclopentanol	96-41-3	32.70	-0.1011
p-Cymene	99-87-6	28.10	-0.0941
Decalin	493-01-6	31.50	-0.1031
Dichloromethane	75-09-2	26.50	-0.1284
Diiodomethane (DI)	75-11-6	50.80	-0.1376
1,3-Diiodopropane 23 °C	627-31-6	46.51	-0.1195
Diethylene glycol (DEG)	111-46-6	44.80	-0.0841
Dipropylene glycol	25265-71-8	33.90	-0.1070
Dipropylene glycol monomethylether	34590-94-8	28.41	-0.1088
Dodecyl benzene	123-01-3	30.70	
Ethanol	64-17-5	22.10	-0.0832
Ethylbenzene	100-41-4	29.20	-0.1094
Ethylbromide	74-96-4	24.20	-0.1159
Ethylene glycol (EG)	107-21-1	47.70	-0.0890
Formamide (FA)	75-12-7	58.20	-0.0842
Fumaric acid diethylester 22°C	623-91-6	31.40	-0.1039
Glycerol (GLY)	56-81-5	64.00	-0.0598
Ethylene glycol monoethyl ether (Ethyl	110-80-5	28.60	-0.0918

Cellosolve)			
Hexachlorobutadiene	87-68-3	36.00	-0.0994
Iodobenzene	591-50-4	39.70	-0.1123
Isoamylchloride	107-84-6	23.50	-0.1078
Isobutylchloride	513-36-0	21.90	-0.1144
Isopropanol	67-63-0	23.00	-0.0789
Isopropylbenzene	98-82-8	28.21	-0.1054
Isovaleronitrile	625-28-5	26.00	-0.0827
m-Nitrotoluene	99-08-1	41.40	-0.1140
Mercury	7439-97-6	425.41	-0.2049
Methanol	67-56-1	22.70	-0.0773
Methyl ethyl ketone (MEK)	78-93-3	24.60	-0.1199
Methyl naphthalene	90-12-0	38.60	-0.1118
N,N-dimethyl acetamide (DMA)	127-19-5	36.70	-0.1395
N,N-dimethyl formamide (DMF)	68-12-2	37.10	-0.1400
N-methyl-2-pyrrolidone	872-50-4	40.79	-0.1156
n-Decane (DEC)	124-18-5	23.83	-0.0920
n-Dodecane (DDEC)	112-40-3	25.35	-0.0884
n-Heptane	142-82-5	20.14	-0.0980
n-Hexadecane (HDEC)	544-76-3	27.47	-0.0854
n-Hexane (HEX)	110-54-3	18.43	-0.1022
n-Octane (OCT)	111-65-9	21.62	-0.0951
n-Tetradecane (TDEC)	629-59-4	26.56	-0.0869
n-Undecane	1120-21-4	24.66	-0.0901
n-Butylbenzene	104-51-8	29.23	-0.1082
n-Propylbenzene	103-65-1	28.99	-0.1071
Nitroethane	79-24-3	31.90	-0.1255
Nitrobenzene	98-95-3	43.90	-0.1177
Nitromethane	75-52-5	36.80	-0.1678
o-Nitrotoluene	88-72-2	41.50	-0.1229
Perfluoroheptane	335-57-9	12.85	-0.0972
Perfluorohexane	355-42-0	11.91	-0.0935
Perfluorooctane	307-34-6	14.00	-0.0902
Phenylisothiocyanate	103-72-0	41.50	-0.1172
Phthalic acid diethylester 22°C	84-66-2	37.00	-0.1018
Polyethylen glycol 200 (PEG)	25322-68-3	43.50	-0.1170
Polydimethyl siloxane (Baysilone M5)	9016-00-6	19.00	-0.0365
Propanol 25 °C	71-23-8	23.70	-0.0777
Pyridine	110-86-1	38.00	-0.1372
3-Pyridylcarbinol 23°C (PYC)	100-55-0	47.68	-0.1259
Pyrrol (PY)	109-97-7	36.60	-0.1100
Toluene	108-88-3	28.40	-0.1189
Tricresylphosphate (TCP)	1330-78-5	40.90	-0.0887
Water (WA)	7732-18-5	72.80	-0.1514
o-Xylene	95-47-6	30.10	-0.1101
m-Xylene	108-38-3	28.90	-0.1104

APPENDIX B

SURFACE ENERGY OF SOME METALS

Experimental surface energy values of some metals [92]

Name	Surface tension (mN/m)
Li	522-525
Na	260-261
K	130-145
Ca	490-502
Mg	760-785
Al	1143-1160
Pb	593-600
Ti	1989-2100
Mn	1543-1600
Fe	2417-2475
Cu	1790-1825
Ag	1246-1250
Pt	2475-2489
Au	1500-1506

APPENDIX C

SURFACE PLASMON RESONANCE

Metals include positive ionic cores with conduction electrons between them. When alternating external electric fields or waves are applied to a metal, electrons move so as to compensate the electric field inside the material (namely screening), pass beyond the neutral states, and again return to the neutral states and so on. This collective motion of electrons is called a "plasmon resonance" or Plasmon (figure APPX C.1).

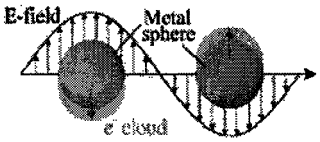

Figure APPX C.1 : Plasmon resonance of electrons in metallic nanoparticles.

The Plasmon of metallic nanoparticles is related to their size, shape and crystal structure. According to the number of atoms, there are three characteristic lengths that can be used to classify the nanoparticles optical responses, as indicated in figure APPX C.2.

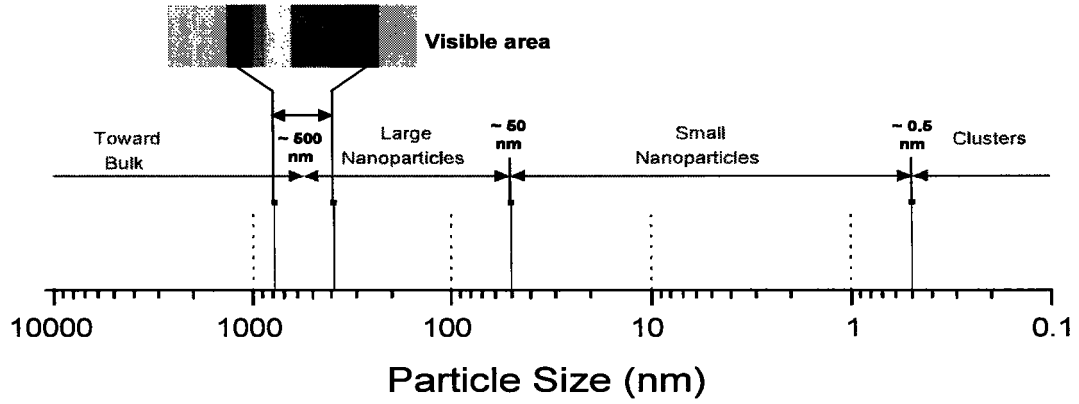

Figure APPX C.2 : Categories of nanoparticles based on their size.

When the size of a group of metal atoms is small, its properties can be dramatically different from those of bulk because of so-called quantum size or confinement effects,

which essentially arise from the presence of discrete atom-like electronic states [204]. Three size categories of metallic particles are: large nanoparticles, small nanoparticles and clusters, according to three characteristic length scales [205,206]. The first characteristic length scale encountered in shrinking from bulk to nanoparticles is the wavelength of light, ranging from 780nm for red to 390nm for violet. Optical responses of large conductive nanoparticles to external electromagnetic waves are simply dependent on their sizes, free electron density and refractive index of the surrounding medium [205]. The second essential length is electron mean free path, the average distance an electron goes between two collisions, which is ~50 nm in silver [206]. In these sizes, the dielectric function and refractive indices become size dependent, so the small nanoparticles have the different size-dependent optical responses compared with large nanoparticles. When particle size becomes comparable to the third characteristic length, Fermi wavelength of an electron, the wavelength of electron at the Fermi energy (~0.5 nm for silver) [207], the optical, electronic and chemical properties of metal clusters are dramatically different from the other two size regimes.

In macroscopic scale, the optical responses of nanoparticle systems are complex. The final measurement result is the average of behaviour of too many particles, ~$10^{14}/cm^3$, with statistically varying sizes, shapes and interactions among them and with surroundings. One of the first theoretical explanations of this phenomenon was presented by Mie [208] which has been continued by others [209]. A set of physically meaningful assumptions applied by Mie in 1908 leads to quantitatively description of optical properties of large, and sometimes small, Ag nanoparticles [205]. He considered a single metallic spherical particle with a

uniform isotropic dielectric function equal to the one of bulk material. The surrounding material also has a real and constant dielectric function and there is no effect from any neighbour particle. Then, the resulting complex dielectric response is calculated in incidence of an external plane, monochromatic electromagnetic wave. The total response in a macroscopic sample is the superposition of single particle responses [210].

The absorbance, A, for a dispersion of N particles per unit volume is given by [211]

$$A = CNl/2.303$$

where C and l are the absorption cross section and the optical path length, respectively. In the limit of $2\pi R < \lambda$ (where R is the radius of the particles and λ the wavelength of light in the medium), only the electric dipole mode can be excited, in Mie's theory expansion formula. So the cross section can be written as [212]:

$$C = (18\pi V \varepsilon_2(\omega)\varepsilon_m^{3/2})/\lambda[(\varepsilon_1(\omega)+2\varepsilon_m)^2+\varepsilon_2(\omega)^2]$$

in which V and λ are , respectively, the volume of the spherical particle and the incident wavelength, corresponding to a frequency ω. The complex relative permittivity of the metal, $\varepsilon(\omega)$, is expressed as

$$\varepsilon(\omega) = \varepsilon_1(\omega) + i\varepsilon_2(\omega)$$

When ε_2 is small or does not change so much around the band, the position of maximum absorption occurs for all $\varepsilon_1(\omega) = -2\varepsilon_m$. The wavelength of this plasmon resonance is therefore given by the wavelength dependence of $\varepsilon_1(\omega)$. The width and height of the resonance are determined by the $\varepsilon_2(\omega)$ value at this wavelength. Furthermore, the plasmon

peak width is related to the dielectric constant of the surrounding environment, ε_m [212,213].

The Ag particles achieved in this research have an average diameter in the range of ~195 to ~360 nm. The UV-visible spectrophotometer could measure the wavelengths of 190 to 1100nm. Having these values, the condition of $2\pi R < \lambda$ was not valid over the entire range and the higher-order terms in Mie theory should be considered. A complete derivation of Mie theory can be found in many text books such as [214]. However it was still possible to track the nanoparticles with their UV-visible absorption data and to compare with experimental curves in the literature or numerical values predicted by more general form of Mie theory.

APPENDIX D

CENTRIFUGATION

When the number of reduced ions (now neutral atoms) in the medium increases beyond a specific saturation level, they start joining together in the form of clusters and then nanoparticles [157]. The concentration of particles in solution is governed by reaction parameters. But after termination of reaction, the concentration of such particles should be increased before the solution is used for spin-coating.

Since the specific density of metallic particles is larger than that of the liquid, they normally start to fall down. The acceleration of weight is compensated by velocity-dependent friction with liquid and the particles reach a constant "precipitation velocity", V_o given by Stokes' law [215].

$$V_0 = \frac{1}{18}\frac{D^2 g(\rho_s - \rho_f)}{\eta}$$

where g is the gravitational acceleration, ρ_s, the density of solid, ρ_f, the density of fluid, D, the average particles diameter, and η, the viscosity of the liquid. In water with the viscosity of 0.894 mPas ([216], page 6-3), it takes 64 min for Ag nanoparticles with average diameter of 1 μm to pass a height of 2 cm of a vessel and precipitate. For similar particles (material, shape and average diameter) but in EG, that time period is 18 times longer, because EG has a viscosity of 16.1 mPas (at 25°C) ([216], page 6-187).

This precipitation process can be accelerated by increasing the g in the equation above, the gravity sensed by particles. This is done by centrifugation. Figure APPX D.1 shows the

centrifuge system and the colloid of nanoparticles type 1, before and after centrifugation at 3500 rpm for 45min.

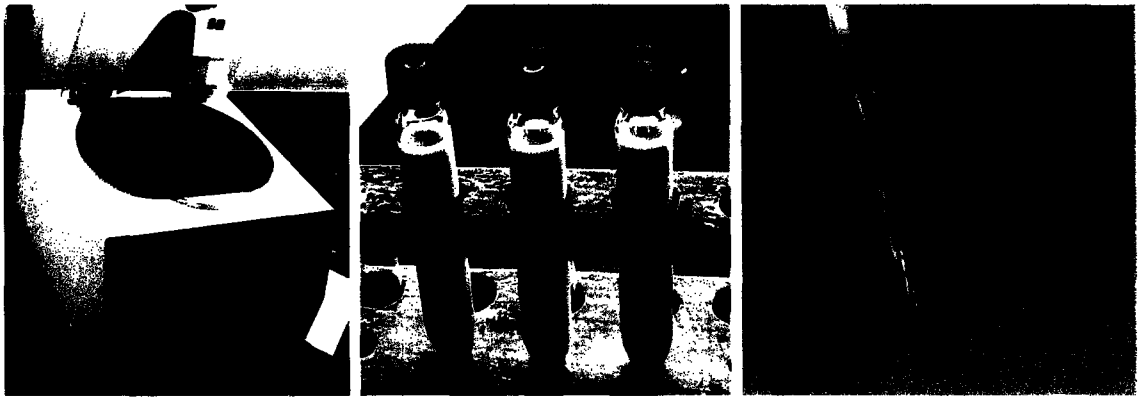

Figure APPX D.1: Centrifuge and silver nanoparticles in colloid before and after separation.

Centrifugation should be performed carefully to obtain a high quality final result. Usually, an additional solvent is added to an original reaction solution to be centrifuged. In presence of reactant ions, concentration of particles at the bottom of tube may give rise to unwanted reactions or agglomerations. Adding a relatively large amount of another solvent reduces the concentration of such ions in the mixture and inhibits the undesirable reactions. This may be a necessary step to terminate the slow reactions. The type solvent to be added is also important. It should not react with any material and should not lead to particle oxidation. In addition, the viscosity of solvent should be selected properly. Adding very viscous solvents leads to long centrifugation time and loss of the particles which remain in the reaction liquid. Also, with very low-viscosity solvents the particles sit on the tube walls and separating them is not easy. Some solvents can also dissolve and remove unwanted PVP from nanoparticles, which is not desirable.

Figure A.4 depicts the UV-vis responses of silver colloid (silver particle type 1) before and after centrifugation, normalized for easier comparison. There is a shift in peak position toward higher wavelengths (red-shift), indicating that after the centrifugation the ratio of smaller particles to larger ones (with lower and higher resonance wavelengths, respectively) decreases. According to the equation, the precipitation velocity (V_o) is related to the square of the particle diameter (D). So, larger particles precipitate faster than their smaller counterparts.

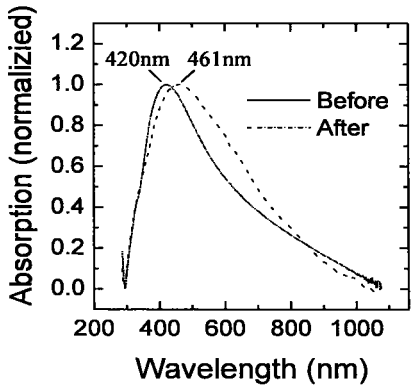

Figure APPX D.2: UV-visible absorption of silver particles in liquid phase before and after centrifugation

After centrifugation, the particles were dispersed in a mixture of MeOH and EG with MeOH:EG=3:1. In the case of Ag particles, the experiments showed that aqueous medium was not adequate for keeping as particles and they precipitated within 2 days. A similar result was observed with a mixture of H_2O and EG with H_2O:EG=3:1 which had almost the same viscosity as MeOH/EG. Thus the solvent substance is more important than its

viscosity. In addition, in aqueous medium the particles got oxidized and the solution turned black, indicating appearance of silver oxide.

The situation was different for Cu nanoparticle colloids. It was observed that the tendency of Cu particles to agglomerate was quite high and many experiments were carried out to find an adequate medium. In contrast to Ag nanoparticles, those of Cu are not very stable. In aqueous solution they tend to follow the reverse reaction and convert to Cu^{2+} (which is accompanied by solution color changing from red to blue). This can be related to the difference between standard reduction potentials of Ag and Cu ($Ag^{+}\rightarrow$ Ag: 0.7996 versus $Cu^{2+}\rightarrow$ Cu: 0.3419) ([216], page 8-23). The trend same was observed for particles dispersed in MeOH or EG but with slower rate. This can be related to presence of water in these alcohols or absorption of humidity from air. The only solvent that can keep copper particles for long time was found to be pure acetone which is not acceptable because of its low viscosity leading to very fast agglomeration. Therefore, the copper nanoparticles obtained were not stored and always applied as a coating material immediately after their preparation.

APPENDIX E

CALCULATION OF ICE REDUCTION FACTOR

$A = \text{ice covered area} \quad (m^2)$

$r = 015m$

$M = (\text{Mass of beam with ice}) \times (\text{Mass of beam without ice}) \quad (kg)$

$$F = M \times r \times \omega^2 = Mr\,(2\pi f)^2 = Mr\left(2\pi \frac{rpm}{60}\right)^2 \quad (N)$$

$$\text{Shear stress} = \tau = \frac{F}{A} \quad (Pa)$$

$$\text{Average shear stress} = \tau_{avg} = \frac{F}{A} \quad (Pa)$$

$$\text{Standard error of } \tau_{avg} = \Delta\tau_{avg} = \frac{1}{3}\sqrt{(\tau_1 - \tau_{avg})^2 + (\tau_2 - \tau_{avg})^2 + (\tau_3 - \tau_{avg})^2} \quad (Pa)$$

$$\text{Ice adhesion Reduction factor} = ARF = \frac{\tau_{avg,non-coated}}{\tau_{avg,coated}}$$

$$\text{Standard error of } ARF = \Delta ARF = ARF \times \left(\frac{\Delta\tau_{avg,non-coated}}{\tau_{avg,non-coated}} + \frac{\Delta\tau_{avg,coated}}{\tau_{avg,coated}}\right)$$